

Scale-adaptivity of the HARMONIE-AROME EDMF-scheme in the shallow cumulus boundary layer

Investigating and reviewing the turbulence partitioning
functions from LES-based coarse-graining

Charlotte Raven

Scale-adaptivity of the HARMONIE-AROME EDMF-scheme in the shallow cumulus boundary layer

Investigating and reviewing the turbulence
partitioning functions from LES-based
coarse-graining

by

Charlotte Raven

to obtain the degree of Master of Environmental Engineering
at the Delft University of Technology,
to be defended publicly on July 3rd 2024 at 10.00 a.m.

Student number:	4605381	
Defense date:	July 3, 2024	
Thesis committee:	Dr. Ir. A.A. Nuijens,	TU Delft, Graduation Chair
	Dr. Ir. W. De Rooij,	KNMI, supervisor
	Dr. Ir. N. Theeuwes,	KNMI, supervisor
	Prof. Dr. Ir. A. P. Siebesma	TU Delft, Secondary supervisor
	Dr. Ir. M.A. Schleiss	TU Delft, Additional assessor

Cover: Shallow cumulus clouds, drawn by D.A. Bouter using
Adobe Photoshop

An electronic version of this thesis is available at <http://repository.tudelft.nl/>.

Preface

A word of thanks

I would like to thank my supervisors Louise, Wim and Natalie for their involved guidance throughout this thesis. It has been quite a turbulent (literally) process, in which you have always given me all the space and support I needed. I have enjoyed working on this topic with all of you, and have been captivated by the science of meteorology and your vast knowledge of it. Thanks a lot!

I also want to thank KNMI for their warm welcome and the opportunity for me to work autonomously on my project, while also getting to know the organization. Furthermore, Pier and Marc, thank you for the additional support and feedback, and for chairing my committee.

Last of all, I want to thank my family and friends for the continuous support and interest throughout this thesis.

*Charlotte Raven
Amsterdam, June 2024*

Abstract

The weather significantly influences daily life, which is predominantly due to short-term weather phenomena occurring in the atmospheric boundary layer (ABL). The HARMONIE-AROME (HARMONIE) model, used by the Royal Netherlands Meteorological Institute (KNMI), simulates the ABL by discretizing the atmosphere into a three-dimensional grid. Processes occurring on scales significantly larger than these grid can be resolved by the model, but processes occurring at scales smaller than the grid (subgrid) are parameterized by theoretical frameworks.

At the current horizontal grid resolution of the HARMONIE model, both shallow convection and smaller-scaled diffuse turbulent transport are parameterized by the Eddy-Diffusivity (ED) and the Mass-Flux (MF) scheme, respectively, coupled in the EDMF-framework. In which the MF is described separately for the dry and the moist (cloudy) updraft. Increasing the model's resolution promises an increase in atmospheric representation, yet introduces challenges in the so-called Grey zone of turbulence, where the scale of the turbulent motions are in the same order of magnitude as grid size, making them neither fully resolved nor fully subgrid.

This study aims to investigate the scale-adaptivity of the HARMONIE EDMF-scheme in the Grey zone of turbulence, for the shallow cumulus boundary layer. To this end, high-resolution Large Eddy Simulation (LES) results of two shallow-cumulus cases are coarse-grained to quantify the partitioning of resolved and unresolved turbulence. It is reviewed how well these partitionings scale against the resolution, normalized with height of the dry (h) and the cloudy boundary layer ($h+h_c$), to investigate the potential of scale-adaptivity of the EDMF-scheme with this height. Additionally, the HARMONIE model is run for one of these cases at three EDMF settings: without scale adaptations, with a scale-adaptive scheme based on both h and h_c , and with an additional vertical velocity threshold.

In the dry boundary layer, the partitionings of turbulences showed to scale well with the height of the dry boundary layer h , but also implied additional large scaled turbulent transport not carried by strong updrafts. The scaling down of the dry MF in the HARMONIE run showed significant reduction, with increased resolved transport. However, the unresolved partitioning to the total flux still was higher than expected by LES results, which may be explained by these large scaled turbulent transport not accounted for with the mass-flux. In the cloud layer, scaling the resolved and unresolved partitioning of the total turbulence with the height of the cloud $h+h_c$ showed not as effective, and indicated that it may not sufficiently represent the strength of convection in the cloud layer. This is supported by the HARMONIE run, that showed too much decrease of the moist updraft. The addition of the vertical velocity threshold showed a too strong decrease of mass-flux, both in the dry and in the mixed layer. An additional figure from LES results suggest that this threshold was set too low and scale-adaptivity of this threshold may be needed.

Contents

Preface	i
Abstract	ii
1 Introduction	1
2 Theory	3
2.1 Atmospheric Boundary layer	3
2.1.1 Convective boundary layer	4
2.2 Numerical Weather Prediction	7
2.2.1 Parameterizations	8
2.3 HARMONIE-AROME	10
2.3.1 Mass-Flux	10
2.3.2 Eddy-Diffusivity	12
2.3.3 Other parameterizations	13
2.4 Large Eddy Simulation	13
3 Problem Definition and Scope	14
3.1 Motivation	14
3.2 Problem	15
3.2.1 The Grey Zone of turbulence	15
3.2.2 Studying the Grey zone	16
3.2.3 Adaptations in the Grey zone	18
3.3 Aim and scope	19
4 Methodology	20
4.1 Benchmark simulations	20
4.1.1 Cabauw case	20
4.1.2 BOMEX	24
4.1.3 Data selection	27
4.2 Resolved and unresolved partitioning to the total turbulence	29
4.2.1 Coarse-graining	29
4.2.2 Total resolved and unresolved	32
4.2.3 Convective resolved and unresolved	34
4.2.4 Similarity parameter	38
4.3 HARMONIE simulations	39
4.3.1 Datapoints	39
4.3.2 Model settings	39
4.3.3 Adaptive convection scheme	40
5 Results and discussion	41
5.1 Partitioning functions from LES	42
5.1.1 Mixed layer	42
5.1.2 Cloud layer	49
5.2 HARMONIE runs	61
6 Conclusion	65
A Coarse-graining	68
B Conditional sampling	71
C Scaling with other heights	76
C.1 Scaling with $h + h_c$ in the mixed layer	76

C.2 Scaling with h_c in the cloud layer	77
D TKE	78

1

Introduction

The weather is one of the most frequently discussed topics in the Netherlands. Which is not surprising, given how significantly the weather impacts our daily lives. Whether it is planning outdoor activities or dealing with transportation disruptions, the weather plays a crucial role in our every day life. Such short-term weather phenomena primarily occur in the atmospheric boundary layer (ABL), the lowest part of the atmosphere where the Earth's surface directly influences atmospheric processes. Accurate prediction and understanding of these weather patterns within the ABL is not only practical, but critical as they affect our economic stability, health, and security. For instance, the ability of crops to be harvested is affected by weather patterns, while the quality of the air affects our health. Furthermore, the occurrence of extreme weather events, such as storms and flooding, represents a potential threat to our safety and well-being.

Consequently, modelling this ABL has become a fundamental instrument in meteorological research. Given the vital importance of accurate weather forecasting, it is evident that continuing development of these models is essential to enhance forecast precision. Likewise, the HARMONIE-AROME, referred to as HARMONIE, the short-term weather model used by the Royal Netherlands Meteorological Institute (KNMI). This is a so-called Numerical Weather Prediction (NWP) model. These models simulate the ABL by discretizing the atmosphere into a grid of finite volumes. Each grid cell represents an average state of the atmosphere within that volume, effectively capturing processes that occur on scales much larger than the size of the grids. However, processes that occur scales smaller than the grid resolution, cannot be directly resolved by the model. Instead, these sub-grid scale processes are parameterized; their effects on the mean state of the grid are approximated, using mathematical formulas based on theoretical physics and empirical data.

Currently, the grids of the HARMONIE model have a horizontal length-scale of 2km, and the dynamic processes that occur at smaller scales than this are parametrized. A critical aspect of these parameterizations is that of the turbulent transport within the ABL. Turbulent transport is significant for the mixing and redistribution of heat, moisture, and momentum in the ABL. Moreover, convective turbulent transport plays a vital role in the ABL by strong vertical transport of air, which can lead to the formation of clouds and storms, making their accurate representation in models crucial. At the current resolution, the HARMONIE model can roughly resolve deep convection, but shallow convection and smaller-scaled turbulence are parametrized with the Eddy-Diffusivity Mass-Flux (EDMF) scheme.

The ability to increase the resolution of the HARMONIE model is becoming more readily available as the power of the computer processing increases. Furthermore, it is of considerable interest as it enables a more detailed representation of atmospheric processes. Higher resolution can capture finer-scale features of turbulence and resolving dynamical processes that cannot be adequately represented by parametrization, which can lead to more accurate and detailed forecasts.

However, with increasing this resolution, one of the challenges in weather modeling is encountered. This is the so-called Grey zone of turbulence. In this zone, the length scales of the turbulent motion are of the same order as the grid spacing, resulting the turbulent processes to not be fully resolved, but neither fully subgrid. From this, the current EDMF-scheme may not be effective at these resolutions, as it is based on grids that are much larger than the turbulent motion.

This Grey zone of turbulence has already been extensively studied. One particularly notable study is that of Honnert et al. (2011). In this study, Large Eddy Simulation (LES), which can sufficiently capture turbulence with high-resolution simulations, are used to study the 'true' turbulence under increasing resolution. This is done by mathematically coarse-grained the simulations, and is used to quantify the resolved and the unresolved partitioning to the total turbulence. The partitionings are presented in relation to the size of the grid, normalized with the height of the boundary layer. This is based on the idea that the of the boundary layer is representative of the vertically dominant length scale of the turbulent motion. In this study, superimposing partitioning functions for several convective cases were found, thereby suggesting a general relationship between the partitioning of resolved and unresolved turbulence to the normalized grid-size. In this context, the suggestion is made to adapt the EDMF-scheme in the Grey zone of turbulence by scaling down the Mass-Flux (MF) component, according to the height of the boundary layer. This approach has already demonstrated some promising outcomes, yet it has also prompted questions regarding its general applicability.

Therefore, this study aims *to investigate the scale-adaptivity of the HARMONIE EDMF-scheme in the Grey zone of turbulence, for the shallow cumulus boundary layer.*

This is done in a two-fold way. Firstly, LES results of two shallow-cumulus cases are mathematically coarse-grained to quantify the resolved and unresolved partitioning to the total turbulence, against the resolution normalized height of the boundary layer, following the method proposed by Honnert et al. (2011). Secondly, the HARMONIE model is run for one of the shallow-cumulus cases in the Grey zone of turbulence at three different settings of the EDMF scheme. The model is run without any scale adaptations, then with a scale-adaptive MF scheme, based on the height of the boundary layer, and finally with an additional vertical velocity threshold. The performance of the three simulations is reviewed and compared with the partitionings found.

In the following chapter, a comprehensive theoretical framework is provided on the key terms (2). Subsequently, Chapter 3 presents a detailed explanation of the problem and the specific subquestions of this research. Chapter 4 describes the methodologies employed to address these questions. The findings from these methods are presented and analyzed in Chapter 5. Lastly, Chapter 6 offers the conclusion on the scale-adaptivity of the HARMONIE EDMF-scheme and provides a future perspective.

2

Theory

This chapter outlines the theory required for this research. First, the lower layer of the Earth's atmosphere, the Atmospheric Boundary Layer (ABL), is discussed in chapter 2.1. Specifically, the Convective Boundary Layer (CBL) and its turbulence processes are covered. Secondly, the main concept and framework of numerical weather prediction (NWP), a typical method of modelling this ABL, is explained in chapter 2.2. Then, the NWP model used by KNMI to study and forecast the ABL of the Netherlands, the HARMONIE-AROME model, and its specifications are discussed in chapter 2.3. Finally, the high-resolution LES model is treated in chapter 2.4.

2.1. Atmospheric Boundary layer

The atmospheric boundary layer (ABL) represents the lowest part of the Earth's atmosphere, which is most strongly influenced by the interaction with the Earth's surface. From the effects of solar radiation together with surface conditions, the ABL is characterized by dynamic exchanges of atmospheric variables between the surface and the atmosphere above, on short temporal scales up to one hour (Stull, 2012). This exchange of momentum, heat, moisture, and pollutants is done by turbulent eddies. These occur on a variety of scales, ranging from a few millimeters to kilometers, and are both mechanically and thermally driven. Throughout the diurnal cycle, the ABL changes continuously and is strongly influenced by orography, surface conditions, and the macroscale dynamics of the atmosphere. However, an idealized diurnal cycle of the ABL can be described for fair weather conditions over flat land.

At the end of the night, as the Earth's surface has received no radiance for a long time, and it cools down, the air above the surface becomes stably stratified. This prevents air at the surface from rising, suppressing turbulence and mixing. During this stable boundary layer (SBL), moderate mixing is caused only by wind; the wind flowing over the surface is slowed down by friction, creating a gradient in wind speed known as wind shear. This shear generates mechanical turbulence, which is usually not very strong. The height of the Nocturnal Boundary Layer (NBL) is dependent on the wind velocity and the surface's roughness, but rarely exceeds 300 meter (Cushman-Roisin, 2022).

After sunrise, the Earth's surface warms up, heating the nearby air through sensible heat, making it warmer than the air above. This warmer air naturally rises, forming upward-moving thermals that mix atmospheric variables within the boundary layer. This process, known as convective turbulent transport, is driven by temperature gradients and includes large updraft that can reach from the ground to the top of the CBL (Honnert et al., 2020). Convection is usually the main mechanism of turbulence production in the ABL, whereas wind shear contributes less significantly. Nonetheless, wind shear can influence these updrafts. Strong wind shear can elongate and tilt them, creating more complex turbulent structures. Such interactions can either enhance or diminish the effectiveness of vertical transport when compared to weaker shear conditions. If the wind shear is significantly strong, it can stabilize the atmosphere by spreading the rising air horizontally before it can rise. This can suppress the development of deep convection, leading to a less unstable, or neutral boundary layer despite the presence of surface heating. When the wind shear production is negligible compared to the convective turbulence production, we speak of a convective boundary layer (CBL).

As the sun sets again, the surface's solar heating diminishes and the convective mixing quickly

decreases. The CBL gradually dissipates, leaving a residual layer with mixed properties above the NBL. The dynamics of the ABL and its diurnal cycle are essential for local weather patterns, but also for larger climatic patterns (Cushman-Roisin et al., 2008).

2.1.1. Convective boundary layer

The CBL can be vertically subdivided into three regions. The surface layer, which in the case of a CBL, is usually the lower 10% of the layer (Schmidt and Schumann, 1989). It is characterized by strong gradients in atmospheric properties. Within this layer, essential physical processes of the CBL take place. As discussed, the sensible heat flux from the surface, and the production of wind shear take place in this lower layer, and are both essential for production of turbulence. Additionally, the solar heating causes moisture from the surface to heat and evaporate, transferring moisture into the CBL, essential for cloud formation. Above the surface layer, atmospheric properties are relatively uniform with height, due to strong turbulent mixing. This is referred to as the mixing layer. At the top of the CBL, a temperature inversion layer separates the mixing layer from the more stable free atmosphere above. This inversion layer acts as a cap, inhibiting further upward movement of thermals and thus the vertical extent of the CBL. Strongly buoyant thermals may overshoot this inversion layer due to their momentum, and penetrate into the stably stratified free atmosphere. While losing their buoyancy and eventually sinking back into the CBL, warm and dry air is entrained into the CBL. This entrainment can enhance the vertical growth of the CBL and influences the distribution of heat, moisture, and momentum within this layer (Fedorovich et al., 2004). The height of the CBL is dependent on multiple atmospheric conditions, such as the incoming solar radiation and the surface characteristics, but can reach peak altitudes of 1-3 km over continental surfaces (X. Wang and Wang, 2016).

Thus, the development of the CBL is driven by turbulent transport, and this turbulence can be subdivided into two regimes: large-scaled, organized, non-local turbulence, from now on referred to as convective turbulence and small-scaled, random, local, referred to as diffuse turbulence. Although in nature these two are far from unrelated and no clear division really exists, it is of interest to separately describe them for better understanding.

Convective transport

Convective transport is driven by instability of the boundary layer, as a function of vertical difference in temperature. Convective eddies have larger length and time scales than those of diffusive transport and are organized into larger structures.

As discussed, during the day, the surface warms as the incoming solar radiation is absorbed, the air above heated directly from the surface, by sensible heating. As the air above the surface warms up, it expands and becomes less dense. The less dense, lighter air is positively buoyant and begins to rise. As buoyant air rises, it moves into regions of lower atmospheric pressure. The decrease in pressure causes the air parcel to expand adiabatically. During adiabatic expansion, the air parcel does work on the surrounding air, leading to a decrease in its temperature. The rate at which the temperature of a rising air-parcel changes due to this adiabatic processes is known as the adiabatic lapse rate.

How far the air-parcel can reach, depends on the conditions of the ABL. It will continue to rise until all of its kinetic energy is lost. The main contributor to this kinetic energy is the buoyancy. A parcel remains positively buoyant, as long as its potential temperature is higher than it surrounding.

When the ABL is stable, the lapse rate of the environmental temperature is less than the adiabatic lapse rate, meaning that the parcel cools faster than it surrounding air. This leads to negative buoyancy, and the parcel tends to sink back to its original position. When the ABL is unstable, the lapse rate of the environmental temperature is greater than the adiabatic lapse rate. The parcel remains positively buoyant and continues to rise until it hits the thermal inversion of the environment. By definition, the CBL is unstable, allowing parcels to remain positively buoyant till a layer of inversion.

The rising air creates an area of lower pressure at the bottom, allowing cooler and denser air to move into this area. As this air is heated again, organized convective circulations develop with buoyant updrafts and surrounding downdrafts.

From this convective transport, cumulus clouds may form. If the air can rise sufficiently, it can reach its lifting condensation level (LCL). This is the level where the temperature of the parcel is equal to its dew point temperature. At this temperature, the air is fully saturated and can no longer hold all of its humidity as water vapor. The excess water vapor condenses into liquid water, and clouds start to form.

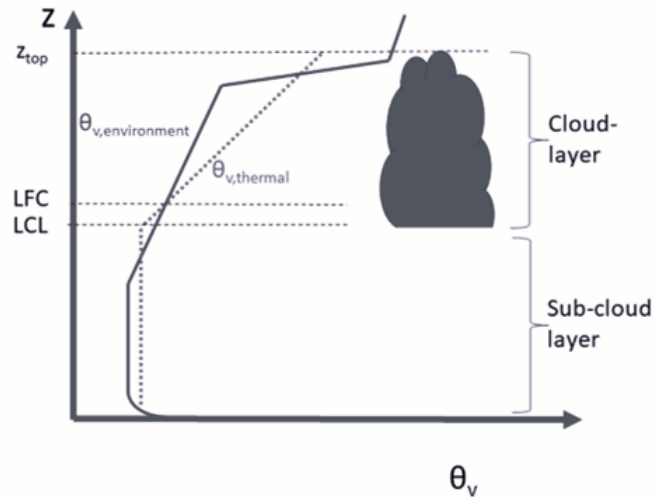


Figure 2.1: Idealized vertical profile of the virtual potential temperature for cumulus convection (De Rooy and Siebesma, 2008)

This process of condensation releases heat onto the parcels of air, causing the lapse rate to decrease, known as the moist adiabatic lapse rate.

When the CBL is very unstable and parcels are buoyant when reaching the LCL, the air can continue to rise and condensate, creating deep convective clouds till strong inversion occurs.

When the CBL is less unstable, the rising air may become less buoyant than its surrounding before reaching the LCL. However, due to the remaining kinetic energy, it can overshoot the inversion and still reach the LCL. Very shallow cumulus clouds start to form from the oversaturated parcels. The remaining energy cause the parcels to rise while cooling at the moist adiabatic lapse rate. If this energy is strong enough, the non-buoyant air parcel may become more buoyant than its environment again. This is referred to as the Level of Free Convection (LFC), the parcel will continue to rise freely without any external lifting force, deepening the shallow cumulus clouds till strong inversion occurs.

In figure 2.1, an idealized vertical profile of potential temperature is shown for a cumulus case. It shows the thermal rising and overshooting the environmental inversion, reaching the LCL and from there on rising with a decreased lapse rate. It reaches the LFC, and becomes positively buoyant again, and remains to rise and form clouds, till strong inversion occurs.

The amount of energy that must be overcome by an air-parcel to rise from the LCL to the LFC is expressed with the Convective Inhibition (CIN). It is calculated by integrating the negative buoyant energy over the depth of the layer, where the parcel is less buoyant than the environment. A high value of this parameter indicates a strong barrier to convection, which impedes or prevents the formation of clouds. Conversely, a low or zero value indicates the potential for deep convective clouds and thunderstorms to develop.

The total energy available for parcels to rise after the CIN is overcome, thus from the LFC to the strong inversion, is represented by the Convective Available Potential Energy (CAPE). It is calculated by integrating the positive buoyant energy over the depth of the layer, where the parcel is more buoyant than the environment. A High CAPE value indicates a high potential for deep convection and thunderstorms, while a low CAPE value suggests limited convection (Cushman-Roisin et al., 2008).

Diffusive transport

As discussed, turbulent transport of atmospheric properties within the CBL is not only performed by convective, organized motions. It also involves diffuse turbulent transport, which is driven by small-scaled, less-organized eddies. These arise mechanically from the presence of wind shear in the ABL. Additionally, in the CBL, energy from larger, organized convective thermals breaks down into smaller eddies. This cascading effect leads to the creation of a spectrum of turbulent eddies of various sizes, contributing to this diffuse turbulence. The diffuse turbulent transport plays a crucial role in the mixing

processes within the CBL, especially because it mixes properties over smaller temporal and spatial scales. By distributing heat, moisture and momentum, it affects their profiles and the stability of the boundary layer. In case of a neutral surface layer, this type of turbulent transport is dominant, as no convection occur. However, in the CBL, convection is the dominant type of turbulent transport (Stull, 2012).

2.2. Numerical Weather Prediction

Using computer simulation, it is possible to model the processes and dynamics discussed above, and thus to generate short-term weather forecasts. A frequently applied approach for this is the use of Numerical Weather Prediction (NWP) models. In this approach, the ABL is simulated by dividing the atmosphere above the area of interest into a three-dimensional grid. At each point on this grid, the model calculates atmospheric variables through a series of partial differential equations based on the equations of fluid motion (Pu and Kalnay, 2019). These are known as the primitive equations and include the Momentum Equation (2.1), Continuity Equation (2.2), Thermodynamic Energy Equation (2.3), Moisture Continuity Equation (2.4) and the Equation of State (2.5).

$$\frac{D\mathbf{v}}{Dt} = -\frac{1}{\rho}\nabla p + f\mathbf{v} + \text{Friction terms} \quad (2.1)$$

$$\frac{\partial\rho}{\partial t} + \nabla \cdot (\rho\mathbf{v}) = 0. \quad (2.2)$$

$$\frac{DT}{Dt} = \frac{1}{\rho c_p} \left(Q - \frac{Dp}{Dt} \right). \quad (2.3)$$

$$\frac{Dq}{Dt} = S - C. \quad (2.4)$$

$$p = \rho RT. \quad (2.5)$$

Where $\mathbf{v} = (u, v, w)$ represents the velocity, ρ is the density of air, p is the atmospheric pressure, f represents the Coriolis parameter, T is the temperature, c_p the specific heat at constant pressure, Q is the diabatic heating rate per unit mass, q is the specific humidity or mixing ratios, S and C are the source and sink terms for moisture, representing the rates of evaporation and condensation / precipitation, respectively. ∇ represents the gradient in equation 2.1, and with $\nabla \cdot$ in equation 2.2 it represents the divergence. $\frac{D}{Dt}$ is the total derivative, representing the rate of change of the fluid:

$$\frac{Du}{Dt} \equiv \frac{\partial u}{\partial t} + u \frac{\partial u}{\partial x} + v \frac{\partial u}{\partial y} + w \frac{\partial u}{\partial z}$$

As it is not possible to solve these equations analytically, NWP numerically approximates the solution by using finite-difference equations (FDEs). Here, a first order discretization is given as an example. Taking the continuity equation, only the eastward direction gives:

$$\frac{\partial\rho}{\partial t} + \frac{\partial(\rho u)}{\partial x} = 0$$

Discretizing the spatial domain, x_i represents the spatial coordinate at the i -th grid point and Δx as the grid-spacing. The spatial derivative can be rewritten as

$$\frac{\partial\rho}{\partial x} \approx \frac{\rho_i - \rho_{i-1}}{\Delta x}$$

Doing the same for time, using discrete steps with t_n representing the time in the n -th time step, and Δt as the size of the time step. The temporal derivative can be rewritten as:

$$\frac{\partial\rho}{\partial t} \approx \frac{\rho_i^{n+1} - \rho_i^n}{\Delta t}$$

Substituting these finite-difference approximations into the continuity equation gives:

$$\frac{\rho_i^{n+1} - \rho_i^n}{\Delta t} + \frac{\rho_i^n u_i^n - \rho_{i-1}^n u_{i-1}^n}{\Delta x} = 0$$

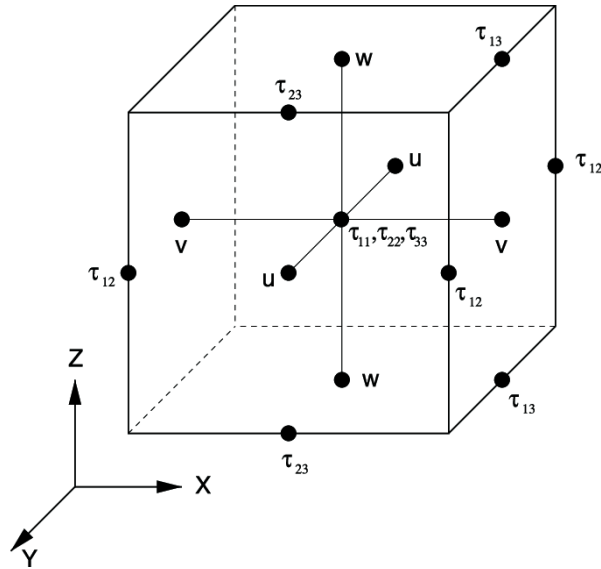


Figure 2.2: Staggered grid (Lundquist et al., 2010)

This method is applied to all primitive equations.

To numerically solve these equations, the conditions of the initial state of the atmosphere are essential. They are usually obtained from a combination of observational data and short-range weather forecasts (Pu and Kalnay, 2019).

By integrating the set of equations forward, the future atmospheric state can be approximated, represented in equation 2.6 (Richardson, 1922).

$$\begin{aligned} \frac{\partial \varphi}{\partial t} &= F(\varphi, t) \\ \varphi|_{t+\Delta t} &= \varphi|_t + F(\varphi|_t, t) \Delta t \end{aligned} \quad (2.6)$$

Note that this is a first order forward difference, while NWP models typically use various higher orders of finite difference schemes, to ensure computational stability (Pu and Kalnay, 2019).

As most NWP models are a subset of a larger system, boundary conditions are vital components of these models. For example, global atmospheric models need both top and bottom boundary conditions, and regional models also require additional lateral boundary conditions. With the initial conditions, forward integration of the FDEs, and boundary conditions, the NWP model can now resolve atmospheric variables at each grid point.

Rather than positioning all variables at the same grid points, numerous numerical models apply a staggered grid method, shown in figure 2.2. Here, the atmospheric prognostic variables such as temperature, pressure, and humidity (T , p , and q), are defined in the center, representing the average over the grid box. The horizontal wind velocities (u , v and w) are located on the grid edges, representing the average of the wind velocity between the centers of the adjacent boxes. This approach aligns more closely with physical principles and allows for a more accurate formulation of several primitive equations (Pu and Kalnay, 2019).

2.2.1. Parameterizations

The use of numerical discretization to solve PDEs implies that the resolution of the NWP model is always limited, leaving some processes in the atmosphere unresolved. The primitive equations illustrate how the model's dynamics are influenced by various physical processes. For example, the impact of heating sources such as radiation, sensible heat transfer, and latent heat release are evident in the thermodynamic equation (2.3) with the diabatic heating rate Q , while the influences of condensation and evaporation are apparent in the moisture continuity equation (2.4) with the source and sink terms, S and C . Therefore, it is essential to incorporate these physical processes, including radiative transfer,

cloud microphysics, and surface conditions, into the model. In addition, atmospheric motion includes a wide range of temporal and spatial scales. With the current effective resolutions of NWP models, it is inevitable that certain dynamics smaller than the grid-spacing will remain unresolved. Once again, these processes can have a substantial impact on the atmospheric conditions, so their effect must be taken into account (Pu and Kalnay, 2019).

This is evidently shown when the primitive equations are rewritten by separating mean and fluctuating components of their prognostic variables, using the Reynolds decomposition (2.7) (Pielke, 2013).

$$\varphi = \bar{\varphi} + \varphi' \quad (2.7)$$

Where, the mean $\bar{\varphi}$ is defined as an average over a grid cell and φ' represents the deviations from this mean.

Applying the Reynolds Decomposition to the moisture continuity equation:

$$\frac{D(\bar{q} + q')}{Dt} = S - C$$

Expanding the derivative using the linearity of derivatives:

$$\frac{D\bar{q}}{Dt} + \frac{Dq'}{Dt} = S - C$$

Using the definition of the total derivative:

$$\left(\frac{\partial \bar{q}}{\partial t} + u \frac{\partial \bar{q}}{\partial x} + v \frac{\partial \bar{q}}{\partial y} + w \frac{\partial \bar{q}}{\partial z} \right) + \left(\frac{\partial q'}{\partial t} + u' \frac{\partial q'}{\partial x} + v' \frac{\partial q'}{\partial y} + w' \frac{\partial q'}{\partial z} \right) = S - C$$

Averaging the entire equation:

$$\overline{\left(\frac{\partial \bar{q}}{\partial t} + u \frac{\partial \bar{q}}{\partial x} + v \frac{\partial \bar{q}}{\partial y} + w \frac{\partial \bar{q}}{\partial z} \right) + \left(\frac{\partial q'}{\partial t} + u' \frac{\partial q'}{\partial x} + v' \frac{\partial q'}{\partial y} + w' \frac{\partial q'}{\partial z} \right)} = \overline{S - C}$$

With the averaging rules ($\overline{A + B} = \overline{A} + \overline{B}$) and properties of fluctuations ($\overline{q'} = 0$), this becomes:

$$\frac{D\bar{q}}{Dt} + \overline{u' \frac{\partial q'}{\partial x}} + \overline{v' \frac{\partial q'}{\partial y}} + \overline{w' \frac{\partial q'}{\partial z}} = \overline{S} - \overline{C}$$

Assuming incompressible flow, this can be rewritten as:

$$\frac{D\bar{q}}{Dt} = -\frac{1}{\rho} \frac{\partial \rho}{\partial z} \left(\overline{\frac{\partial q' u'}{\partial x}} + \overline{\frac{\partial q' v'}{\partial y}} + \overline{\frac{\partial q' w'}{\partial z}} \right) + (\overline{S} - \overline{C}) \quad (2.8)$$

The correlations of fluctuating properties with fluctuations of velocity in the atmosphere can be associated with turbulent transport of these properties (Reynolds, 1987). Thus, the second, third, and fourth component of the right-hand side of the equation represent the subgrid turbulent transport in the eastward, northward and vertical direction, respectively. This can be applied to all primitive equations, giving a general form of equation that states that the change of the mean variable in the grid is dependent on the changes in turbulent fluxes within the grid, and additional effective physical processes.

$$\frac{D\bar{\varphi}}{Dt} = -\frac{1}{\rho} \frac{\partial \rho}{\partial z} \left(\overline{\frac{\partial \varphi' u'}{\partial x}} + \overline{\frac{\partial \varphi' v'}{\partial y}} + \overline{\frac{\partial \varphi' w'}{\partial z}} \right) + F_{\varphi} \quad (2.9)$$

These subgrid processes affect the large-scale grid-box averages and vice versa are affected by them. To describe this impact both ways, parametrization of subgrid-scale processes, in terms of the resolved grid averages, are necessary (Pu and Kalnay, 2019). Most NWP models, assume that this subgrid turbulent transport is dominated by the vertical component and are therefore one-dimensional (Honnert et al., 2020).

$$\frac{D\bar{\varphi}}{Dt} = -\frac{1}{\rho} \frac{\partial \rho}{\partial z} \frac{\partial \overline{\varphi' w'}}{\partial z} + F_{\varphi} \quad (2.10)$$

The parameterization schemes of both turbulence and other physical processes are usually developed from fundamental physical principles, together with empirical relations from observational data and high-resolution simulations (Nychka, 2000).

2.3. HARMONIE-AROME

The HARMONIE-AROME (HIRLAM–ALADIN Research on Mesoscale Operational NWP in Euromed), from now on referred to as HARMONIE, is such an NWP model, operated by the Royal Dutch Meteorology institute (KNMI). Its origin lays in the cooperation of the Northern Europe research program High Resolution Limited Area Model (HIRLAM) and the central European collaboration Aire Limitée Adaptation Dynamique Développement International (ALADIN), to develop a high-end numerical weather prediction (NWP) model, applicable in all its regions. To this end, the readily existing Applications of Research to Operations at Mesoscale (AROME) model is extended for use across all ALADIN-HIRLAM countries. The model is designed for short and very short range forecasting, including now-casting, to support both research and operational activities. It operates with the same non-hydrostatic dynamical core as AROME-France, with modifications to suit Nordic weather conditions. It generally runs at a horizontal resolution with 2.5km grid-spacing and contains 65 vertical layers. At the lateral boundaries, it is forced by the global ECMWF-IFS model (Bengtsson et al., 2017). As discussed, the effects of processes that cannot be resolved by the NWP model, are accounted for with parameterization schemes. Likewise, HARMONIE uses a set of schemes to represent the subgrid processes. In this section, the specifications of the parametrization schemes used in HARMONIE model, CY46h1, are outlined.

At the current resolution, deep convection can be fully resolved by the model (Bengtsson et al., 2017). This leaves the remaining shallow convection and diffuse turbulence to be parametrized. As most NWP models, the HARMONIE model assumes the subgrid turbulent transport to be dominated by the vertical component, expressed in equation 2.10. To parameterize the total subgrid turbulent transport, the HARMONIE model utilizes an Eddy-Diffusivity Mass-Flux (EDMF) framework. In this framework, the total turbulent transport in the CBL is decomposed into a convective and a diffuse term, found on the idea that convective cloud are rooted in dry convective thermals in the subcloud layer (Siebesma et al., 2007). This is done by defining a decomposition between the strong cumulus updrafts and the remaining environmental diffuse turbulent transport. The convective updrafts are described with a Mass-Flux approach, separately from the remaining diffuse turbulence, which is represented with an Eddy-Diffusivity approach (Siebesma and Teixeira, 2000). This framework facilitates a unified description of the turbulent transport in the CBL, proven to effective for both dry cases (Siebesma et al., 2007) and cloud-topped cases (Soares et al., 2004).

$$\overline{w'\varphi'} = \overline{w'\varphi'}^{\text{turb}} + \overline{w'\varphi'}^{\text{conv}} \quad (2.11)$$

2.3.1. Mass-Flux

The Mass-Flux scheme, used in the HARMONIE model, is based on the one developed by Neggers et al. (2009). And its derivation is described here.

As discussed, the decomposition between the convective and diffuse turbulent transport is based on distinguishing strong updrafts from environmental turbulent motion. For any atmospheric variable, a mean value for both areas can be defined with equation 2.12.

$$\begin{aligned} \varphi_u \equiv \varphi_c &\equiv \frac{1}{A_u} \iint_{\text{updraft area}} \varphi dx dy \\ \varphi_e \equiv \varphi_e &\equiv \frac{1}{A_e} \iint_{\text{environment part}} \varphi dx dy \end{aligned} \quad (2.12)$$

By defining the updraft fraction is defined with $a_u = \frac{A_u}{A}$, the total mean of the variable can be written as:

$$\bar{\varphi} = a_u \varphi_u + (1 - a_u) \varphi_e \quad (2.13)$$

Then, substituting this into the total mean flux, it can be written in a decomposed form. This is done in equation (2.14), with the first term representing the diffusive turbulence in the environment, the second term representing the diffusive turbulence in the updraft, and the third term representing the organized convective term.

$$\overline{w'\phi'} = (1 - a)\overline{w'\phi'}^e + a\overline{w'\phi'}^u + a(1 - a)(w_u - w_e)(\phi_u - \phi_e) \quad (2.14)$$

Thus, the convective flux can be described with:

$$\overline{w'\phi'}^{\text{conv}} = a(1 - a)(w_u - w_e)(\phi_u - \phi_e) \quad (2.15)$$

By assuming that the updraft fraction is significantly smaller than unity ($a_u \ll 1$), the environmental mean is equal to the total mean ($\phi_e \simeq \bar{\phi}$) and the vertical speed of the updraft is much greater than that of its surroundings ($w_u \gg w_e$), the subgrid convective turbulence can be written with the Mass-Flux approximation (Gu et al., 2020):

$$\overline{w'\phi'}^{\text{conv}} = a_u w_u (\phi_u - \bar{\phi}) \equiv \frac{M}{\rho} (\phi_u - \bar{\phi}) \quad (2.16)$$

Here, $M = \rho a_u w_u$ represents the mass-flux of the strong updraft. Therefore, rather than directly simulating separate updrafts, the vertical convective transport is modeled as a single, steady-state updraft (Pergaud et al., 2009).

Dual Mass-Flux

Additionally, a distinction is made between the dry and moist convective updraft in HARMONIE. This is done using a Dual Mass-Flux approach (Neggers et al., 2009). Here, the dry updraft describes the thermals that do not saturate and the moist updraft describes the thermals that reach their LCL and continue to rise in the cloud layer (de Rooy et al., 2022).

$$\overline{w'\phi'}^{\text{conv}} \approx \frac{M_{\text{dry}}}{\rho} (\phi_{\text{u, dry}} - \bar{\phi}) + \frac{M_{\text{moist}}}{\rho} (\phi_{\text{u, moist}} - \bar{\phi}) \quad (2.17)$$

This framework allows for a smooth transition between the mixed layer and the cloud layer above, as both dry and moist convection can coexist simultaneously (Neggers et al., 2009). Additionally, the dry convective term guarantees a zone of counter-gradient fluxes at the top of the dry CBL, which is known to be ill-represented by an eddy-diffusivity (Honnert et al., 2020).

Updraft profile

The mass-flux is initialized at the surface using excess values for temperature and humidity, and at cloud base with a closure scheme proposed by Grant, 2001, using convective velocity scaling derived from the surface buoyancy flux. Then, an updraft equation is used for the vertical velocity of the updraft, which is used to estimate the penetration height of the updraft. This equation can be used for both the dry and the moist updraft, giving the height of the inversion of the dry boundary layer, the height of the cloud base and the cloud top.

How the updraft changes with height, is determined by the horizontal entrainment and detrainment. The entrainment is the mass-flux divergence, from the environment inwards to the updraft, and the detrainment D is the outward mass-flux divergence.

$$\frac{\partial M_u}{\partial z} = (E - D) \quad (2.18)$$

With $E = \varepsilon M$ and $D = \delta M$, where ε and δ are the fractional entrainment rate and detrainment rate.

The profiles of the entrainment rate can be found using the heights from the updraft equation. A different entrainment rate profile is found for the different updraft types. For the dry convection, the

entrainment is a function of the inversion of the dry updraft, formulated by Siebesma et al., 2007, based on LES results for the dry convective boundary layer. In the moist subcloud layer, the updrafts must represent stronger thermals than in the dry CBL. From this, the entrainment profile is extended into the moist subcloud layer, with adjustments considering that the updraft does not stop at the inversion height and that these stronger updrafts are associated with smaller entrainment rates. The profile of the entrainment rate in the cloud layer is linked to the value of ε at the top of the subcloud layer. From there, it decreases proportionally with height (de Rooy et al., 2022). However, the detrainment shows to be much more dominant in the formulation of the cloudy updraft profile than entrainment and to have a much larger variation (De Rooy and Pier Siebesma, 2010). Resulting, variations in the Mass-Flux profile from case to case and hour to hour can be almost exclusively related to the detrainment rate δ (De Rooy and Siebesma, 2008). The variation of magnitude in δ can be assigned to the depth of the cloud layer, the humidity of the environment and the buoyancy of the updraft.

The transition between the dry and moist updraft is ensured with the mass flux closure at cloud base, defined as:

$$M_{z_{cl}} = c_b w_* \quad (2.19)$$

Where $M_{z_{cl}}$ is the mass flux at the level of condensation, w_* is the convective velocity scaling, and c_b is a constant, set to 0.035. In the subcloud layer, the moist updraft mass flux is prescribed to increase linearly to the value at cloud base (de Rooy et al., 2022).

Note that downdrafts are disregarded in this parameterization, as it is applied solely to shallow convection (Pergaud et al., 2009). Studies within the CBL show that the mass-flux scheme is typically dominant in turbulence parametrization, accounting for 80–90% of the overall moist and temperature flux (Siebesma and Cuijpers, 1995).

2.3.2. Eddy-Diffusivity

The diffusive transport is approximated with vertical diffusion using the eddy-diffusivity (ED) approach. It assumes that the diffuse transport of a variable is proportional to its vertical gradient and an eddy-diffusivity coefficient. This can be described with:

$$\overline{w'\phi'}^{\text{diff}} = -K \frac{\partial \overline{\phi}}{\partial z} \quad (2.20)$$

This eddy-diffusivity coefficient K thus describes the rate at which the atmospheric properties are being transported by turbulent eddies (Siebesma and Teixeira, 2000). In the HARMONIE model, the TKE-based HARATU (Harmonie with Racmo Turbulence) scheme is implemented Bengtsson et al., 2017. Here, the eddy-diffusivity coefficient is based on the prognostic TKE and the formulation of the mixing length:

$$K = l\sqrt{TKE} \quad (2.21)$$

where the Turbulent Kinetic Energy (TKE) represents the energy from turbulent motion with the variance in velocities:

$$TKE = \frac{1}{2}(\overline{(u')^2} + \overline{(v')^2} + \overline{(w')^2}) \quad (2.22)$$

The mixing length-scale l is derived using two distinct length-scales: a stable ABL length-scale l_s , and a length-scale l_{int} for unstable or weakly stable conditions.

The formulation of the stable length-scale scale is given by the square root of the TKE, divided by the Brunt–Vaisala frequency N , which is an indicator of the environmental stability. It is multiplied with a stability correction for momentum or heat separately ($c_{m,h}$):

$$I_s = c_{m,h} \frac{\sqrt{TKE}}{N}, \quad (2.23)$$

The formulation of the unstable and weakly-stable length-scale scale is given by :

$$l_{int} = \kappa z \left(1 - \frac{z}{h}\right)^2 \quad (2.24)$$

Where κ is the von Kármán constant, typically $\kappa \approx 0.4$, z is the height and h is the boundary layer height. For convective conditions, the integral length scale follows a quadratic profile (Lenderink and Holtslag, 2004). The effective length-scale for momentum and humidity $l_{m,h}$ that can be generally applied, is found by interpolating these length-scales (Lenderink and Holtslag, 2004). The Mass-Flux and Eddy-diffusivity scheme are directly coupled by the TKE budget equation. In this budget equation, the mass-flux is used as a source term, mimicking the energy cascade in which turbulent kinetic energy cascades from the larger eddies down to the smaller eddies (de Rooy et al., 2022).

2.3.3. Other parameterizations

As discussed, not only turbulent motion occurring on subgrid scales requires parameterization; other physical processes that cannot be resolved must be accounted as well. Therefore, the HARMONIE model uses parameterization schemes for radiation, clouds and microphysics and surface physics (Bengtsson et al., 2017). The radiation scheme consists of a longwave and shortwave radiation scheme. Both define whether the sky is cloudy or clear and with input of properties such as aerosols, atmospheric gases and cloud properties, and calculate the radiation properties such as the irradiances at the surface and the short- and longwave radiative fluxes on each model level (Bengtsson et al., 2017). The cloud scheme is a statistical scheme, and is tightly coupled with the EDMF-scheme. It determines the cloud cover by determining the variance in saturation, using the subgrid variability of the specific humidity q_t and liquid water potential temperature Θ_l , compared to the saturation specific humidity. Both their variances are contributed positively by turbulence and convection, which is directly linked within their mathematical expression (de Rooy et al., 2022). For the surface parameterization, the SURFEX scheme is included to define the type of surface (sea, ocean, lake, urban area, soil, or vegetation). It then uses different physical models to simulate atmospheric processes that occur at the surface, such as the exchange of energy and moisture between the surface and the atmosphere above. Additionally, it reflects surface properties, such as surface roughness, topography, and albedo. From these, it can be used to obtain surface and near-surface atmospheric variables (Bengtsson et al., 2017). These schemes are not independent, as mentioned, the cloud scheme is directly coupled with the EDMF-scheme, but also schemes are indirectly coupled. For instance, the fluxes at the surface influence the effective parameterized turbulence, the surface fluxes are affected by the incoming radiation, which in turn is affected by the cloud cover. These are just some of many implications of atmospheric modeling, making it a challenging field of research.

2.4. Large Eddy Simulation

Large Eddy Simulation (LES) models are somewhat similar to NWP models, as the area of interest is divided into a three-dimensional grid to numerically solve its governing equations. However, these models are designed to run at much higher resolutions, with grid sizes on the order of 10 meters (Honnert et al., 2011). At these resolutions, most turbulence is resolved, leaving only small scales to be parameterized (Wyngaard, 2004). These types of simulations are computationally too demanding to use for operational weather forecasts (Kealy, 2019), but can be well-used to simulate and study structures of turbulence in the ABL over smaller domains (Huang et al., 2009). In this study, the Dutch Atmospheric Large-Eddy Simulation (DALES) model is used. This model is designed to study processes in the boundary layer, cloud formation, and other processes on small spatial and temporal scales. It simulates atmospheric processes, using three-dimensional numerical modeling of the incompressible Navier-Stokes equations for fluid flow and the equations for thermodynamics. With these, prognostic variables such as the wind velocity components, the liquid water potential temperature and the specific humidity are computed (Heus et al., 2010). The discussed remaining subgrid part of the turbulence is parametrized, and is assumed to be isotropic and homogeneous. For this three-dimensional turbulence parametrization, the concept of eddy-diffusivity is used. The eddy diffusivity coefficients are modeled as a function of the turbulent kinetic energy (TKE) (Deardorff, 1980) or of the rate of strain by using the Smagorinsky approach (Smagorinsky, 1963). A more detailed description can be found at Heus et al. (2010).

3

Problem Definition and Scope

This chapter provides a detailed description of the nature of the problem and the approach to studying it. It outlines the motivation for running the HARMONIE model at higher resolutions than those currently used (3.1). Then, it discusses the problems that arise from this higher resolution modeling, namely the Grey Zone of turbulence (3.2). Finally, it outlines the aim and scope of the research, to study the problems that have been identified (3.3).

3.1. Motivation

The KNMI employs the HARMONIE model to forecast the weather over 48 hours for the Netherlands and neighboring regions (KNMI, 2023). As discussed in the previous chapter, the dynamics within the atmospheric boundary layer (ABL) are crucial for these short-term weather patterns. Furthermore, accurate simulation of CBL processes, such as boundary layer mixing and cumulus convection, has proven to be crucial for large-scale atmospheric modeling (Siebesma and Cuijpers, 1995, Siebesma et al., 2003, Pergaud et al., 2009, Giani and Crippa, 2024).

At the resolution with a horizontal grid spacing of 2km, the model can roughly resolve deep convection. However, turbulent motion of the CBL that occurs at smaller temporal and spatial scales, remains to be unresolved, sub-grid, at this resolution. These motions include shallow convection and diffuse turbulence, and are treated in the model with parameterization schemes.

With the current increase in computer power, it is possible to run these models with a smaller grid spacing, resulting in a higher resolution. The general expectation from an increase in resolution is a corresponding increase in accuracy (Mass et al., 2002). And indeed, a higher resolution can be of great use in short-term weather modeling.

Firstly, it can give more spatial details. With a smaller grid spacing, maxima in, for example, rainfall are less averaged, resulting in more accurate predictions of heavy rainfall.

Secondly, regions with complex terrain can be modelled in more detail at higher resolution (Valkonen et al., 2020). Surface features such as water and vegetation can significantly affect atmospheric variables as temperature and humidity, especially in urban areas (Lean et al., 2019). In addition, Boutle et al. (2016) showed that the modeling of wind flows over orographic regions is improved with a higher resolution.

Lastly, and perhaps most importantly, at a higher resolution, smaller scaled processes such as shallow cumulus convection can be explicitly resolved. Convection parameterization schemes have been shown to poorly represent organized convection and the effects of convective self-aggregation, associated with heavy rain and thunderstorms (Pendergrass, 2020). This inaccuracy of the convection parameterization schemes in representing cloud-related processes is found to contribute significantly to the inherent uncertainty of climate models (Judt and Rios-Berrios, 2021, Bretherton, 2015, Hohenegger et al., 2008). Previously conducted high-resolution studies have shown that by resolving convective processes, significant improvements can be found. These include more realistic precipitation patterns and variability (Judt and Rios-Berrios, 2021), a reduction in several cloud biases (Hentgen et al., 2019, Hohenegger et al., 2008), a higher precision in the spatial distribution of precipitation maxima, and enhancements in the daily patterns of precipitation (Hohenegger et al., 2008, Leutwyler et al., 2017).

In conclusion, it is of interest to conduct higher-resolution simulations using the HARMONIE-AROME model, as this could enhance the spatial details, improve the depiction of terrain variations, and offer a more precise representation of convective motion in the atmosphere.

Models that already run at resolutions on the order of 10 m are Large-Eddy simulations (LES). At these resolutions, convection and even most of the diffusive turbulent motion can explicitly be resolved, and residual turbulence is assumed to be very small, homogeneous, and isotropic in the three dimensions (Honnert et al., 2020). These are currently mainly used on small domain sizes and limited runtime to study turbulent processes and complement experimental data (Honnert et al., 2011). The computational power currently available is insufficient to enable the use of large-eddy simulation techniques for any purpose beyond that of a research environment (Kealy, 2019).

3.2. Problem

3.2.1. The Grey Zone of turbulence

The resulting resolutions of interest are those between the HARMONIE mesoscale and the LES microscale. This is shown schematically in figure 3.1.

The first figure (3.1i) represents a microscale resolution. The length scale of the grid boxes is significantly smaller than the characteristic length-scale of the turbulent motion, and the model is able to explicitly resolve this motion.

The third figure (3.1iii) represents a mesoscale model. The length-scale of the grid boxes is significantly larger than the characteristic length-scale of the turbulent motion. The motion is sub-grid and thus fully parameterized.

The intermediate resolution is shown in the second figure. Here, the length-scale of the grid boxes is close to the characteristic length-scale of the turbulent motion, causing the turbulence to be neither explicitly resolved nor fully parameterized. This phenomenon was first studied by Wyngaard (2004), who described it as 'Terra Incognita'. Later research extended this idea to the 'Grey zone' of turbulence, focusing on the CBL (Honnert et al., 2020). This Grey zone is thus not a fixed regime of resolutions, as the regime in which the grid spacing l is approximately equal to the characteristic length scale l_t of the turbulent motion differs for smaller, diffuse eddies compared to larger, convective cells. For instance, as the current resolution of the HARMONIE model would be increased from 2km, it will operate first the Grey zone of the shallow cumulus convection, and with further increase, the Grey zone of diffuse turbulence will be entered. This is illustrated in figure 3.2.

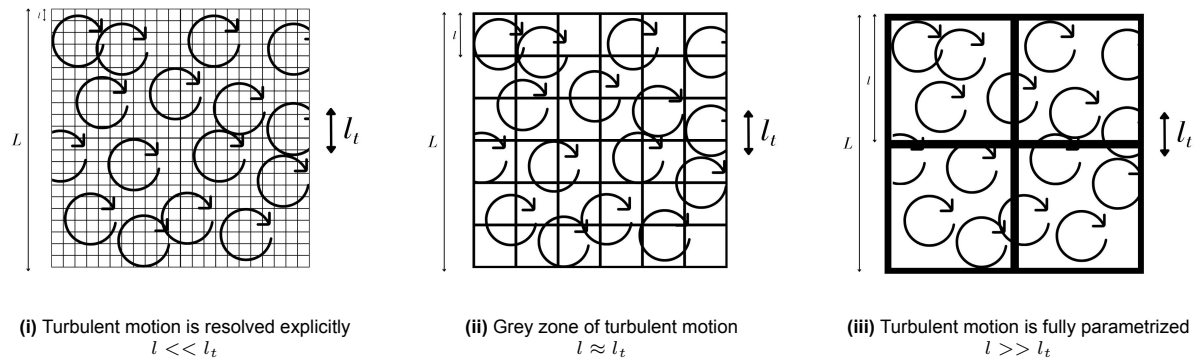


Figure 3.1: Schematic representation of the Grey Zone of turbulence

Wyngaard (2004) found that when the size of the largest turbulence structures in the ABL is of the same order as the model grid spacing, the basic assumptions underlying conventional turbulence parameterisations are violated, creating this problematic area of modelling. The reason that these assumptions no longer hold, is because they are based on a grid spacing much larger than the dominant turbulence length scale. From this, it is assumed that the representation of turbulence by parameterization schemes is not strongly dependent on the resolution. In the Grey zone, this no longer holds and the subgrid turbulence may be scale dependent. Additionally, the assumption is made that the turbulent transport is anisotropic, with a dominant vertical component. Resulting in a one-dimensional representation in the parameterization schemes. As the scale of subgrid turbulence become smaller with

increasing resolution, this assumption may no longer hold. Moreover, the subgrid convective motion is represented by the Mass-Flux approach, under the assumptions that the plume area cover is much less than unity and that the plume updraft and subsidence add up to a mean vertical velocity of zero. Both assumptions do not hold in the Grey zone, where the length scale of the plume is of the order of the grid spacing (Honnert et al., 2020).

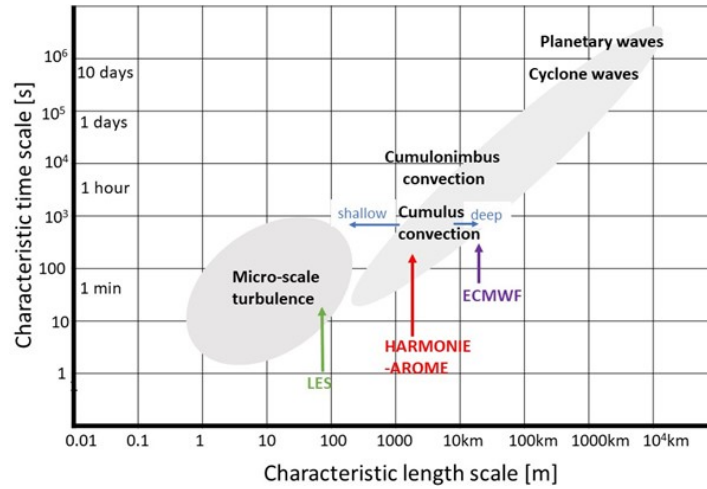


Figure 3.2: Different temporal and spatial scale of atmospheric dynamics, with the resolution of different atmospheric models indicated

3.2.2. Studying the Grey zone

In an attempt to gain more insight into this problematic region of CBL modeling, Honnert et al. (2011) investigated the transition of turbulent fluxes in the CBL through the Grey Zone by coarse-graining LES data from microscale to mesoscale resolution.

As discussed above, the turbulent motion in the CBL is partially resolved and partially unresolved in the Grey Zone. Therefore, by using the LES data to determine the resolved and unresolved components of the total turbulence for each resolution, the study quantified a relationship between their partitioning and the effective horizontal grid spacing within this Grey Zone. The Grey Zone is not a fixed region, as it depends on both the grid spacing and the characteristic length scale of the turbulent motion, which can vary significantly with different atmospheric conditions (Stull and Ahrens, 1995). To find a general form of these partitioning relations for different atmospheric conditions and turbulent transport of various variables, the grid spacing is normalized by the characteristic length scale of the turbulent motion using the similarity theorem (Buckingham, 1914). Based on the idea that the horizontal magnitude of the largest structures in the CBL is closely related to their vertical extent, the dominant length scale of turbulent motion in the CBL is assumed to be represented by the depth of the CBL in convective cases or the top of the cloud layer in shallow cumulus cases. From this, the horizontal grid-spacing (Δx) is normalized by the height of the boundary layer (h), or the height of the cloud top (h_c), this referred to as the similarity parameter (Honnert et al., 2011).

Plotting the resolved and unresolved partitioning to the total turbulence against this normalized horizontal resolution, partial similarity functions were found to hold for dry and cloudy cases. The functions were determined for the resolved and unresolved parts of the TKE, the temperature and moisture fluxes, and the potential temperature and water vapor mixing ratio variances. With this, a new diagnostic method to evaluate the Grey zone of turbulence in the CBL was found. Figure 3.3 shows an example of the results found by Honnert et al., 2011, at heights between 0.05 and 0.85 times the height of the CBL. It shows the resolved partitionings to the humidity flux in the red to yellow shades, where each shade depicts a different convective case. In the darker, purple to green shades, the unresolved partitionings are shown for the various cases. Each partitioning is plotted against its similarity parameter, denoted as $\Delta x / (h + h_c)$. From the combined results, the found similarity function of the humidity flux is plotted with the solid black line, with its first and last vigintiles in depicted with the finer black lines. Two vertical lines are shown in purple and green, the purple line depicts the intersection of the resolved and the unresolved partitioning functions. It represents the dimensionless grid-size at

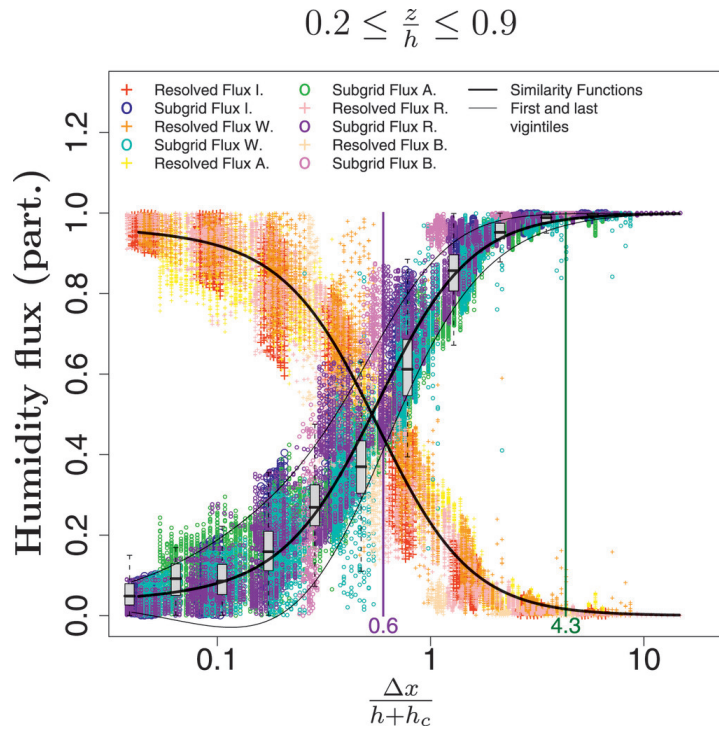


Figure 3.3: Partition of the resolved and unresolved humidity flux, $0.2 \leq \frac{\Delta x}{h+h_c} \leq 0.9$ (Honnert et al., 2011)

which the resolved part contributes the same amount to the total as the unresolved, or sub-grid. The green line shows the effective resolution where the resolved partitioning no longer decreases and is at its minimum. It represents the dimensionless grid-size at which the turbulence is completely subgrid. For both lines, a larger value indicates a larger structure, as a larger grid is needed for the structure to be partly or fully subgrid. This figure shows relatively consistent outcomes across various cases. On average, when the horizontal grid-spacing is 0.6 times the height of the boundary layer (including the cloud layer), the resolved humidity flux and the sub-grid flux contribute equally to the total. Additionally, it shows a horizontal grid-spacing of 4.3 times the height of the boundary layer needed for the turbulent structures to be fully subgrid. The Grey zone of turbulence in the CBL, for the turbulent transport of different variables, was determined to span grid spacings from $0.2(h + h_c)$ to $2(h + h_c)$. Comparing NWP simulations against these partitioning functions, demonstrated that none of these scheme could replicate a desired reduction in sub-grid partitioning as resolution increased.

From this, it is of interest to adapt turbulence schemes, while operating in the Grey zone.

3.2.3. Adaptations in the Grey zone

Attempts have already been made to adapt and extend a variety of turbulence parameterization schemes in the Grey zone in atmospheric modelling. These include, on the one hand, the extension of the parameterization schemes of the LES resolutions into the Grey zone regime, such as the Full Transport Model approach (Wyngaard, 2004, Hatlee and Wyngaard, 2007, Ramachandran and Wyngaard, 2011), which can be seen as an extension of the general eddy diffusivity approach. A grid spacing dependence of the mixing length in TKE-based eddy diffusivity was also found and implemented (Kitamura, 2015, Kitamura, 2016, Zhang et al., 2018, Kurowski and Teixeira, 2018). Others extended the Smagorinsky scheme (Smagorinsky, 1963), either by bounding (G. A. Efstathiou and Beare, 2015) or by applying scale dependence (G. Efstathiou et al., 2018) to the scheme. These adaptations proved successful in extending diffuse turbulence from the isotropic LES region into the more anisotropic region, but failed to represent organized updrafts (Honnert et al., 2020).

More promising showed to be attempts to adapt and extend the mesoscale schemes to higher resolutions. They retain the one-dimensional representation of turbulence in the CBL and focus primarily on reducing the convective parameterization. Particularly relevant to this study is the adaptation of the EDMF-scheme done by Lancz et al. (2018). In the EDMF-scheme, small-scale, diffuse turbulence and the larger-scale, organized convection, are naturally separated, which allows for separate downscaling in the Grey zone. And from the idea that the convective transport is dominant in the case of a CBL, the (single) mass-flux component was modified to be horizontally scale-aware based on the previously discussed partial similarity functions (Honnert et al., 2011). The surface initialization of the mass-flux was adapted, such that it scaled down, based on the relation between horizontal grid spacing and the height of the ABL ($h + h_c$). This approach ensured that the mass-flux updraft velocity decreased as the resolution relatively increased. These reduced updrafts allowed the model to resolve more convection by itself. The results of the adapted turbulence scheme showed positive change of the mean profiles of both subgrid and resolved turbulence for idealized cases, however, this is insufficient to conclude its efficacy. Scale-awareness based solely on the dominant vertical scale of the turbulent motion may not be sufficient. Savazzi et al. (2024) applied the LES coarse-graining method proposed by Honnert et al., 2011 to obtain partitioning functions of the subgrid turbulence, using the dimensionless grid spacing $\frac{\Delta x}{(h+h_c)}$. This was done on several cases of shallow cumulus convection, while separating them in degree of organization. This showed that in case of high organization, less of the turbulent flux was subgrid throughout the Grey zone than expected by the similarity function. Thus, more is resolved than expected, meaning that the scales are larger than estimated with $h + h_c$. Additionally, already at current HARMONIE operational resolution, it shows that the height of the CBL is not always a good measure of scale and organization. In cases with a low h compared to the grid spacing, the expectation from the similarity functions is that very little to nothing is resolved. However, looking at the vertical velocity, it shows that the model already starts to resolve larger and organized structures at this resolution. The convection scheme consumes instability, hampering this build-up of convection by the model, obstructing the organization of clouds and precipitation.

The height of the boundary layer may thus not be a reliable measure for turbulent length-scales. As a result, scale adaptation of the EDMF scheme in the Grey zone based solely on this height may be insufficient.

3.3. Aim and scope

As discussed, KNMI uses the HARMONIE-AROME model with an EDMF framework to parametrize subgrid turbulence in the CBL, and a shift to higher resolution in this model is of interest. However, it has been shown that this shift can lead to problematic areas of atmospheric modeling as it enters the Grey zone of turbulence in the CBL. From this, a method is proposed to quantify resolved and subgrid turbulence in the Grey zone against the grid-spacing relative to the height of the boundary layer, using LES-based coarse-graining. Subsequent changes to an EDMF parameterization scheme using this relation have shown some promising prospects, but are still in their infancy. This adaptation was applied on a single Mass-Flux scheme, whereas a Dual Mass-flux scheme is used for the HARMONIE model. Additionally, questions have been raised whether scaling down with the height of the boundary layer is sufficient.

Therefore, this study aims to investigate the scale-adaptivity of the HARMONIE EDMF-scheme in the grey zone of turbulence, for the shallow cumulus boundary layer.

The approach is two-fold. Firstly, LES is used to answer the following questions:

1. *Is the height of the mixed layer (h) expected to be an effective measure for scale-adaptivity of the dry mass-flux of the HARMONIE EDMF-scheme, in the Grey zone of turbulence?*
2. *Is the height of the cloud layer ($h + h_c$) expected to be an effective measure for scale-adaptivity of the moist mass-flux from the EDMF-scheme, in the Grey zone of turbulence?*

Following the method proposed by Honnert et al. (2011), the LES outputs are coarse-grained to quantify the resolved and unresolved partitionings to the total turbulence for heat, moisture, and momentum. In the mixed layer, it is investigated how these depend on the increasing filter-size, normalized with the height of the mixed layer (h). Similarly in the cloud layer, but here the increasing filter-size is normalized with the height of the cloud layer ($h + h_c$). Additionally, in both layer, these partitionings are decomposed to separately quantify the resolved and unresolved partitionings of the convective flux to the total turbulent flux.

Secondly, HARMONIE simulations are performed to review the expectations from LES results. The questions are asked:

3. *Do scale-adaptations on the dual mass-flux, based on h and $h + h_c$, improve the representation of turbulent transport from the HARMONIE model in the Grey zone of turbulence?*
4. *Does an additional vertical velocity threshold improve the representation of turbulent transport from the HARMONIE model in the Grey zone of turbulence?*

These are reviewed by running the HARMONIE model in the Grey zone of turbulence, at different EDMF-scheme settings. Firstly, it is run without adaptations. Then, scale-aware MF-scheme is applied based on the height of the boundary layer, using h for dry MF and $h + h_c$ for the moist MF. Additionally, a run is done using a threshold on the resolved vertical velocity, to shut down the MF as this threshold is exceeded. For all these run, performance is reviewed and compared with the found partitioning functions from the LES-based coarse-graining.

In this study, two benchmark simulations containing shallow cumulus clouds, are used. Both these cases, and the methods used to perform these examinations, are outlined in the next chapter.

4

Methodology

This chapter describes the method used to investigate the scale-adaptivity of the EDMF parametrization of the cloud model used by HARMONIE, in the Grey Zone of turbulence.

In the first section, 4.1, the benchmark simulations using Large Eddy Simulation (LES) are outlined. It gives a description of the LES model used, followed by a summary of the main LES settings and a case analysis of both selected cases. And concluded with the method of data points selection, and its following data points for both study cases.

The second section, 4.2, describes how this reference data is coarse-grained using a moving averaging method, and how the partitioning of the resolved and unresolved total turbulence is computed from this. Additionally, the method of decomposing these partitioning in convective and diffuse turbulent transport is discussed. Finally, the method for composing the dimensionless grid-size dependency of these partitionings is outlined.

In the last section, 4.3, the different settings and resolutions applied on the HARMONIE model, to compare with the found dimensionless grid-size dependencies of the partitionings of the turbulence, are given.

4.1. Benchmark simulations

To evaluate the scale-adaptivity of the EDMF parametrization scheme used by HARMONIE, Large Eddy Simulation (LES) results are used as a reference. For each case, this model can be tuned to specific settings. For instance, conditions at the surface and the top, lateral boundary conditions, and large-scale dynamics can be set, but also the domain, resolution and time-steps can be altered. Following is a description of the general settings used in the DALES simulations of the selected cases. Additionally, for each case, a short analysis of the observed vertical atmospheric profiles is discussed.

4.1.1. Cabauw case

To study a realistic shallow cumulus case, a mild summer day is selected with some shallow cumulus clouds and no precipitation: 16th of July 2022. The selected location is Cabauw in the Netherlands, a national location for meteorological measurements. An area of $15 \times 15 \times 13$ km is selected, sufficient to capture the scales of turbulent dynamics in the shallow cumulus boundary layer. The horizontal grid spacing is set at 19m, which has been shown to be more than sufficient for CBL modelling in previous studies (Honnert et al., 2011, Cheng et al., 2010, Sullivan and Patton, 2011). The vertical grid spacing is set at 20m, gradually increasing with height. The simulation was done for 24 hours, giving output every hour. The lateral boundary conditions are periodic, to simulate an infinite, repeating domain. The surface domain is homogeneous in land use, with the majority of the surface being grass. Surface fluxes are computed with the HTESSEL land surface scheme from ECMWF, using surface conditions from the ECMWF model. The dynamical tendencies are extracted from the HARMONIE model, and are imposed hourly in DALES as advection. The subgrid turbulence is computed using the Smagorinsky approach.

Case analyses

In figure 4.1, the vertical profiles of horizontal mean virtual potential temperature, the total specific humidity, liquid specific humidity, and its fluxes for each buoyant hour are shown. The vertical profile of the virtual potential temperature shows typical behavior for a summer day over land. Early in the morning, the surface is heated by the sun, enabling buoyant turbulence. This creates a well-mixed layer, resulting in a relatively homogeneous profile of temperature, capped with a layer of inversion. This mixed layer starts shallow in the morning, but quickly deepens up to approximately 1600m as the buoyancy increases with a continuously heated surface. The growth rate diminishes later in the day, as a substantially deeper layer requires more heating to grow compared to the early morning. After midday, a decrease in surface heating leads to a stabilization of temperatures, and a decrease in buoyancy flux. As there is not enough energy available to maintain the depth of the mixed layer, and it diminishes to lower heights. Looking at the profiles of the humidity, q_t and its fluxes, it shows that there is strong vertical transport of moisture in the morning, mixing the more humid air on the surface with drier air above, creating a near-homogeneous profile of q_t . This strong transport of moisture can lead to cloud formation at the heights where it is transported to, and indeed the liquid water specific humidity, q_l shows the condensation into liquid water at these heights. The clouds do not reach very deep, with peak depths of around 700m in the morning (8.00h, 9.00h, 10.00h). Looking back at the buoyancy flux, it shows that at most times, the clouds are not very buoyant as a lot of energy is needed to reach their LFC. After midday, the moisture flux from the surface decreases with an effective decreasing depth and magnitude of q_l , till the clouds are completely dissolved at 17.00h. In figure 4.2, the vertical profiles of the mean meridional and zonal velocities, and its fluxes are shown for each buoyant hour. The profiles of the wind's velocities show a Northwest wind blowing near the surface throughout the day. With the Northern wind growing more dominant during the morning. In the afternoon, both components slightly weaken and stabilize. After 8.00h, both wind velocities show near uniform profiles above the surface layer. However, at height above 1km, strong gradients of increasingly strong winds aloft show. These gradients enhance wind shear, stimulating the formation of turbulence.

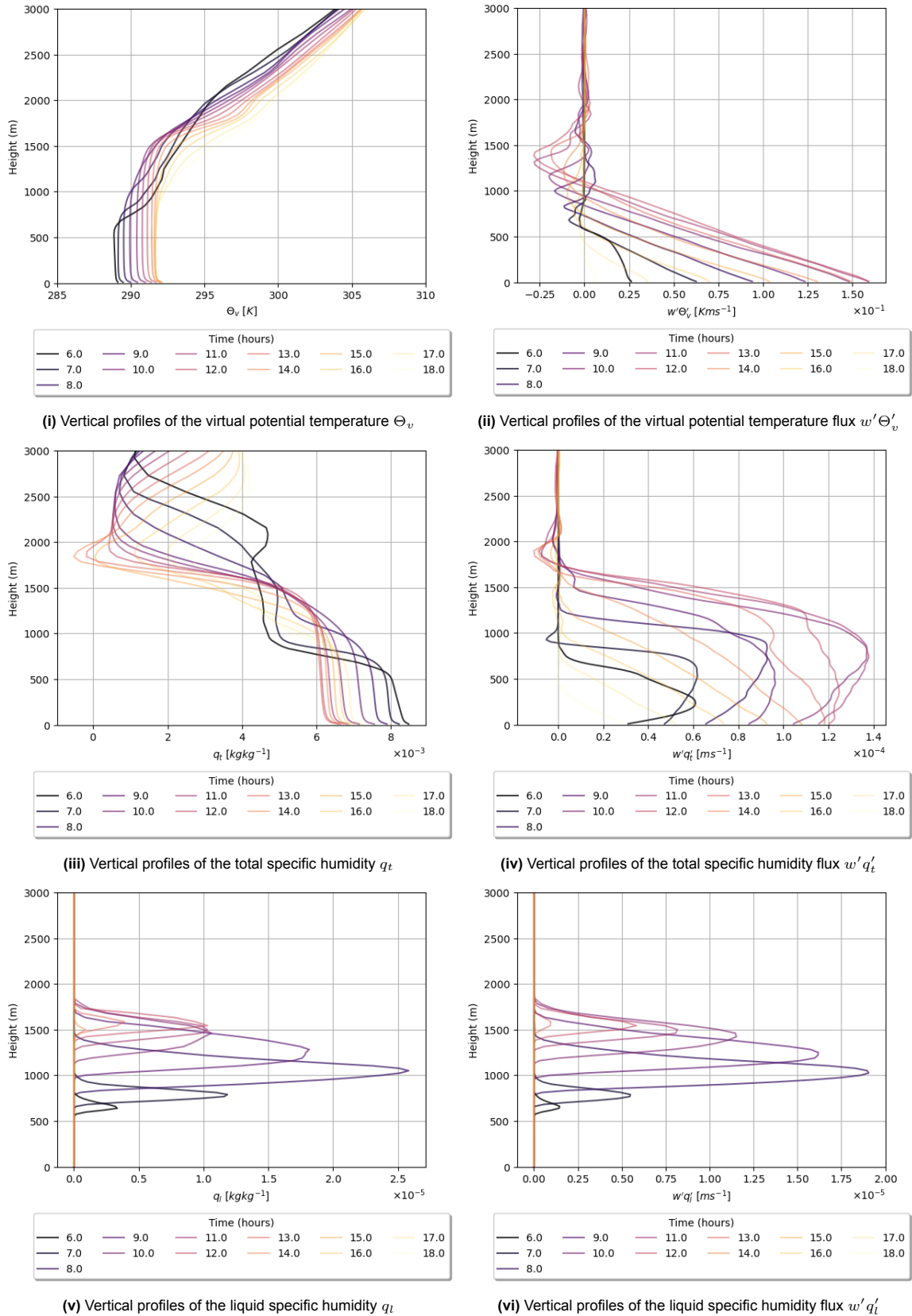


Figure 4.1: Vertical profiles of the horizontal mean values for temperature and moisture quantities of the Cabauw case (06-07-2022), with $t \in t_{buoyant}$

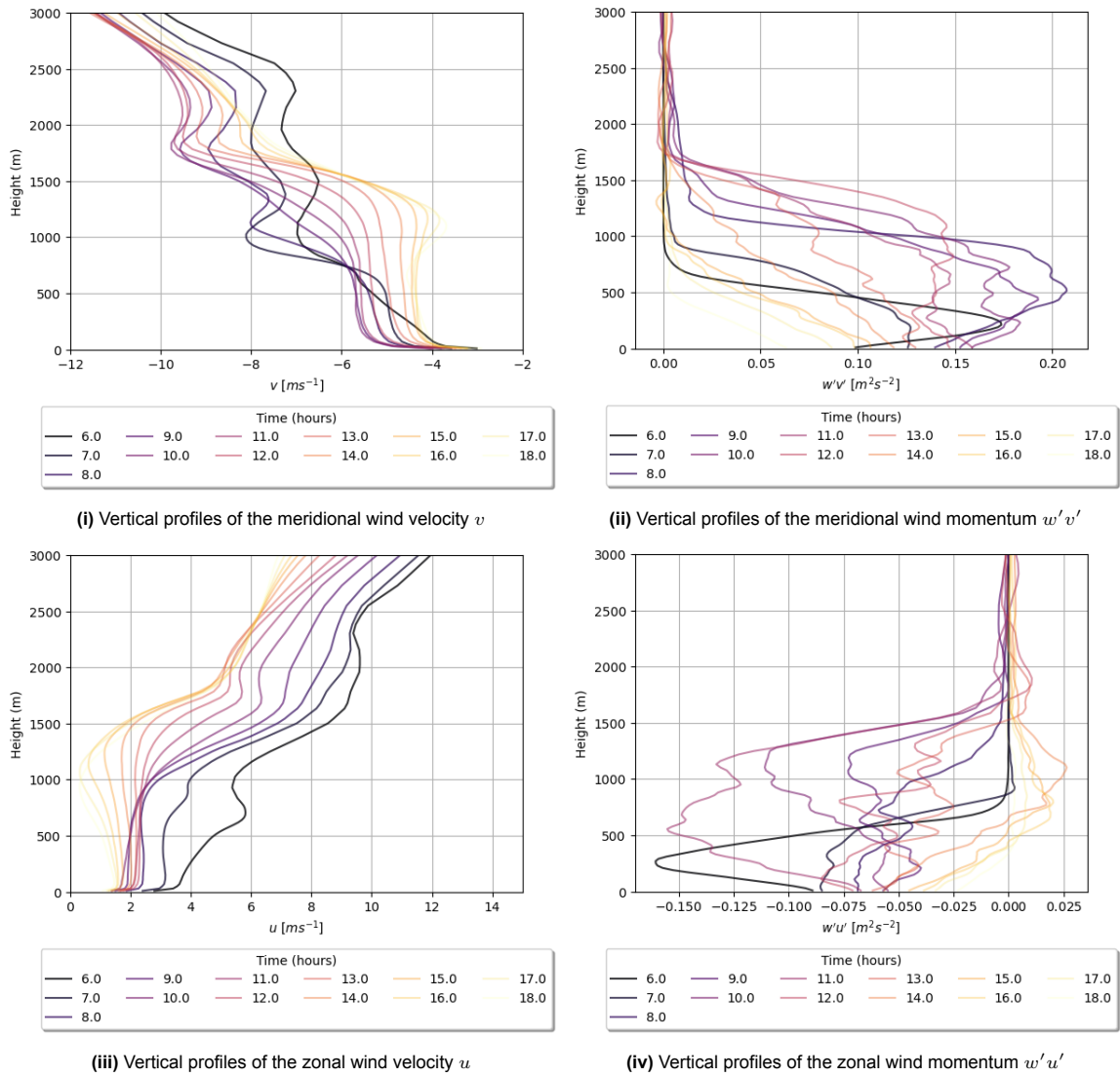


Figure 4.2: Vertical profiles of the horizontal mean values for wind quantities of the Cabauw case (06-07-2022), with $t \in t_{buoyant}$

4.1.2. BOMEX

During the Barbados Oceanographic and Meteorological Experiment (BOMEX), a phase of undisturbed, non-precipitating shallow cumulus clouds, capped by a pronounced trade wind inversion was observed (Holland and Rasmusson, 1973). This phase maintained in a consistent steady-state over five days, a condition that has been effectively simulated using LES and documented in various studies (Siebesma and Cuijpers, 1995).

This case was run on an $15 \times 15 \times 3.2$ km domain, sufficient to capture the dynamics of interest. With the horizontal grid spacing set to 19m and the vertical grid resolution at 40m. The simulation was done for 8 hours, giving output every half hour.

The initial conditions are based on two-days averaged rawinsonde observations from BOMEX, and include vertical profiles of temperature, humidity, and wind. The lateral boundary conditions are periodic, to simulate an infinite, repeating domain. At the top of the domain, a damping layer is applied to remove fluctuations of temperature, moisture, and wind velocity. Surface fluxes are parameterized with surface parametrization schemes from prescribed surface values of heat, moisture, and momentum based on observational data. To maintain steady-state conditions during the simulation period, a constant geostrophic wind to represent the background flow and a prescribed cooling rate to simulate radiative cooling are imposed on the simulation. The subgrid turbulence is determined using the Deardorff TKE closure scheme. A more extensive description of the simulation setup can be found from Siebesma and Cuijpers (1995).

Case analysis

In figure 4.3, the vertical profiles of horizontal mean virtual potential temperature, the total specific humidity, liquid specific humidity, and its fluxes for each buoyant hour are shown. As discussed, the BOMEX case is an oceanic case, in steady-state. The latter implies that the mean profiles of the conserved variables (Θ_v, q_t) show little to no change over time, as visible in figure 4.1i and 4.1iii. Both these variables show a strong gradient in the surface layer, followed by a mixed layer above. This is capped with a conditionally unstable layer, where clouds are formed (see profile q_l). On top of the clouds is an absolute stable inversion. In the first hours, these clouds grow deeper, reaching a continuous cloud layer of about 1.5km deep after the third hour. Looking back at the buoyancy flux, these clouds appear to be very buoyant. In figure 4.4, the vertical profiles of the mean meridional and zonal velocities, and its fluxes are shown for each buoyant hour. At the surface, the winds are dominantly Eastern throughout the simulation, with a weak Southern component. As the simulation continues, the latter becomes relatively stronger compared to the earlier hours. Over height, strong gradients are observed at the surface layer and between 500m and 1000m. These gradients enhance wind shear, stimulating the formation of turbulence. Above the mixed layer, the wind is assumed to be equal to the geostrophic wind (Siebesma and Cuijpers, 1995).

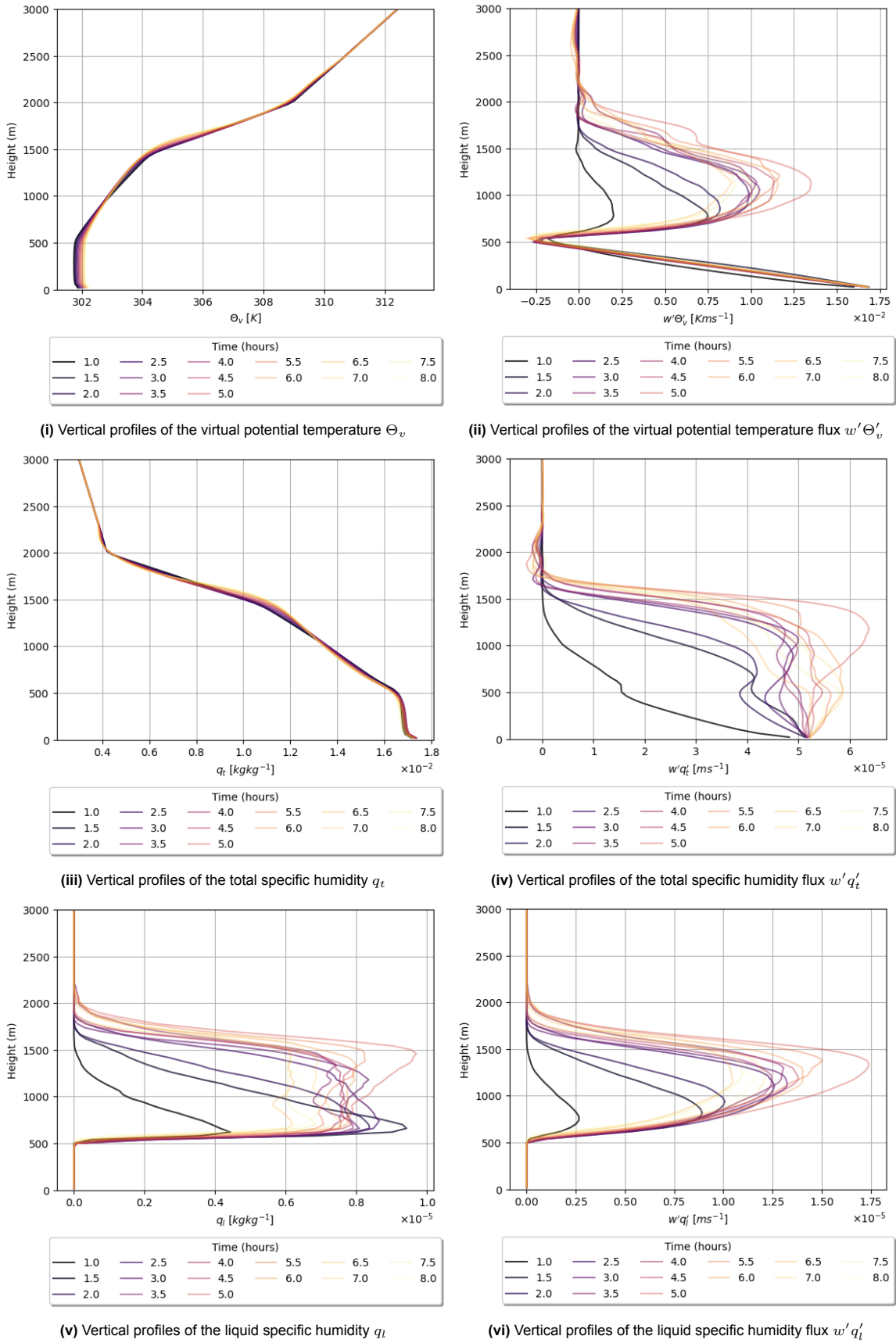


Figure 4.3: Vertical profiles of the horizontal mean values for temperature and moisture quantities of the BOMEX case (06-07-2022), with $t \in t_{buoyant}$

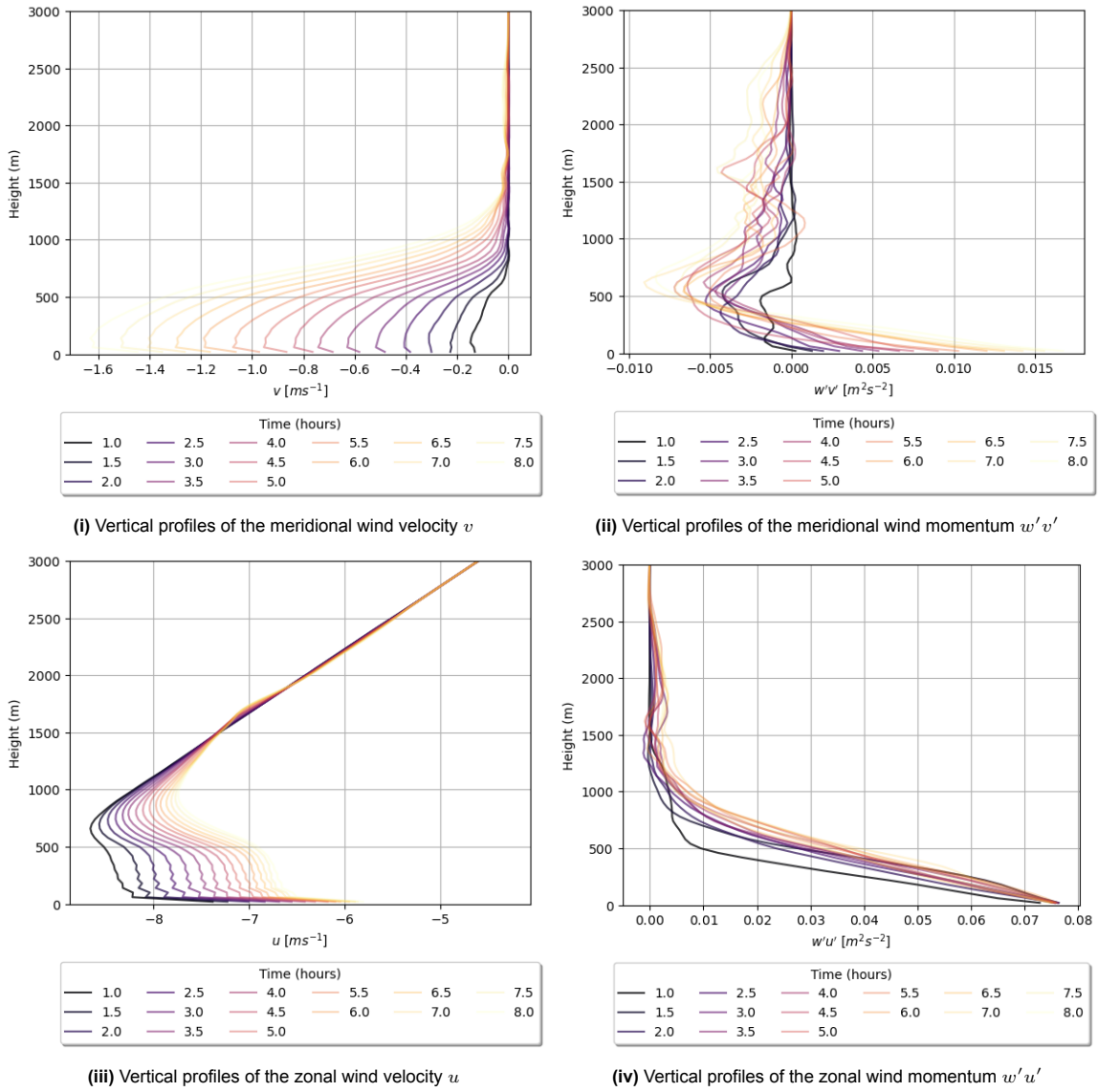


Figure 4.4: Vertical profiles of the horizontal mean values for wind quantities of the BOMEX case, with $t \in t_{buoyant}$

4.1.3. Data selection

The partitioning analysis of the resolved and unresolved turbulence is performed on the horizontal grid spacing. Both cases contain more than six thousand horizontal cross-sections over the simulated dataset. Thus, to sufficiently answer the question of research, while maintaining feasibility, a fixed number of data points throughout the dataset were determined.

As the aim is to study the scale-adaptivity of both the subcloud layer and the cloud layer, the selection includes multiple datapoints in both the mixed layer beneath the cloud layer and in the cloud layer.

For both the Cabauw and BOMEX case, this was done through a similar approach, regarding the mean vertical profiles over time.

1. Initializing:

First, the earliest time steps of the runs are omitted, as the LES model is still initializing.

2. Cloudy times:

Then, the times when the boundary layer is not cloudy are disregarded, as the shallow cumulus boundary layer is of interest. This is done by selecting only the times when water condensates to form cloud. A threshold is used for the liquid specific humidity: $q_l > 1e^{-6}$ kg/kg. This threshold is used in multiple atmospheric researches (R. Wang et al., 2022, Strauss et al., 2022), and also as the cloud base threshold in the ECMWF-IFS (European Centre for Medium Range Weather Forecasts Integrated Forecast System) (Kindlunth, 2020). Higher level clouds were filtered out by assuming low level cumulus clouds to have a cloud base height below 2000m (Kindlunth, 2020).

3. Mixing layer height h :

The height of the mixing layer h , or the LCL, is selected as the height where the water starts to condensate, using the threshold discussed above.

For each of the selected cloudy times, the locations within the mixing layer (z) are set at $\frac{1}{4}$, $\frac{1}{2}$ and $\frac{3}{4}$ of h .

4. Cloud height $h + h_c$:

The height of the cloud top is found by using the same threshold in reverse: selecting the highest level where $q_l > 1e^{-6}$ kg/kg. Again, higher level clouds are filtered out. Additionally, to exclude non-buoyant and fading clouds, the time steps when the cloud layer did not become sufficiently buoyant were disregarded. This was done by setting a threshold for a buoyant cloud, namely a positively buoyant cloud layer of at least 100m deep.

From this, the locations within the cloud ($z = h + z_c$) are set at $z_c = \frac{1}{4}h$, $z_c = \frac{1}{2}h$ and $z_c = \frac{3}{4}h_c$.

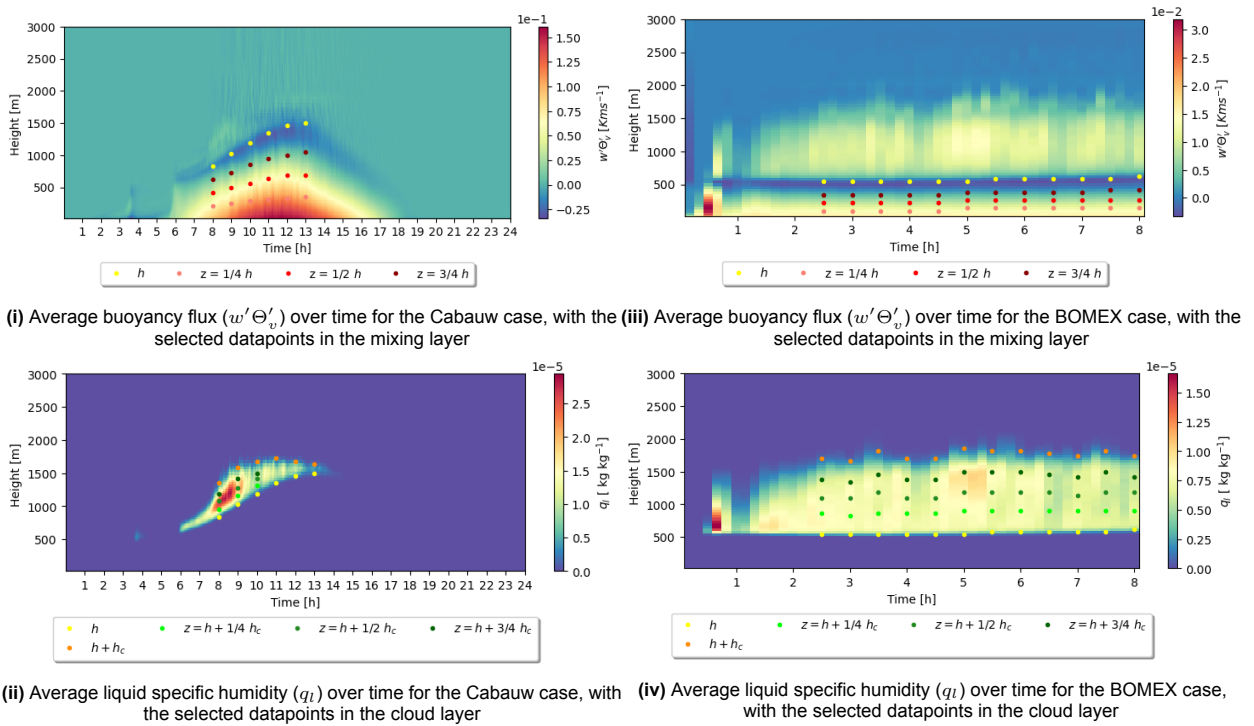
This gives the following locations in the datasets, shown in Table 4.1 and Table 4.2, and also visualized in Figure 4.5.

Table 4.1: Data point locations in the Cabauw dataset

Time [hh.mm]	h [m]	h_c [m]	$z = \frac{1}{4}h$ [m]	$z = \frac{1}{2}h$ [m]	$z = \frac{3}{4}h$ [m]	$z_c = \frac{1}{4}h_c$ [m]	$z_c = \frac{1}{2}h_c$ [m]	$z_c = \frac{3}{4}h_c$ [m]
08.00	835	1350	210	413	619	951	1077	189
09.00	1000	1587	251	494	725	1660	1104	1422
10.00	1160	1681	291	556	857	1315	1422	1501
11.00	1315	1731	311	640	951	-	-	-
12.00	1385	1681	331	682	1000	-	-	-
13.00	1422	1633	352	682	1051	-	-	-

Table 4.2: Data point locations in the BOMEX dataset

Time [hh.mm]	h [m]	h_c [m]	$z = \frac{1}{4}h$ [m]	$z = \frac{1}{2}h$ [m]	$z = \frac{3}{4}h$ [m]	$z_c = \frac{1}{4}h_c$ [m]	$z_c = \frac{1}{2}h_c$ [m]	$z_c = \frac{3}{4}h_c$ [m]
02.30	500	1700	100	220	340	860	1100	1380
03.00	500	1660	100	220	340	820	1100	1340
03.30	500	1820	100	220	340	860	1180	1460
04.00	500	1700	100	220	340	860	1100	1380
04.30	540	1700	100	220	340	900	1100	1380
05.00	540	1860	140	220	380	900	1180	1500
05.30	540	1820	140	260	380	900	1180	1500
06.00	540	1820	140	260	380	900	1180	1500
06.30	540	1780	140	260	380	900	1180	1460
07.00	540	1740	140	260	380	900	1140	1420
07.30	540	1820	140	260	420	900	1180	1500
08.00	540	1740	140	260	420	900	1180	1420

**Figure 4.5:** Visualization of the selected datapoints in the mixed layer and cloud layer, for the BOMEX and Cabauw case

4.2. Resolved and unresolved partitioning to the total turbulence

As explained in chapter 3, the Grey Zone of a process is located between the resolution where it is fully resolved, and the resolution where it is fully unresolved. As turbulent transport in the CBL is of interest, the Grey zone is located between the resolutions that are (1) such that turbulent transport can be resolved explicitly and (2) such that both diffuse and shallow convective transport should be parameterized. As described in 4.1, the grid size of LES is set at 19m for both cases. At this resolution, most of the total turbulent transport can be resolved, leaving just a small dissipation term to be unresolved. This is assumed to be the first resolution. As described in 2.3, the HARMONIE model runs at a grid spacing of 2km, at this resolution both the diffuse and the shallow convective transport is subgrid. It is thus assumed that this is the second resolution. How the grid-size dependency of turbulence in the shallow cumulus boundary is study throughout this regime, is outlined in this chapter.

4.2.1. Coarse-graining

To study the regime located between the two resolutions mentioned, the two-dimensional fields of the LES results are averaged to emulate the resolved fields of a simulation at lower resolutions, known as coarse-graining. This procedure was previously applied to studying parameterizations in atmospheric modeling by Shutts and Palmer (2007), Honnert et al. (2011), Shin and Hong (2013) and Honnert (2018). However, these studies differ in their method of averaging, proposing using a top-hat filter, moving averaging, a Gaussian Filter, and spectral averaging. The top-hat filter is relatively straightforward to implement, and the rectangular function is very grid-like, making it suitable for comparison with NWP model simulations. However, the placement of the filter can significantly impact the averaged values; including or excluding local extrema within a 'hat' can have strong effects on its average. The moving averaging method is similar to the top-hat filter, but the positioning of the filter is moved throughout the area, with the average of all the possible outcomes as the results. The resulting field is less easily interpretable than the top-hat filter but discharges the previously mentioned potential problems. Using a Gaussian filter to average the atmospheric fields may generate structures that are closer to reality than those generated by the top-hat and moving average filter. Also, it allows for straightforward analyses in the frequency domain. The downside of this method is that the rate of averaging accelerates as the filter size increases (Honnert, 2018). Additionally, the effects of the filtering are less easy to interpret and less consistent with the grid structure of the model itself. Similarly, using spectral averaging provides a natural interpretation of the averaging in frequency space. But again, the interpretability and consistency with the model grid are less than that for a top-hat or moving average method. In this research, the moving average method is applied as the coarse-grain method. This is because the representation of and comparison with the gridded NWP model is of interest. Additionally, the interpretability and computational efficiency of this method were advantages taken into account.

The moving average method can be interpreted as follows. The resolution of LES is represented with the length scale of its grid boxes, Δx . The total domain is the horizontal two-dimensional area of the model output, represented with a length scale L . These two length scales are schematically represented in figure 4.6.

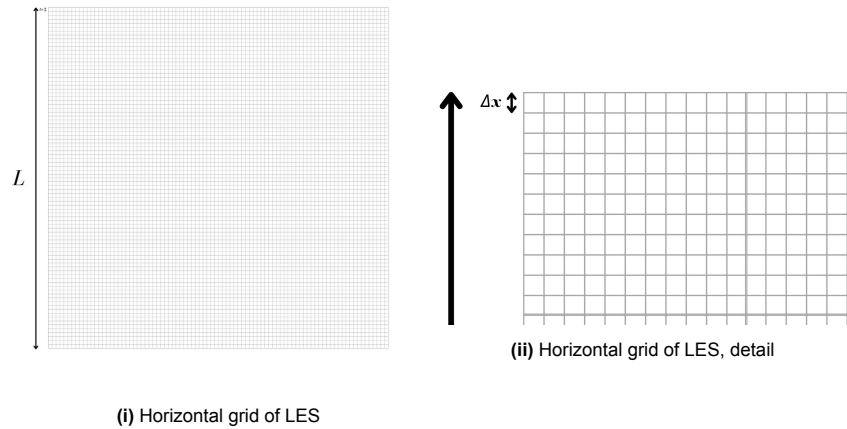


Figure 4.6: Schematic visualization of LES 2D-grid

For both cases, this domain length scale is $L = 15\text{km}$. Proposing a grid box with a horizontal equal to this length scale, guarantees all turbulence to be subgrid. From this, a third length-scale l is introduced, ranging between these the two length scales Δx and L . An averaging filter with a grid-spacing of $l \times l$ is applied over the LES domain with the original grid size. This gives the average of the LES values that are included in each $l \times l$ grid-box. As the domain is filled with these averages, it creates a new coarse-grained field, imposing the same domain on a lower resolution. This is shown schematically in figure 4.7: 4.7i shows the unfiltered LES field, 4.7ii to 4.7v show the LES field with the averaging filter applied, with increasing l . The latter represents a grid-spacing equal to the domain length scale L .

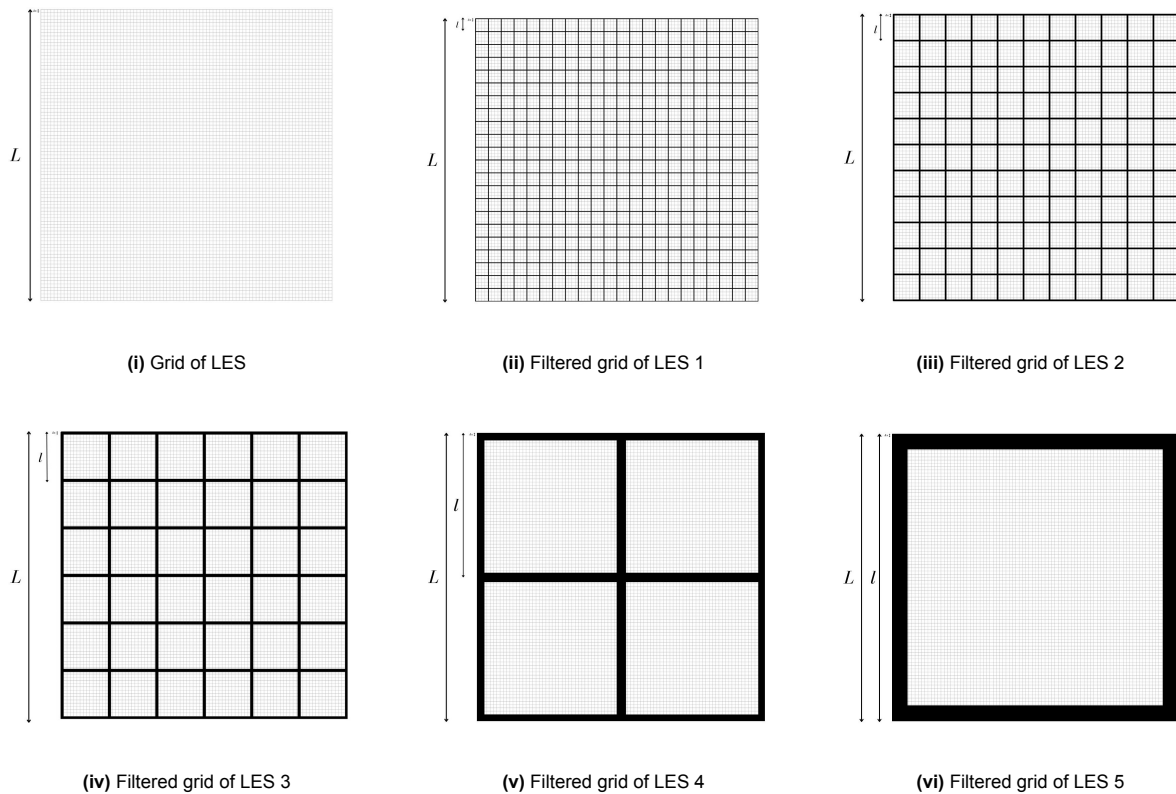


Figure 4.7: Coarse-grained LES output with increasing filtersizes

The moving average method moves these filters to all possible positions over the entire field, and the average of all the outcomes is taken as the result. Note that this is just a representation of the method.

The lengths of l are chosen to always be a multiplication of the original LES length-scale Δx , and to ensure optimal comparison possibilities, these multiplication factors are chosen to be the same for each case. These are the composed by taking the results function 1.6^i , with $i \in \{0, 1, \dots, 16\}$, and rounding up to one decimal. The result of this method are shown in table 4.3.

Note that while coarse graining from Δx to L , the order of magnitude of the HARMONIE model grid spacing is encountered. This ensures that the regime between the LES resolution and the HARMONIE resolution can be studied.

Table 4.3: Length scales for different multiplication factors

Exponent i (-)	Multiplication Factor (f) $f \approx 1.6^i$ (-)	Resulting length scale (l) $l = f \cdot \Delta x$ (m)
0	1.0	19.0
1	2.0	38.0
2	3.0	57.0
3	4.0	76.0
4	7.0	133.0
5	10.0	190.0
6	17.0	323.0
7	27.0	513.0
8	43.0	817.0
9	69.0	1311.0
10	110.0	2090.0
11	176.0	3344.0
12	281.0	5339.0
13	450.0	8550.0
14	721.0	13699.0
15	1153.0	21907.0

4.2.2. Total resolved and unresolved

In this chapter, the steps for computing the resolved and unresolved part of the turbulence on a two-dimensional field, using moving averaging method to coarse-grain, are outlined. In these computations, the following indicators are used:

- φ' Implies the 'true' fluctuation
- $\langle \varphi \rangle$ Implies the mean over the whole domain.
- $\bar{\varphi}$ Implies the resolved value
- $\tilde{\varphi}$ Implies the resolved fluctuation from the domain mean

When the latter three are superscripted with l , it refers to the value from the averaging filter. For example, $\bar{\varphi}^l$ refers to the average over the filter grid with length scale l , interpreted as the resolved grid value.

1. Coarse-grained fields at grid size l :

The moving average method is applied to the selected horizontal cross-sections of the prognostic variables of the model, with a filter length-scale l . The number of grid-boxes of the filter is expressed with I_l , shown in equation 4.1.

$$I_l = \left(\frac{L}{l}\right)^2 \quad (4.1)$$

The index of a single filtered grid-box is expressed with i . The average of all included resolved LES values within this grid-box of length l is referred to as the resolved value of this grid-box. This is denoted with an overbar, shown in equation 4.2.

$$\bar{\varphi}_i^l \text{ with } \varphi \in \{\Theta_l, q_t, q_l, w, u, v\} \quad (4.2)$$

2. Coarse-grained fluctuation fields at grid size l :

With these resolved fields, the resolved fluctuations are defined for each variable by subtracting the total mean of the domain. The mean of the domain is indicated with angle brackets. The mean of the filtered domain is by definition of averaging always equal to the mean of the LES domain.

$$\langle \bar{\varphi} \rangle^l = \frac{1}{I_l} \sum_{i=0}^{I_l} \bar{\varphi}_i^l = \langle \bar{\varphi} \rangle \quad (4.3)$$

The fluctuation from the mean at the filtered grid-box is, referred to as the resolved fluctuation, is expressed with a tilde, shown in equation 4.4.

$$\tilde{\varphi}_i^l = \bar{\varphi}_i^l - \langle \bar{\varphi} \rangle \quad (4.4)$$

3. Coarse-grained flux fields at grid size l :

The resolved turbulent flux can now be computed, by applying equation 4.4 to the vertical wind velocity w .

$$\tilde{w}_i^l \tilde{\varphi}_i^l = (\bar{w}_i^l - \langle \bar{w} \rangle)(\bar{\varphi}_i^l - \langle \bar{\varphi} \rangle) \quad (4.5)$$

With the average resolved turbulent over the whole domain:

$$\langle \tilde{w} \tilde{\varphi} \rangle^l = \frac{1}{I_l} \sum_{i=0}^{I_l} [(\bar{w}_i^l - \langle \bar{w} \rangle)(\bar{\varphi}_i^l - \langle \bar{\varphi} \rangle)] \quad (4.6)$$

4. **Repeat at LES resolution** $l = \Delta x$:

Applying these to the original grid size of the LES run $l = \Delta x$ gives

$$I_{les} = \left(\frac{L}{\Delta x}\right)^2 \quad (4.7)$$

$$\langle \tilde{w}\tilde{\varphi} \rangle^{l=\Delta x} = \frac{1}{I_{les}} \sum_{i=0}^{I_{les}} [(\bar{w}_i^{l=\Delta x} - \langle w \rangle)(\bar{\varphi}_i^{l=\Delta x} - \langle \varphi \rangle)] \quad (4.8)$$

Which can be written as

$$\langle \tilde{w}\tilde{\varphi} \rangle = \frac{1}{I_{les}} \sum_{i=0}^{I_{les}} [(\bar{w}_i - \langle w \rangle)(\bar{\varphi}_i - \langle \varphi \rangle)] \quad (4.9)$$

This is the resolved turbulent transport at the highest resolution, however, as discussed in chapter 2.4, not all turbulence can be resolved and a small part remains to be parametrized. Thus, the “true” total turbulence can be expressed with equation 4.10.

$$\langle w'\varphi' \rangle = \langle \tilde{w}\tilde{\varphi} \rangle + \text{subgrid flux} \quad (4.10)$$

5. **Total, resolved and unresolved turbulence:**

Thus, the mean total flux can be defined with the fluctuations of the LES grid from the domain mean plus the subgrid flux.

$$\begin{aligned} \langle w'\varphi' \rangle_{\text{total}} &= \langle w'\varphi' \rangle \\ &= \frac{1}{I_{les}} \sum_{i=0}^{I_{les}} [(\bar{w}_i - \langle w \rangle)(\bar{\varphi}_i - \langle \varphi \rangle)] + \text{subgrid flux} \end{aligned} \quad (4.11)$$

and the mean resolved flux at l can be defined with the fluctuations of the filtered grids from the domain mean.

$$\begin{aligned} \langle w'\varphi' \rangle_{\text{res}}(l) &= \langle \tilde{w}\tilde{\varphi} \rangle^l \\ &= \frac{1}{I_l} \sum_{i=0}^{I_l} [(\bar{w}_i - \langle w \rangle)(\bar{\varphi}_i - \langle \varphi \rangle)] \end{aligned} \quad (4.12)$$

From these, the unresolved flux at l can be obtained, as the total flux minus the resolved flux at this filter resolution.

$$\begin{aligned} \langle w'\varphi' \rangle_{\text{unres}}(l) &= \langle w'\varphi' \rangle_{\text{total}} - \langle w'\varphi' \rangle_{\text{res}}(l) \\ &= \frac{1}{I_{les}} \sum_{i=0}^{I_{les}} [(\bar{w}_i - \langle w \rangle)(\bar{\varphi}_i - \langle \varphi \rangle)] - \frac{1}{I_l} \sum_{i=0}^{I_l} [(\bar{w}_i - \langle w \rangle)(\bar{\varphi}_i - \langle \varphi \rangle)] + \text{subgrid flux} \end{aligned} \quad (4.13)$$

Thus, by computing the grid values at LES resolution and at the filtered grid resolution, the ‘true’ mean total turbulent flux can be decomposed into the resolved and unresolved parts at every filter length-scale l .

4.2.3. Convective resolved and unresolved

This chapter outlines how the grid-size dependency of the resolved and subgrid turbulence, for convective turbulence separately, is examined throughout the Grey zone. First, it is explained how total turbulent flux is decomposed into convective updrafts and remaining diffuse turbulence, based on the mass-flux approach. Then, different methods for selecting the convective and diffuse turbulent grids with conditional sampling are proposed.

Mass-flux decomposition

To separately analyze the resolved and unresolved parts of the flux for convective transport, the total flux need to be decomposed. This decomposition is done closely following the decomposition on which the mass flux is found 2.14, shown again here:

$$\overline{w'\varphi'} = (1 - a)\overline{w'\varphi'^e} + a\overline{w'\varphi'^u} + a(1 - a)\overline{(w_u - w_e)(\varphi_u - \varphi_e)}$$

As discussed, the first term represents the small-scale, diffusive turbulence in the environment, the second term represents the small scale, diffusive turbulence in the updraft, and the third term represents the organized convective term with its compensating subsidence in the environment.

The latter is used to compute the resolved and unresolved convective turbulent transport. This is done in the following way.

1. Coarse-grained fields at grid size l :

From the first step of the decomposition of the resolved and unresolved flux, the coarse-grained field at a filtered grid-size l are expressed with:

$$\overline{\varphi}_i^l \text{ with } \varphi \in \{\Theta_l, q_t, q_l, w, u, v\} \quad (4.14)$$

Again, the number of grid-boxes of the filter is expressed with I_l , the index of a single filtered grid-box is expressed with i and the average of all included resolved LES values within this grid-box of length l is referred to as the resolved value of this grid-box and is denoted with an overbar.

2. Conditional sampling:

One these coarse-grained fields, conditional sampling is applied. By using threshold conditions, a grid is either defined as updraft or as environmental.

$$\overline{\varphi}_i^l \in \{\overline{\varphi}_{i,\text{updraft}}^l, \overline{\varphi}_{i,\text{environmental}}^l\} \quad (4.15)$$

The different possible threshold conditions for conditional sampling of updrafts are outlined in chapter 4.2.3.

3. Compute convective transport:

With the defined updraft and environmental grids, the third term of equation 2.14, the mass-flux term, is used to compute the resolved convective flux over the entire domain, for each l . Note that this is not done using the simplified mass-flux approach, applied in the EDMF-scheme. At higher resolutions of the averaging filter, the assumptions on which this simplification is built may no longer hold, see chapter 2.3.1.

The updraft fraction at a filtered grid-size l can be defined by dividing the number of updraft grid by the total number of grids:

$$\overline{a}_u^l = \frac{I_u}{I_l} \quad (4.16)$$

And the mean values over the updraft and environmental grids can be found with:

$$\begin{aligned}\bar{\varphi}_u^l &= \frac{1}{I_u} \sum_{i=0}^{I_u} \bar{\varphi}_{i,\text{updraft}}^l \\ \bar{\varphi}_e^l &= \frac{1}{I_e} \sum_{i=0}^{I_e} \bar{\varphi}_{i,\text{environment}}^l\end{aligned}\quad (4.17)$$

Where I_u and I_e are the amount of grid-boxes that are defined as updraft and environment, respectively.

From the averaging rules, the mean resolved convective flux at grid-size l can be found with:

$$\langle \tilde{w}\tilde{\varphi} \rangle_{\text{convective}}^l = \bar{a}_u^l (1 - \bar{a}_u^l) (\bar{w}_u^l - \bar{w}_e^l) (\bar{\varphi}_u^l - \bar{\varphi}_e^l) \quad (4.18)$$

By applying equation 4.17 to the vertical velocity and variable of interest, the mean of the resolved convective turbulent transport can be found for each filter resolution.

4. Repeat at LES resolution $l = \Delta x$:

Applying this method to the original grid-size of the LES run, gives the resolved convective turbulence at this finest resolution.

$$\langle \tilde{w}\tilde{\varphi} \rangle_{\text{convective}}^{l=\Delta x} = \bar{a}_u^{l=\Delta x} (1 - \bar{a}_u^{l=\Delta x}) (\bar{w}_u^{l=\Delta x} - \bar{w}_e^{l=\Delta x}) (\bar{\varphi}_u^{l=\Delta x} - \bar{\varphi}_e^{l=\Delta x}) \quad (4.19)$$

which can be written as,

$$\langle \tilde{w}\tilde{\varphi} \rangle_{\text{convective}} = \bar{a}_u (1 - \bar{a}_u) (\bar{w}_u - \bar{w}_e) (\bar{\varphi}_u - \bar{\varphi}_e) \quad (4.20)$$

5. Total resolved and unresolved convective turbulence:

Using the total 'true' flux from equation 4.10 together with the computations at LES resolution, the total convective and turbulence over the domain can be computed.

$$\begin{aligned}\langle w'\varphi' \rangle_{\text{total}} &= \langle w'\varphi' \rangle \\ &= \langle \tilde{w}\tilde{\varphi} \rangle + \text{subgrid flux}\end{aligned}\quad (4.21)$$

$$\begin{aligned}\langle w'\varphi' \rangle_{\text{con, total}} &= \langle \tilde{w}\tilde{\varphi} \rangle_{\text{convective}} \\ &= \bar{a}_u (1 - \bar{a}_u) (\bar{w}_u - \bar{w}_e) (\bar{\varphi}_u - \bar{\varphi}_e)\end{aligned}\quad (4.22)$$

The sub-grid values of the turbulent flux from the LES output can be ascribed to diffuse turbulence entirely, since they occur at very small scales. With equations 4.18 the resolved convective turbulence over the domain can be computed at each l :

$$\begin{aligned}\langle w'\varphi' \rangle_{\text{con, res}}(l) &= \langle \tilde{w}\tilde{\varphi} \rangle_{\text{convective}}^l \\ &= \bar{a}_u^l (1 - \bar{a}_u^l) (\bar{w}_u^l - \bar{w}_e^l) (\bar{\varphi}_u^l - \bar{\varphi}_e^l)\end{aligned}\quad (4.23)$$

Finally, from the total and the resolved convective turbulence, the unresolved convective turbulence can be computed at each l :

$$\langle w'\varphi' \rangle_{\text{con, unres}}(l) = \langle w'\varphi' \rangle_{\text{con, total}} - \langle w'\varphi' \rangle_{\text{con, res}}(l) \quad (4.24)$$

$$= [\bar{a}_u (1 - \bar{a}_u) (\bar{w}_u - \bar{w}_e) (\bar{\varphi}_u - \bar{\varphi}_e)] - [\bar{a}_u^l (1 - \bar{a}_u^l) (\bar{w}_u^l - \bar{w}_e^l) (\bar{\varphi}_u^l - \bar{\varphi}_e^l)] \quad (4.25)$$

Thus, for each resolution of l , the total flux over the L domain can be found (4.11), and this can be decomposed into the resolved (4.12) and the unresolved(4.13) flux. Additionally, the total convective flux over the L domain can be found (4.23), and this can be decomposed into the resolved (4.24) and the unresolved (4.25) flux. Additionally, these components of the variances of each variable can be computed similarly.

Conditional sampling

For the computations shown in the previous chapter, it is needed to define the grids that are updraft, and those that are environmental. This is done using conditional sampling; selecting the grids on the selected area that comply with one or more specific conditions. Thus, by selecting conditions for updraft grids, the grids that comply with these conditions are identified as updraft and the remaining grids are identified as environmental.

A clear distinction is made between conditional sampling of updraft grids in the dry CBL and in the cloud layer.

If the area of interest is located in the cloud layer, the selection is more straightforward, as the mass-flux approach is based on cloud modelling. From the organized nature of clouds, a natural decomposition of the cumulus updrafts from their surrounding environment is allowed. In this study, the cumulus updrafts grids are selected as the grids that contain liquid water and have a positive vertical velocity. This is referred to as updraft decomposition, and was first defined by Siebesma and Cuijpers, 1995.

Updraft decomposition

1. Selecting the grid boxes of the coarse-grained field that contain liquid water as active updraft by computing the saturation humidity ($\overline{q_{sat}^l}$) at each grid for the resolved field with the resolved liquid virtual temperature ($\overline{\Theta_{li}^l}$), the resolved total humidity ($\overline{q_{ti}^l}$) and the pressure (p) (Appendix ??). And selecting the grids where the total humidity is greater than this saturation humidity:

$$\overline{\varphi}_i^l = \begin{cases} \overline{\varphi}_{i,\text{liquid}}^l & \text{if } \overline{q_{ti}^l} > \overline{q_{sat}^l} \\ \overline{\varphi}_{i,\text{dry}}^l & \text{otherwise} \end{cases} \quad (4.26)$$

2. Selecting the grids that contain liquid water and where the vertical velocity is greater than zero as active updraft:

$$\overline{\varphi}_i^l = \begin{cases} \overline{\varphi}_{i,\text{updraft}}^l & \text{if } \overline{q_{ti}^l} > \overline{q_{sat}^l} \text{ and } \overline{w}_i^l > 0 \\ \overline{\varphi}_{i,\text{environment}}^l & \text{otherwise} \end{cases} \quad (4.27)$$

Eventhough the Mass-flux concept originates from cloud modeling, this equation is suitable to describe dry updrafts as well (Siebesma et al., 2007). Furthermore, it allows for a natural transition from the dry boundary layer to the cloud layer, since the updraft can be seen as the convective roots of cloudy updrafts (LeMone and Pennell, 1976). However, defining the updraft grids is somewhat more complicated than in the cloud layer. A method was proposed by Siebesma et al. (2007). Using typical length scales of thermals and positive anomalies in the vertical velocity as conditions to define these updrafts, they showed that the highest vertical velocities are mainly concentrated within these updrafts. By defining the p_{th} percentile value of the total w distribution at a certain height, $w_{p\%}(z)$, a threshold vertical velocity can be found. The grid points with a larger positive vertical velocity than this threshold can be defined as strong updrafts.

The values used for the percentile p range from 99% to 95%, implying fractional updraft area cover between 1% and 5%, consistent with observed fractional area cover of thermals using wavelet analysis (de Haij, 2005). The selection of updrafts in the CBL was repeated by Shin and Hong (2013), using the 90_{th} percentile of the vertical velocity as the threshold. Therefore, percentiles ranging from 90 to 99 are used.

Vertical velocity decomposition

Selecting the grid boxes of the coarse-grained field that have a larger positive vertical velocity than the p -percentile of the vertical velocity distribution at that height:

$$\overline{\varphi}_i^l = \begin{cases} \overline{\varphi}_{i,\text{updraft}}^l & \text{if } \overline{w}_i^l > w_{p\%} \text{ with } p \in [90..99] \\ \overline{\varphi}_{i,\text{environment}}^l & \text{otherwise} \end{cases} \quad (4.28)$$

4.2.4. Similarity parameter

With the methods proposed in previous chapters the selected horizontal fields of the LES benchmark simulation can be coarse-grained (4.2.1), these coarse-grained fields can be used to decompose the total flux into the resolved and unresolved partitioning (4.2.2), and this can be done for convective transport separately (4.2.3). By applying these computations on every filter grid-spacing proposed in table 4.3, the partitioning of the different components of the turbulent fluxes can be examining throughout the Grey zone regime of resolutions.

However, this partitioning is not independent of the scale of the turbulent structures, as explained in Chapter 3.2. Also discussed here, is the similarity parameter, proposed by Honnert et al. (2011) as a way to non-dimensionalize the grid spacing. This normalization is based on the idea that the dominant length scale of turbulent motion is well represented by the depth of the CBL in the convective (sub-cloud) layer and by the top of the cloud layer in shallow-cumulus cases. Setting out the resolved and unresolved contribution to the total turbulence against this similarity parameter, is thus expected to result in general relations (partial similarity functions) between these two, independent of the turbulent conditions. This would suggest that the EDMF scheme, which is currently employed outside the Grey zone in the HARMONIE model, could be scaled down using these similarity functions in order to adapt to resolutions within the Grey zone. An example of the moisture flux partitionings and its partial similarity functions, found by Honnert et al. (2011), can be found in 3.2, figure 3.3.

This research aims to find such scale-independent grid-size dependencies of turbulence in the shallow cumulus boundary layer, using a similar approach. As the interest is to separately scale down the dry and the moist mass-flux in the Dual Mass-Flux scheme, this is done separately in the mixed layer and in the cloud layer. For this similarity parameter, Honnert et al., 2011 used the coarse-graining grid-spacing, denoted with Δx , and the boundary layer height h and the height of the cloud layer h_c . In this research, the coarse-graining grid-spacing is used in the same way, but denoted with l , explained in chapter 4.2.1.

Thus, in the mixed layer, the resolved and the unresolved partitioning to the total flux or variance is set out against the filter-size, normalized with the height of the mixed layer.

$$\frac{l}{h} \quad (4.29)$$

where:

l is the coarse-graining grid-spacing

h is the mixed layer height

In the cloud layer, the resolved and the unresolved partitioning to the total flux or variance is set out against the filter-size, normalized with the height of the cloud layer.

$$\frac{l}{(h + h_c)} \quad (4.30)$$

where:

l is the coarse-graining grid-spacing

h is the mixed layer height

h_c is the depth of the cloud layer

Run	Case	Grid size [m]	Parametrization schemes
Run 1	Cabauw 16-07-2022	500	Original EDMF scheme
Run 2	Cabauw 16-07-2022	500	Scale-aware MF
Run 3	Cabauw 16-07-2022	500	Scale-aware MF + w_{\max}

Table 4.4: Different settings of the HARMONIE runs

4.3. HARMONIE simulations

As discussed, this research aims to use the LES results as a representative of the desired behavior of the turbulence parameterizations in the HARMONIE model. To this end, the results of the Cabauw case gained with the LES model are compared with the outputs of the HARMONIE model. This chapter outlines the different settings and resolutions applied on the HARMONIE model and gives a more detailed insight into the applied scale-aware EDMF-schemes.

4.3.1. Datapoints

The LES model results are obtained by coarse-graining the horizontal cross-sections at various points within the cloud and sub-cloud layers. To effectively compare these results with the HARMONIE simulations, datapoints must be chosen at comparable locations. Therefore, a similar method (as discussed in Chapter 4.1.3) for selecting these heights is applied to the HARMONIE results.

1. **Cloudy times:**

First, the times when the model does not show clouds are disregarded, as the shallow cumulus boundary layer is of interest.

2. **Mixing layer height h :**

Then, the height of the mixing layer h is found where the dry convection from the mass-flux scheme is equal to zero. For each of the selected buoyant times, the locations within the mixing layer (z) are set at $\frac{1}{4}$, $\frac{1}{2}$ and $\frac{3}{4}$ of h .

3. **Cloud height $h + h_c$:**

The height of the mixing layer h , is assumed to coincide with the LCL, the maximum height of the cloud is found where the moist updraft of the dual mass-flux determines to zero. From this, the locations within the cloud ($z = h + z_c$) are set at $z_c = \frac{1}{4}h$, $z_c = \frac{1}{2}h$ and $z_c = \frac{3}{4}h_c$.

4.3.2. Model settings

The HARMONIE model is run in the Grey zone of shallow cumulus turbulence, with different EDMF-scheme settings. As the Grey zone is expected to occur when the length scales of the turbulent motion are in the same order as the grid length scale, these runs are done at 500m horizontal grid-spacing. These 500m runs are done with the default convection parametrization as applied in the $2km$ runs and with two adapted mass-flux schemes, shown in table 4.4. These adapted mass-flux schemes are further explained in the next section, 4.3.3.

4.3.3. Adaptive convection scheme

The 500m run of the HARMONIE model is located in the Grey zone of shallow cumulus convection. Therefore, it is of interest to run this resolution with an adapted mass-flux scheme, to see if this increases the performance of the model. This adaptation is two-fold, and discussed here. First, the method proposed by Lancz et al. (2018) is outlined. This is a scale-adaptive mass-flux parametrization, dependent on horizontal resolution, based on the partitioning functions found by Honnert et al. (2011). Then, an addition to this scheme is proposed, by introducing a threshold value for convective vertical velocity. The simulation at a resolution of 500m of HARMONIE is done using solely the scale-aware scheme, as well as adding the vertical velocity threshold.

1. Scale-adaptive mass-flux scheme

Following the approach of Lancz et al. (2018), the mass flux in the convection scheme depends on the non-dimensionalized grid size. However, Harmonie-Arome uses a dual updraft mass flux scheme (Neggers et al., 2009, de Rooy et al., 2022) and scale-aware adaptation of the mass flux is done separately for the dry and moist convection.

$$M_{u,dry,scale-aware} = \tanh\left(1.86 \times \left(\frac{\sqrt{\Delta x \times \Delta y}}{h}\right)\right) \times M_{u,dry} \quad (4.31)$$

$$M_{u,moist,scale-aware} = \tanh\left(1.86 \times \left(\frac{\sqrt{\Delta x \times \Delta y}}{h + h_c}\right)\right) \times M_{u,moist} \quad (4.32)$$

2. Vertical velocity threshold

That is why a second modification to the mass-flux of the EDMF is proposed.

Khain et al. (2021) introduced a threshold value for the resolved vertical velocity w_{max} , which allowed turning off the convective parametrization in cases of grid scale updrafts stronger than this. High resolved vertical velocities can be seen as an indication that the model starts to resolve convection itself. Shutting down the convection parameterization with relatively strong resolved vertical velocities supports the model to build up resolved convection itself (and when it probably should). Khain et al., 2021 showed significant improvements of shallow convection modelling at a 2.5km grid-spacing, with an optimal result found at $w_{max} = 0.1\text{m/s}$. To this end, the same w_{max} is applied to the HARMONIE runs in the Grey zone of shallow cumulus convection. Thus, if the vertical velocity of the grid exceeds the threshold value (0.1m/s), the mass-flux scheme is turned off. If this is not the case, the scale-adaptive mass-flux scheme stays active:

$$\text{Mass flux scheme} = \begin{cases} \text{Scale-adaptive mass-flux scheme} & \text{if } |w_{resolved}|_{between0-7kmheight} \leq w_{max} \\ \text{mass-flux scheme off} & \text{if } |w_{resolved}|_{between0-7kmheight} > w_{max} \end{cases} \quad (4.33)$$

The threshold value is diagnosed between 0 – 7km because above this height high values can occur, but they are not related to surface-induced convection. Note that the absolute value of the resolved vertical velocity is taken, because downdrafts are considered as well.

5

Results and discussion

This chapter shows the results of the method proposed and discusses its outcomes. In the first chapter, the coarse-grained LES results are used to investigate the resolved and unresolved partitioning to the total variance and fluxes of the prognostic variables (q_t, Θ_l, u, w, v) against the normalized grid-size. For each flux, the convective partitioning to the total flux is studied separately. This is done both in the mixed layer, and in the cloud layer. In the second chapter, the HARMONIE simulations of the Cabauw case are reviewed. In particular, the effects of the Dual Mass-Flux scheme, at the different settings, on the partitioning of the resolved and unresolved flux are studied. These are compared with the partitioning functions found from the LES results. Again, the mixed layer and the cloud layer are treated separately.

5.1. Partitioning functions from LES

In this chapter, the partitionings of the resolved and unresolved variance and fluxes of the prognostic LES variables (q_t, Θ_l, u, w, v) are plotted against the normalized grid-size. In these figures, the hourly values of the resolved and unresolved partitioning to their total are depicted with patterned lines, which are dotted for the BOMEX case and dashed for the Cabauw case. The mean of these hourly partitioning values is represented with a solid line. Two values can be helpful indicators for the size of the structures considered. First, the intersection of the resolved and the unresolved mean partitioning functions. It represents the dimensionless grid-size at which the resolved flux or variance contributes the same amount to the total flux or variance as the unresolved, or sub-grid flux or variance. This scale is defined as I_{int} in this research. Larger values of I_{int} indicate larger structures carrying the flux or variance. A second indicator is the scale where the resolved partitioning no longer decreases and is at its minimum. It represents the dimensionless grid-size at which the turbulence is completely subgrid. A larger value indicates a larger grid needed for the entire structure to be subgrid, thus a larger structure. This scale is defined as I_{exc} in this research.

First, the resolved and the unresolved partitioning to the total variance (φ'^2) is reviewed for each variable. Then, focussing on the vertical turbulent transport, the resolved and the unresolved partitionings to the total flux ($w'\varphi'$) are examined. As the focus of this research is on the mass-flux component of the turbulent transport, the convective partitionings are shown separately. This is done first for the fluxes of the conserved variables, and then for the momentum fluxes. The mixed layer and the cloud layer are treated separately.

5.1.1. Mixed layer

In this section, the partitionings of the resolved and unresolved partitionings of the variances and fluxes are plotted against the grid-size, normalized with the height of the mixed layer (h).

Variances

In figures 5.1 the partitioning functions of the variance of the potential temperature, the total specific humidity, and the wind velocities are plotted against the grid size normalized with the height of the mixed layer. These figures illustrate that the variance in vertical velocity diminishes most rapidly as grid scales increase, suggesting smaller variance structures. The other two wind velocities decrease at a slower rate, comparable to each other, implying their variance is associated with larger, similarly sized structures. Both moisture and heat variances decrease more slowly than that of the wind velocities, with the moisture flux decreasing the slowest. The structures of variance in the specific humidity thus are larger than those of the potential temperature, which is in turn larger than the structures of horizontal winds and the vertical wind variance. These differentiating grid-size dependencies of the variances agree with those found from LES-based coarse-graining done by Honnert et al., 2011, who found the moisture flux to be resolved at grid scales larger than that of the potential temperature, which in turn was found to be mainly resolved at grid scales larger than that of the vertical velocity. Additionally, it is in agreement with studies done on the length scales of various quantities in the CBL by de Roode et al. (2004). Here, it was found that in the CBL, the transport of both the potential temperature and the specific humidity become gradually dominated by larger organized structures, while the vertical velocity fields are dominated by horizontal scales on the order of height of the boundary layer.

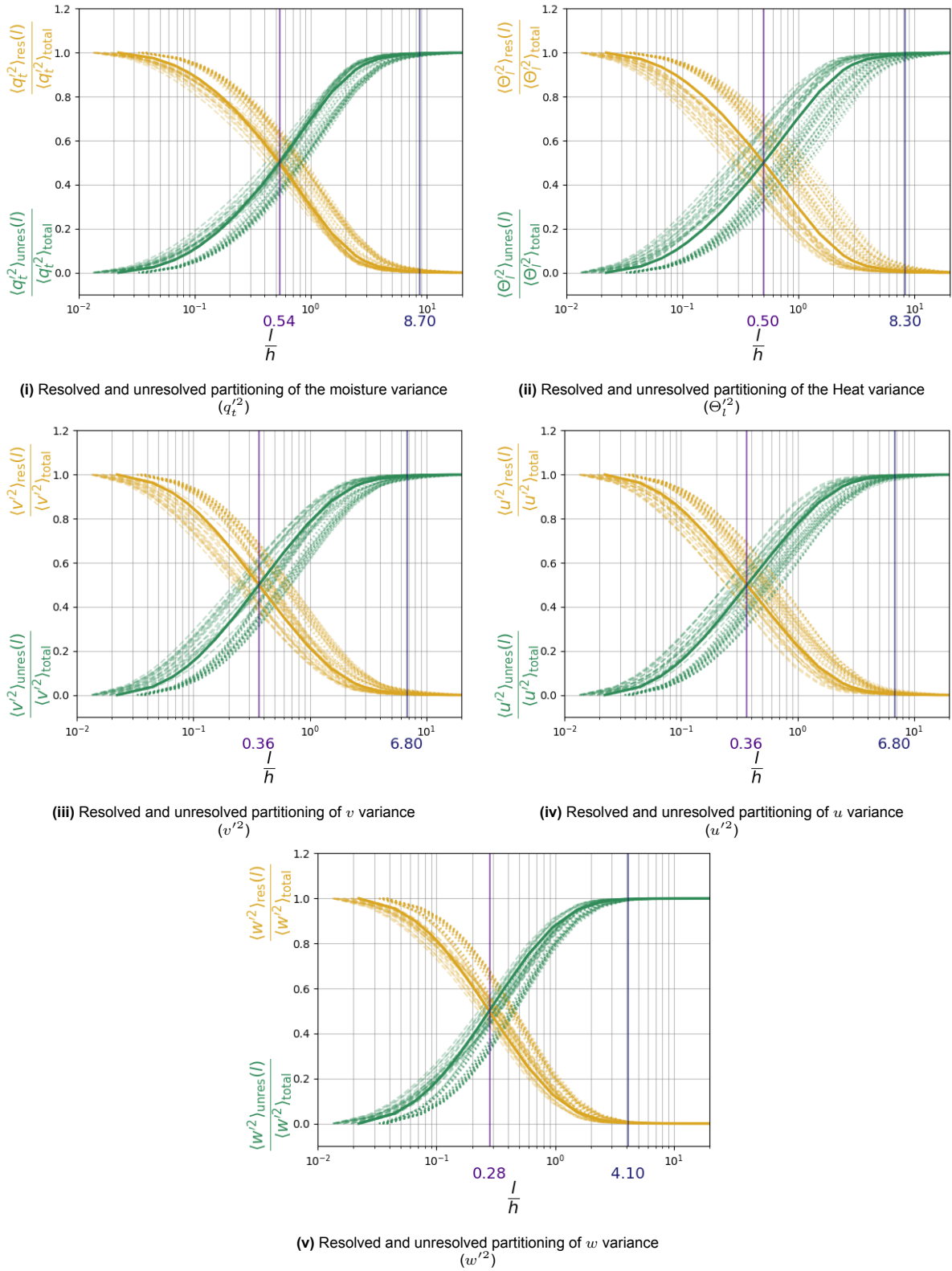


Figure 5.1: Partitioning functions variance, at $0.25 \leq \frac{z}{h} \leq 0.75$, with $t \in t_{cloudy}$. With the hourly (patterned) and mean (solid) partitionings of the resolved (yellow) and unresolved (green) variance. The dotted lines show the BOMEX results, and the dashed lines the Cabauw results. The indicators I_{int} and I_{exc} are depicted in light and dark purple

For these convective cases, the variance of the different quantities in the mixed layer is expected to be strongly correlated with the convective transport of these quantities, especially for the heat and temperature. Consequently, the scales of the variance structures are expected to scale well with the height of the mixed layer. Looking at figure 5.1, the variance of the moisture and the vertical velocity appear to scale well with the height of the mixed layer, showing very little spread in the partitionings. However, the horizontal wind velocities and the potential temperature variance show more spread, showing relatively larger structures for the BOMEX case than for the Cabauw case. This indicates that the dominant turbulent structures of these quantities correlate less with the height of the mixed layer. This may be explained by a relatively strong contribution of horizontal transport, which can be expected to transport momentum, as this is generally less dominantly transported by upwards convective motion. However, for the heat flux, this is much less expected.

Fluxes of conserved variables

In figure 5.2 the partitioning functions are shown for the moisture flux and the heat flux in the mixed layer. The two cases show very similar mean partitioning functions for the heat and humidity flux, indicating that on average over these two shallow cumulus cases, the heat and humidity flux are vertically transported on scales of similar size in the mixed layer. These structures appear to be relatively large, and thus suggesting these are convective structures. However, the spread of the heat flux shows to be much larger than for the moisture flux, which may explain the larger spread found in the variance of the heat flux (figure 5.1ii). Both the BOMEX and the Cabauw case unexpectedly show a large amount of remaining resolved heat flux, still at larger grid scales.

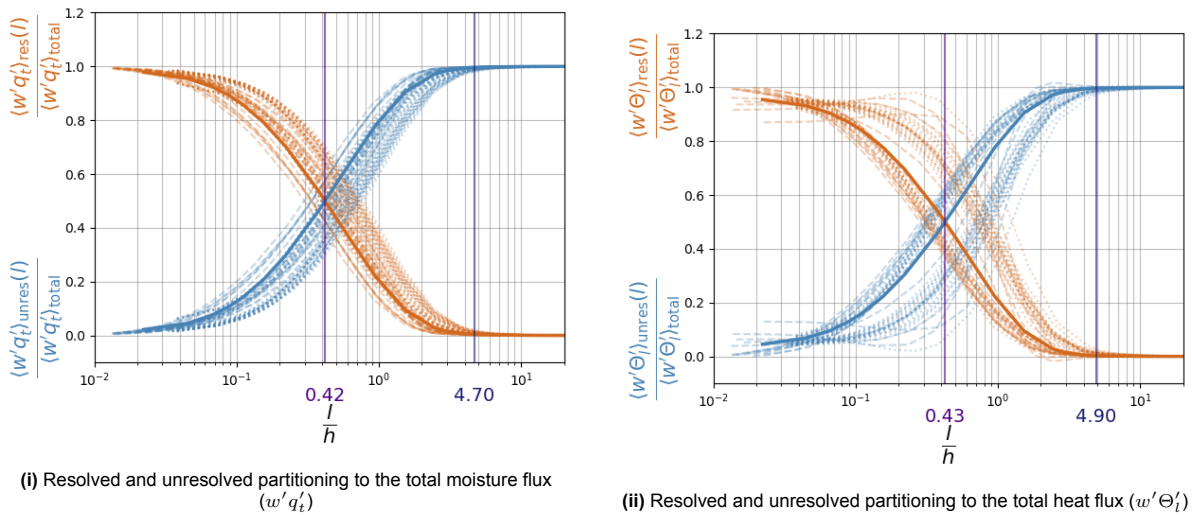


Figure 5.2: Partitioning functions, at $0.25 \leq \frac{z}{h} \leq 0.75$, with $t \in t_{cloudy}$.

With the hourly (patterned) and mean (solid) partitionings of the resolved (orange) and unresolved (blue) fluxes.

The dotted lines show the BOMEX results, and the dashed lines the Cabauw results.

The indicators I_{int} and I_{exc} are depicted in light and dark purple.

This large spread in the partitioning functions of the heat flux appear to be related to the height of the cross-sections, taken in the mixed layer. This is shown in figure 5.3, where the resolved and the unresolved partitioning to the total heat flux are depicted with a different color per location, separately for the BOMEX case and the Cabauw case.

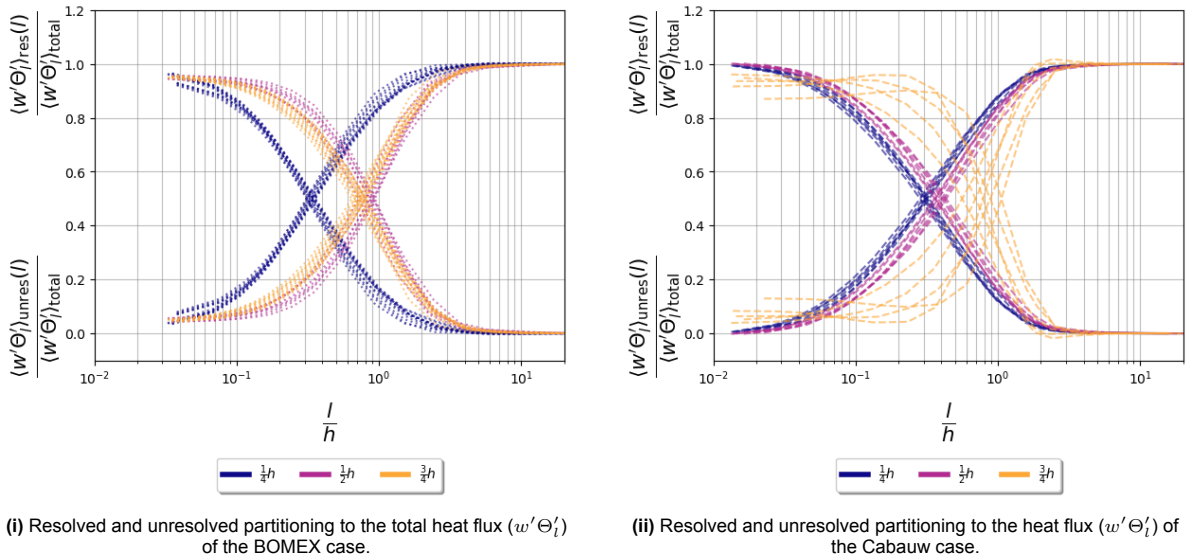


Figure 5.3: Hourly partitionings of the resolved and unresolved fluxes of the BOMEX and the Cabauw at $0.25 \leq \frac{z}{h} \leq 0.75$, with $t \in t_{cloudy}$. The different locations ($\frac{1}{4}h$, $\frac{1}{2}h$, and $\frac{3}{4}h$) in the mixed are depicted with blue, purple and yellow, respectively.

The figures illustrate the difference between the partitioning of the resolved and unresolved components of the total heat flux with respect to each location. It shows that, in both cases, the resolved partitioning to the total flux remains significantly higher with increasing grid spacing at locations higher in the mixed layer.

This could indicate much larger structures of heat flux at higher altitudes, that do not correlate well with the height of the mixed layer. However, another explanation could be the change in sign of the heat flux over the increasing height in the mixed layer. From the surface, warmer, lighter air is transported upwards throughout the mixed layer, creating a positive heat flux. When the air starts to condensate at the LCL, the air near this level is heated and the rising air now transports air with lower temperature than its surrounding, creating a negative flux. At locations higher in the mixed layer, some of this negative flux may start to contribute to the total flux at that height, together with positive heat flux from below. If these positive and the negative fluxes are carried on structures similar in size, coarse-graining these field may result in equal diminishing of the two. These can then counterbalance each other, leaving the mean resolved flux to be similar in magnitude to the total mean flux over a number of increasing filter sizes.

Convective flux of conserved variables

In figure 5.4, the partitionings of the convective flux to the total flux are shown, for the moisture flux (5.4i) and the heat flux (5.2ii). Here, the updrafts are selected with $p = 90$ (Appendix B). Comparing these to the partitioning functions of the total resolved flux in figure 5.2, similar behavior shows for both fluxes: the convective moisture flux scales well with the height of the mixed layer, whereas the heat flux shows a large spread.

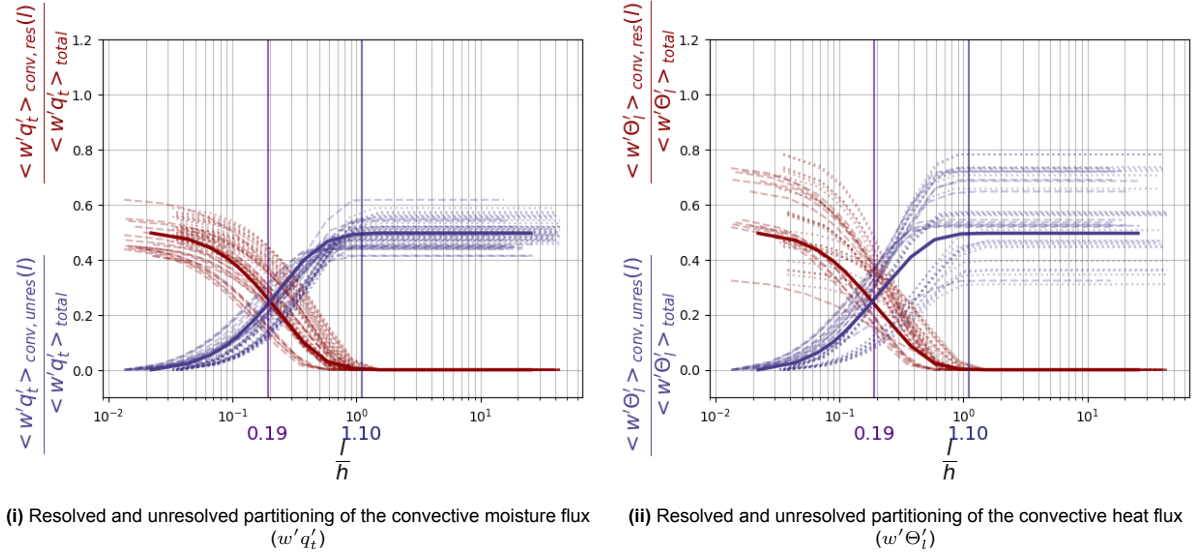


Figure 5.4: Partitioning function of the convective flux, selecting the updrafts where $w > w_{90\%}$. Taken at $0.25 \leq \frac{z}{h} \leq 0.75$, with $t \in t_{cloudy}$. With the hourly (patterned) and mean (solid) partitions of the resolved (red) and unresolved (purple) convective fluxes. The dotted lines show the BOMEX results, and the dashed lines show the Cabauw results.

In figure 5.5 the resolved and the unresolved partitioning of the convective flux to the total heat flux are depicted with a different color per location, separately for the BOMEX case and the Cabauw case. The spread of the convective partitioning correlates similarly to the location in the mixed layer, as it did for the total flux. Therefore, the change in sign of the heat flux, transported by convective updraft, is expected to be the reason of large spread in partitionings to the total heat flux in the mixed layer.

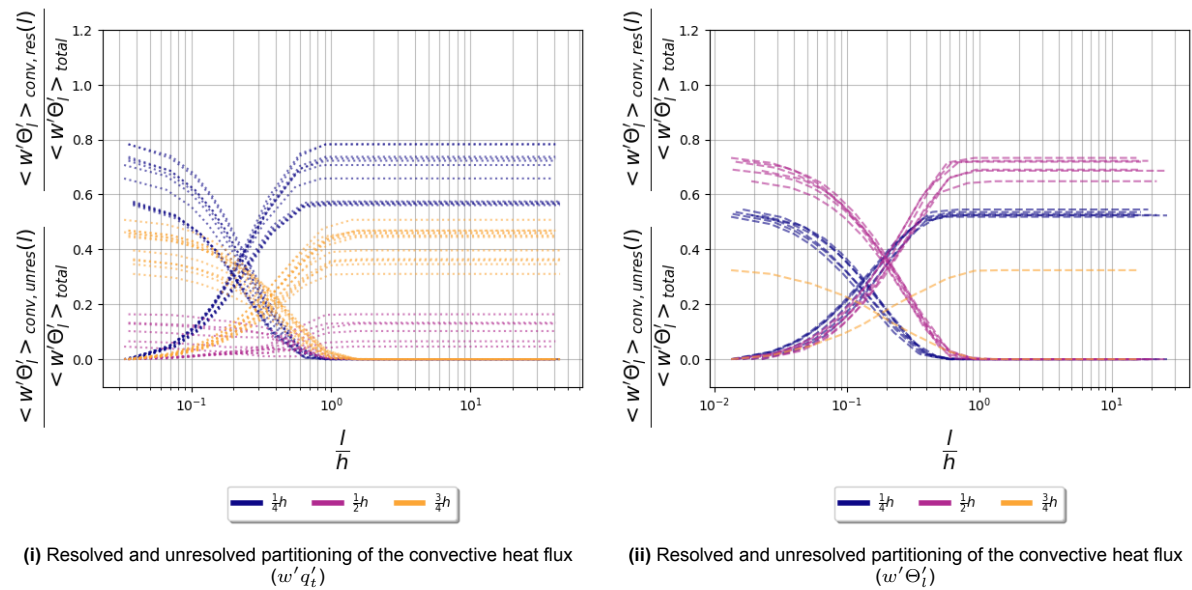


Figure 5.5: Hourly resolved and unresolved convective partitioning to the total heat flux of the BOMEX and the Cabauw at $0.25 \leq \frac{z}{h} \leq 0.75$, with $t \in t_{cloudy}$. The different locations ($\frac{1}{4}h$, $\frac{1}{2}h$, and $\frac{3}{4}h$) in the mixed are depicted with blue, purple and yellow, respectively.

From the convective resolved and the unresolved partitioning of the total moisture flux, it shows that these convective updrafts in the mixed layer contribute around 50% of the total flux, on average. Additionally, it shows that the structures carrying the total moisture flux in the mixed layer, become unresolved at a relative coarser grid, than the convective structures carrying the moisture flux. This indicates that the total moisture flux in the mixed layer is not solely carried on these stronger updrafts, but other larger structures contribute to the total flux as well.

Fluxes of momentum

In figure 5.6 the partitioning functions, found in the mixed layer, are shown for the momentum flux of the zonal wind (5.6ii) and the meridional wind (5.6i).

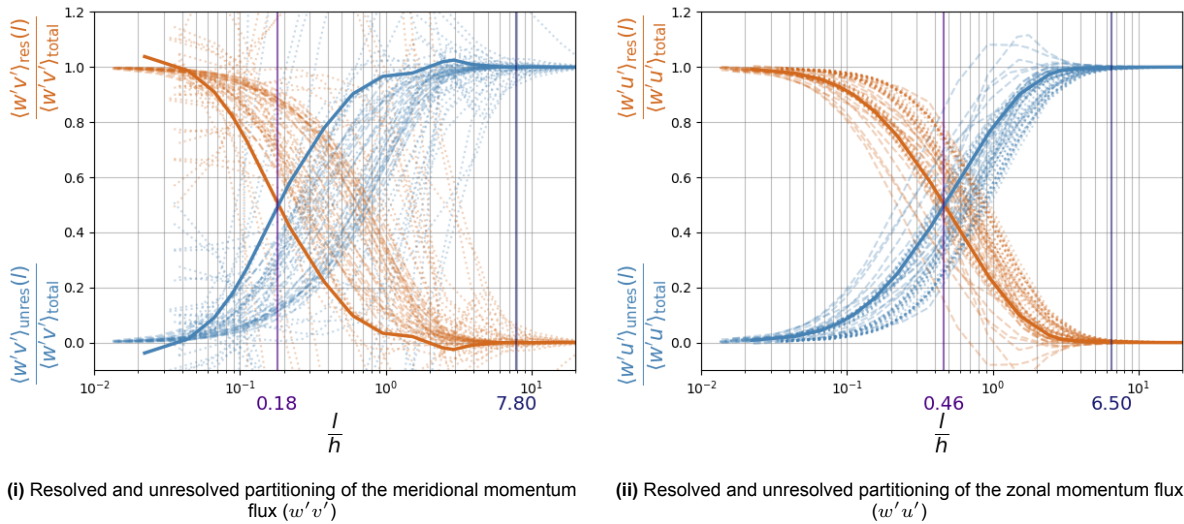


Figure 5.6: Partitioning functions, at $0.25 \leq \frac{z}{h} \leq 0.75$, with $t \in t_{cloudy}$.

With the hourly (patterned) and mean (solid) partitionings of the resolved (orange) and unresolved (blue) momentum fluxes. The dotted lines show the BOMEX results, and the dashed lines show the Cabauw results. The indicators I_{int} and I_{exc} are depicted in light and dark purple

The hourly partitionings of the total upward transport of both the meridional and the zonal momentum show to be very scattered, with a wide spread and even outlying highly positive and negative values. This shown most strongly for the meridional flux. These outliers can be associated with the BOMEX case, where the meridional wind (v) in the mixed layer is weak. This causes little shear in the meridional direction, hence the shear-driven turbulence of the meridional momentum flux is small. Due to these weak shear-driven stresses, larger scaled flows in the meridional direction can develop more freely. The total flux is determined by using the correlation between the fluctuations in the vertical wind w' and the meridional wind v' at LES-resolution. At such fine scales, these large scaled flows may not show yet, resulting in a weak correlation. However, while coarse-graining, the large-scaled correlations may start to show their contribution to the mean resolved flux. These larger flows may result in much strong negative or positive fluxes, differentiating with scale. This can cause the fraction of resolved and unresolved to the total flux to fluctuate strongly and even exceed the total flux computed at LES-resolution.

For the BOMEX case, the zonal momentum flux is more strongly contributed by shear-driven turbulence, given that the zonal wind is much stronger. For the Cabauw case, this is the same with meridional wind. The partitioning functions of these stronger momentum fluxes are depicted separately in figure 5.7. The momentum shows to be transported on structures that scale well with the height of the mixed layer, with sizes somewhat similar to those carrying moisture and heat. Especially the zonal momentum of the BOMEX case, where this wind is very strong. This may indicate that the momentum fluxes of the stronger winds are carried, or partly carried, on convective updrafts.

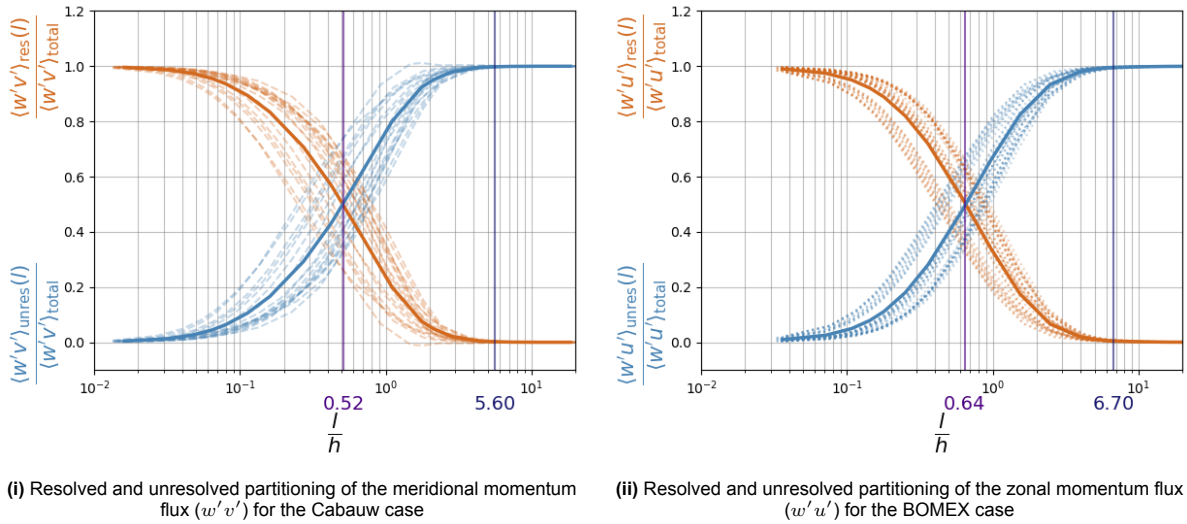


Figure 5.7: Partitioning functions, at $0.25 \leq \frac{z}{h} \leq 0.75$, with $t \in t_{cloudy}$.

With the hourly (patterned) and mean (solid) partitionings of the resolved (orange) and unresolved (blue) momentum fluxes. The dotted lines show the BOMEX results, and the dashed lines show the Cabauw results. The indicators I_{int} and I_{exc} are depicted in light and dark purple

Convective momentum flux

In figure 5.8, the partitionings of the convective flux to the total flux in the mixed layer are shown. They are shown for the momentum of the strong, dominant winds, e.g., the meridional momentum flux of the Cabauw case (5.7i) and the zonal momentum flux of the BOMEX case (5.8ii). These encourage the suggestion that these momentum fluxes are carried on convective structures. They show that the flux carried on these updrafts makes up for about 50% to 60% of the total turbulent transport of the momentum in the mixed layer, for both cases. This is similar to what was found for the moisture flux. Likewise, the partitionings of the convective flux show strong similarities to those of the total resolved flux in figure 5.7: both convective momentum fluxes scale well with height of the mixed layer, especially the zonal momentum flux of the BOMEX case. Similar to the moisture flux as well, the convective partitionings show faster decrease than the total partitioning, indicating additional transport on larger scales.

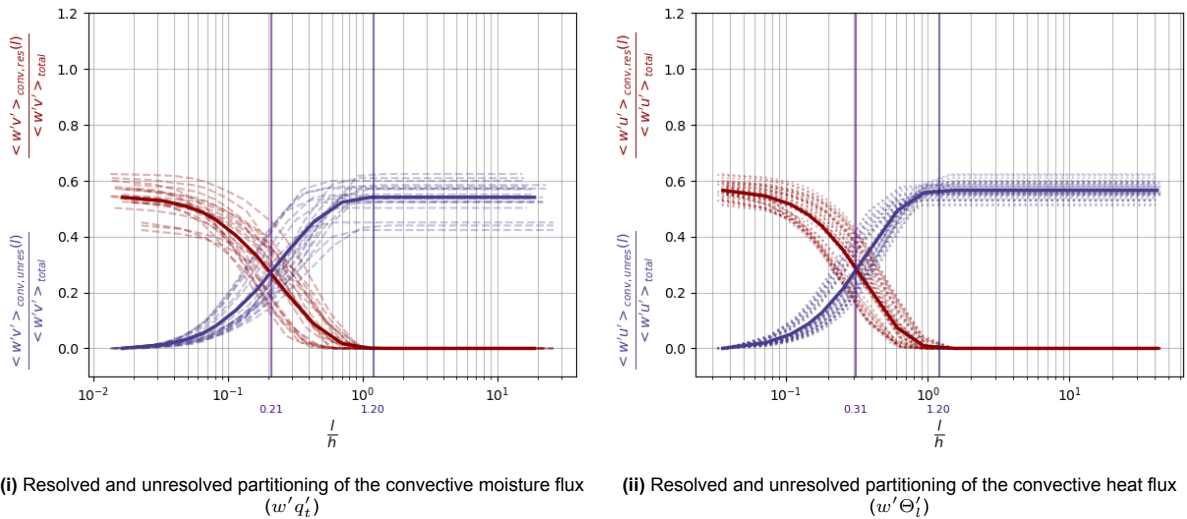


Figure 5.8: Partitioning function of the convective flux, selecting the updrafts where $w > w_{90\%}$. Taken at $0.25 \leq \frac{z_c}{h_c} \leq 0.75$, with $t \in t_{cloudy}$. With the hourly (patterned) and mean (solid) partitionings of the resolved (red) and unresolved (purple) convective fluxes. The dotted lines show the BOMEX results, and the dashed lines show the Cabauw results. The indicators I_{int} and I_{exc} are depicted in light and dark purple.

5.1.2. Cloud layer

In this section, the partitionings of the resolved and unresolved partitionings of the variances and fluxes are plotted against the grid-size, normalized with the height of the mixed layer ($h + h_c$).

Variances

In figure 5.9 the partitioning functions of the variance in the potential temperature, the specific humidity and the wind velocities are plotted against the dimensionless grid size, for the selected locations in the cloud layer. On average, the results show that the variance structures in specific humidity are comparatively larger than those in potential temperature, which are, in turn, larger than the variance structures in horizontal and vertical wind, with the latter exhibiting the smallest structures. Comparing the results obtained from the mixed layer shows a similar order of relative structure sizes for the various quantities. For these convective cases, the variance of the different quantities in the cloud layer is expected to be dominated by the convective motion, which may be even stronger due to condensation processes, especially for the conserved variables. Consequently, the scales of the variance structures are expected to scale well with the height of the cloud layer.

Similar to the mixed layer, the variance in the zonal and meridional winds in figure 5.9 show a relatively wider spread, as their variance is not so strongly dominated by convective transport. The variance of the moisture flux shows sufficient scaling, as the two cases overlap, but it shows a wider spread for the BOMEX case itself. The variance partitioning function of the variance in virtual temperature and vertical velocity show a spread that is relatively narrow when considered individually, but relatively wide when compared to each other. The variances that do not scale well, show the effects of normalizing the grid with the height of the mixed layer (h) or the cloud layer ($h + h_c$). As their heights of the cloud layer are pretty similar, the structures of variance in the Cabauw case show to be larger than those of the BOMEX case. However, the height of the mixed layer is much lower for the BOMEX case than for the Cabauw case, and thus appear relatively larger in the mixed layer.

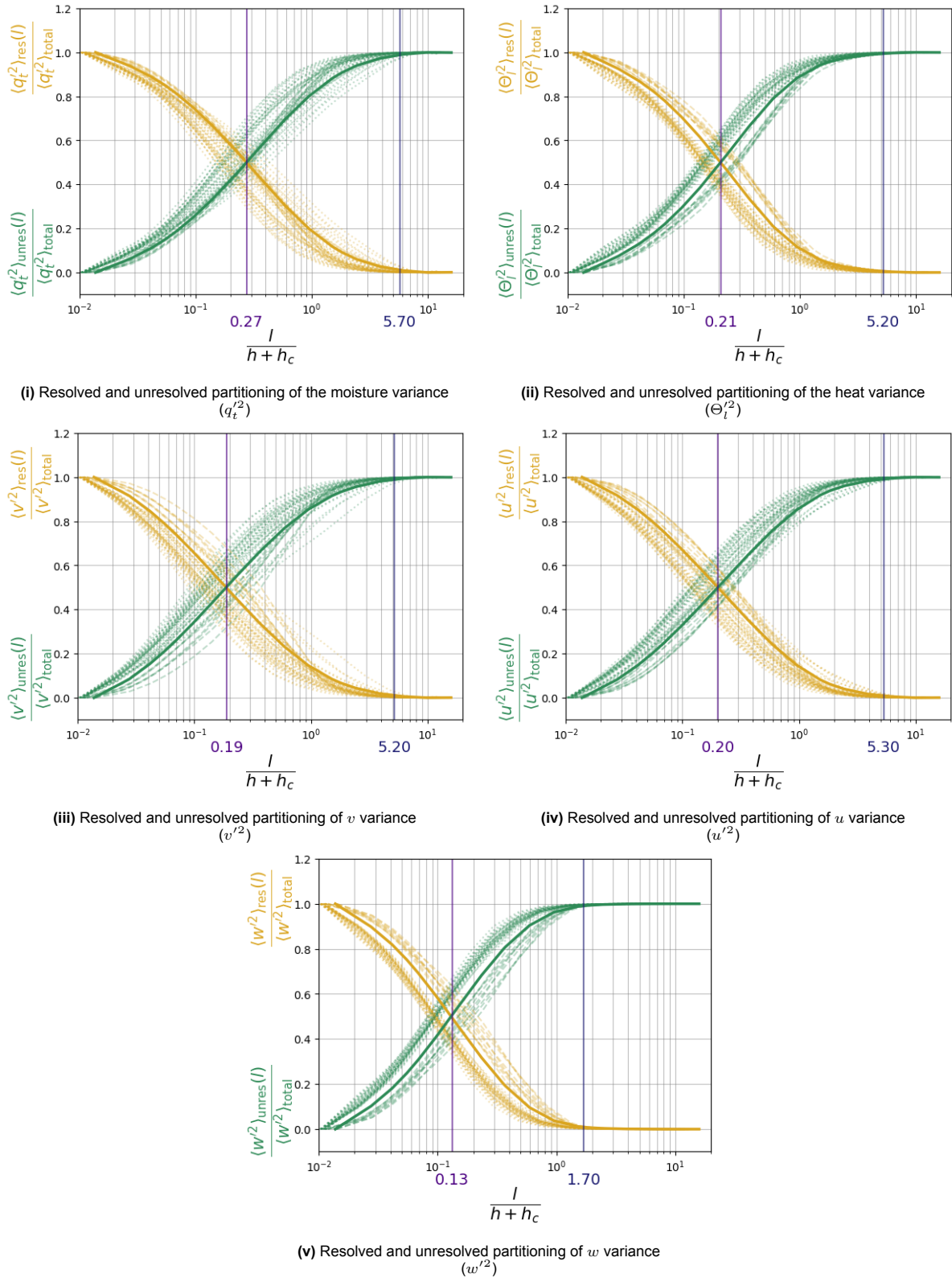


Figure 5.9: Partitioning functions variance, at $0.25 \leq \frac{z_c}{h_c} \leq 0.75$, with $t \in t_{cloudy}$.

With the hourly (patterned) and mean (solid) partitionings of the resolved (yellow) and unresolved (green) variance. The dotted lines show the BOMEX results, and the dashed lines show the Cabauw results. The indicators I_{int} and I_{exc} are depicted in light and dark purple

Fluxes of conserved variables

The partitioning functions of the heat and momentum flux are plotted against the grid spacing, normalized with the height of the cloud layer, in figure 5.10. The figures show similar partitioning functions for both fluxes, indicating that on average, these are vertically transported on scales of similar size in the cloud layer, which are expected to be dominated by convective structures. This is supported by the strong resemblance to the partitioning function of the variance in vertical velocity (5.9v). Looking back on the results in the mixed layer, this is much less the case. This suggests that moisture and heat flux are more strongly dominated by the variance in vertical velocity in the cloud layer than in the mixed layer. Both the moisture and heat flux scale very well with the height of the cloud layer for the BOMEX case, but show a larger spread for the Cabauw case.

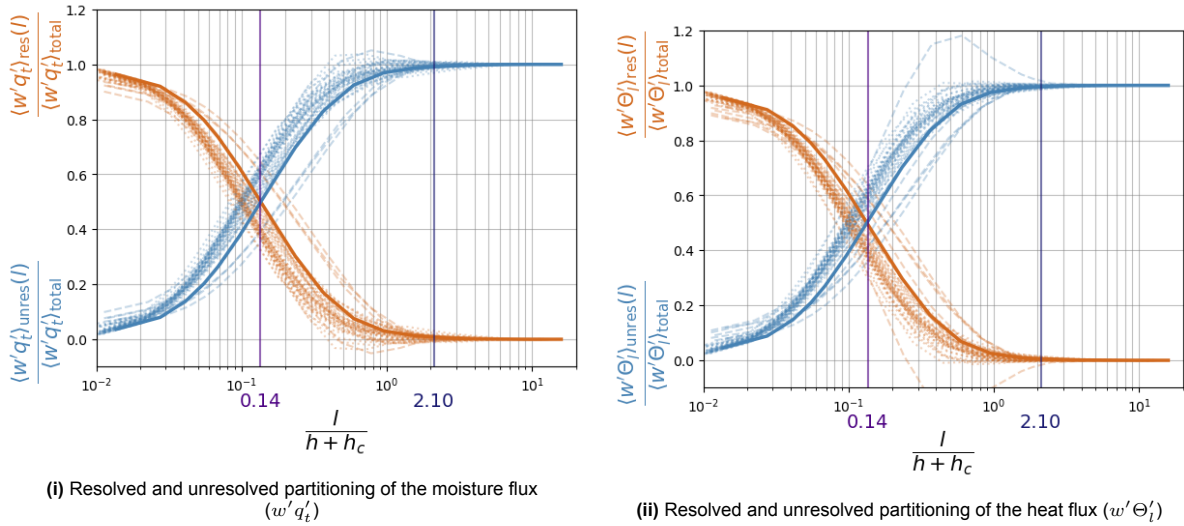


Figure 5.10: Partitioning functions, at $0.25 \leq \frac{z_c}{h_c} \leq 0.75$, with $t \in t_{cloudy}$. With the hourly (patterned) and mean (solid) partitionings of the resolved (orange) and unresolved (blue) fluxes. The dotted lines show the BOMEX results, and the dashed lines show the Cabauw results. The indicators I_{int} and I_{exc} are depicted in light and dark purple.

This spread is strongly correlated with the location taken in the cloud layer, shown in figure 5.11. The fluxes seem to become unresolved relatively faster at higher locations in the cloud, where the heat flux also shows outliers at larger grid scales. Cabauw is a weaker convective case, and the clouds maybe less steady over height as those of BOMEX. Giving smaller fluxes higher in the cloud, as they are starting to dissolve. With these weaker flux, larger-scaled flows may start to contribute more strongly to the total flux, showing their correlation between w' and thl' at lower resolutions. This similar to what is seen at the weak momentum flux of BOMEX (5.6).

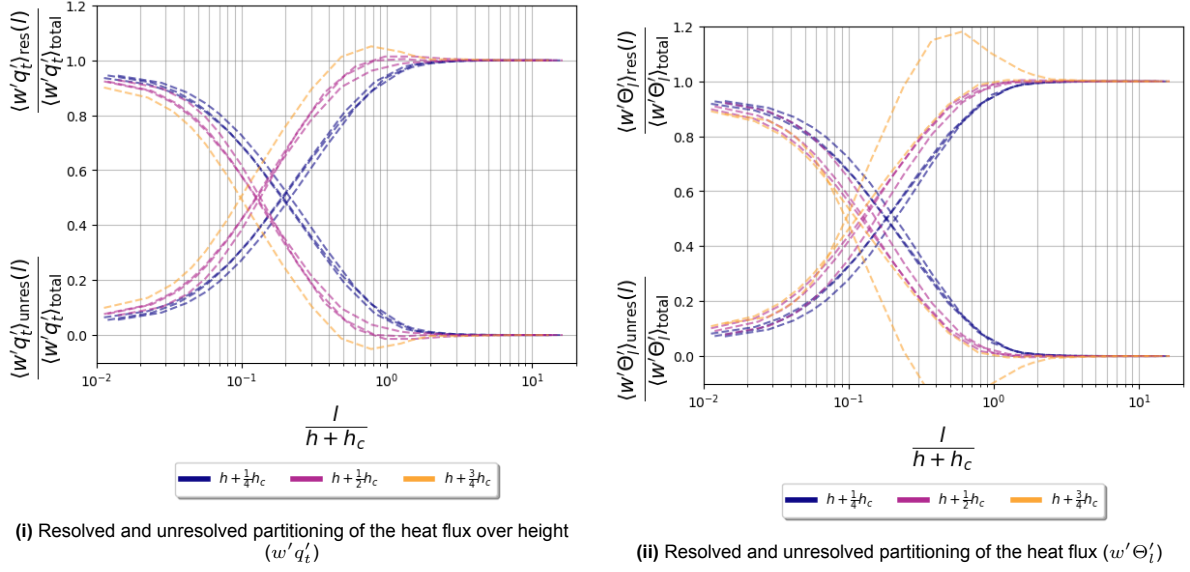


Figure 5.11: Hourly partitionings of the resolved and unresolved fluxes of the BOMEX and the Cabauw at $0.25 \leq \frac{z_c}{h_c} \leq 0.75$, with $t \in t_{cloudy}$. The dotted lines show the BOMEX results, and the dashed lines the Cabauw results. The different locations ($h + \frac{1}{4}h_c$, $h + \frac{1}{2}h_c$, and $h + \frac{3}{4}h_c$) in the mixed are depicted with blue, purple and yellow, respectively.

Convective fluxes of conserved variables

In figure 5.12, the partitionings of the convective flux to the total moisture and heat flux in the cloud layer are shown. Again, the BOMEX case scales well with cloud height, for both moisture and heat, similar to the partitioning of the total flux. Furthermore, the total transport appears to be almost completely driven by convective transport, and their partitionings show a strong similarity. This suggests that the convective transport is strongly dominant for both heat and moisture in this case. For both the BOMEX and the Cabauw case, some partitionings show a mean convective flux higher than the mean total flux, indicating strong negative environmental flux, which may be due to negative subsidence of dissolving clouds or strong flows at higher altitudes. For the Cabauw case, these values show to be more extreme, with an overall much larger spread for both the heat and moisture flux.

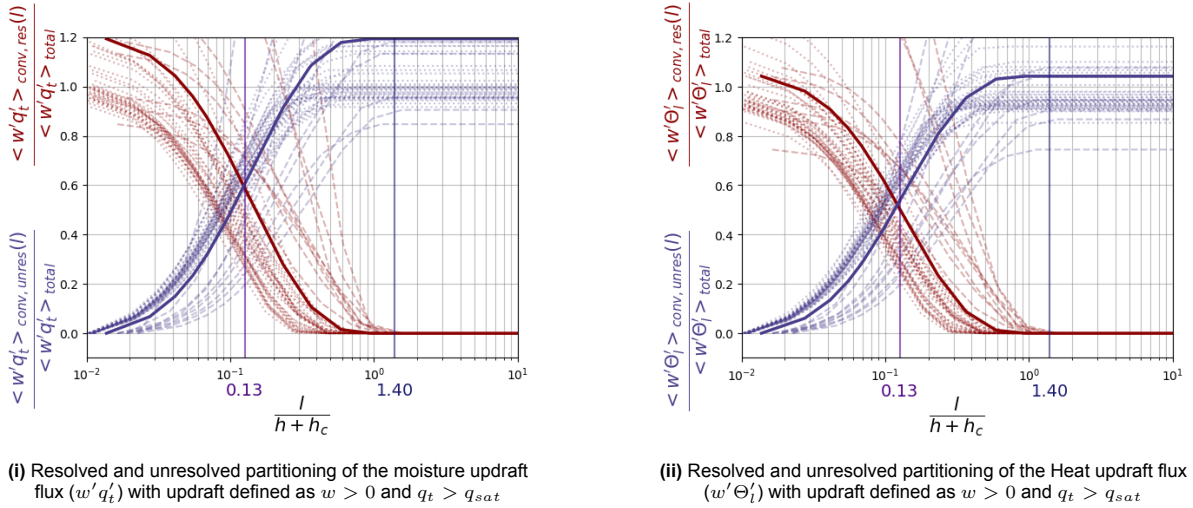
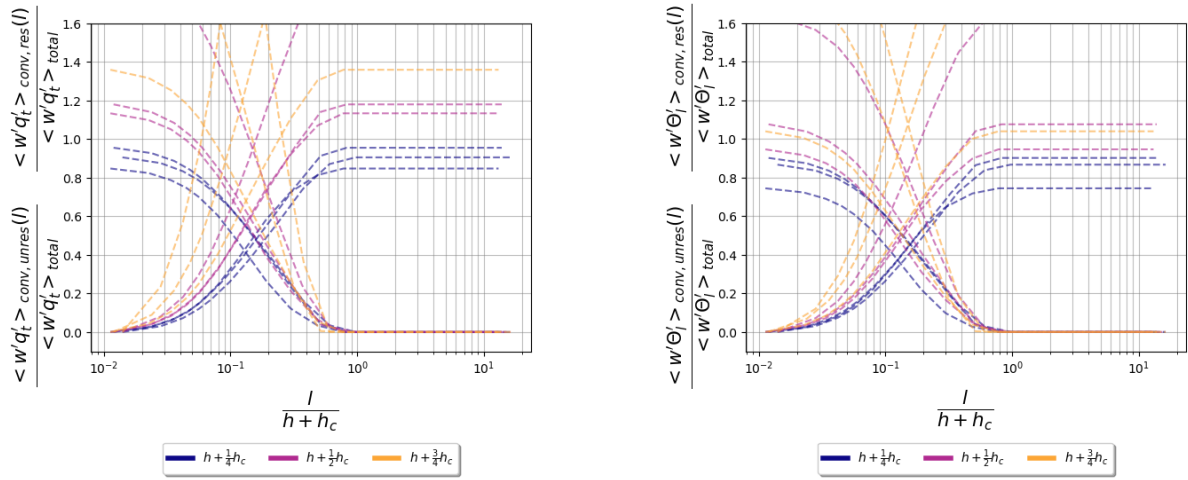


Figure 5.12: Partitioning function of the convective flux, selecting the updrafts where $w > 0$ and $q_t > q_{sat}$. Taken at $0.25 \leq \frac{z_c}{h_c} \leq 0.75$, with $t \in t_{cloudy}$. With the hourly (patterned) and mean (solid) partitionings of the resolved (red) and unresolved (purple) convective fluxes. The dotted lines show the BOMEX results, and the dashed lines show the Cabauw results. The indicators I_{int} and I_{exc} are depicted in light and dark purple.

These indeed are found to be at the higher locations in the cloud, shown in figure 5.13. The stronger effect of such negative fluxes on the Cabauw case, may be due to its weaker convective transport.



(i) Resolved and unresolved partitioning of the moisture updraft flux ($w'q'_t$) with updraft defined as $w > 0$ and $q_t > q_{sat}$

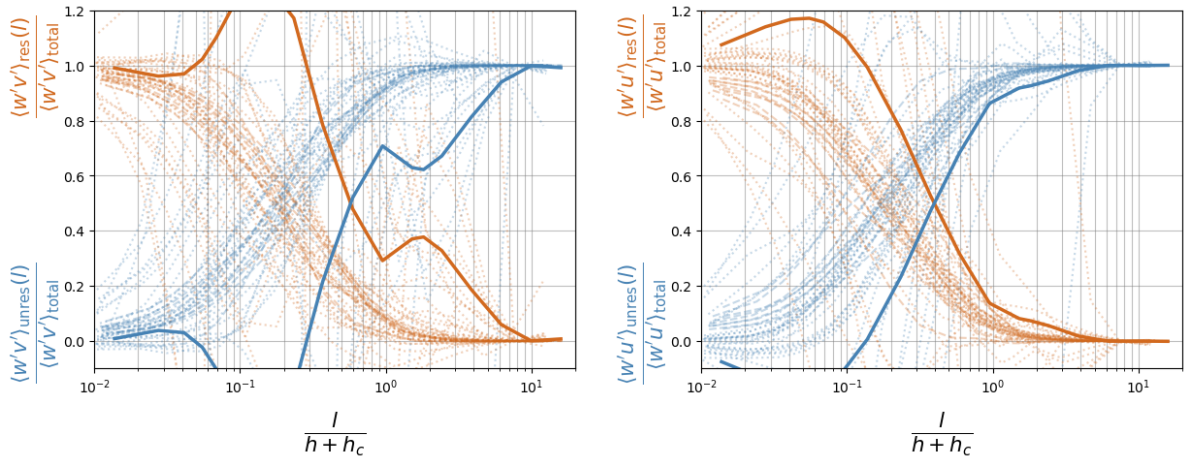
(ii) Resolved and unresolved partitioning of the Heat updraft flux ($w'\Theta'_t$) with updraft defined as $w > 0$ and $q_t > q_{sat}$

Figure 5.13: Hourly partitionings of the convective resolved and unresolved fluxes of the BOMEX and the Cabauw at $0.25 \leq \frac{z_c}{h_c} \leq 0.75$, with $t \in t_{cloudy}$. The dotted lines show the BOMEX results, and the dashed lines the Cabauw results. The different locations ($h + \frac{1}{4}h_c$, $h + \frac{1}{2}h_c$, and $h + \frac{3}{4}h_c$) in the mixed are depicted with blue, purple and yellow, respectively.

Fluxes of momentum

The hourly partitionings of both the zonal and meridional momentum flux in the cloud layer shows a very wide spread and high positive and negative outliers, especially for the weaker winds. This is similar to what was observed in the mixed layer, indicating that the momentum flux of these weaker winds is carried less consistently by structures of a certain size. In the cloud layer, these momentum fluxes are thus driven by flows that are not strongly correlated with updrafts or downdrafts, such as moisture and heat, but by larger-scaled flows that show their correlation at higher grid scales.

Momentum fluxes of stronger winds, such the meridional and zonal momentum of the Cabauw case, shown in figure 5.15, show to scale better with the height of the cloud layer, especially the stronger zonal momentum. This indicates that they are more strongly carried on structures that correlate with the height of the cloud layer.

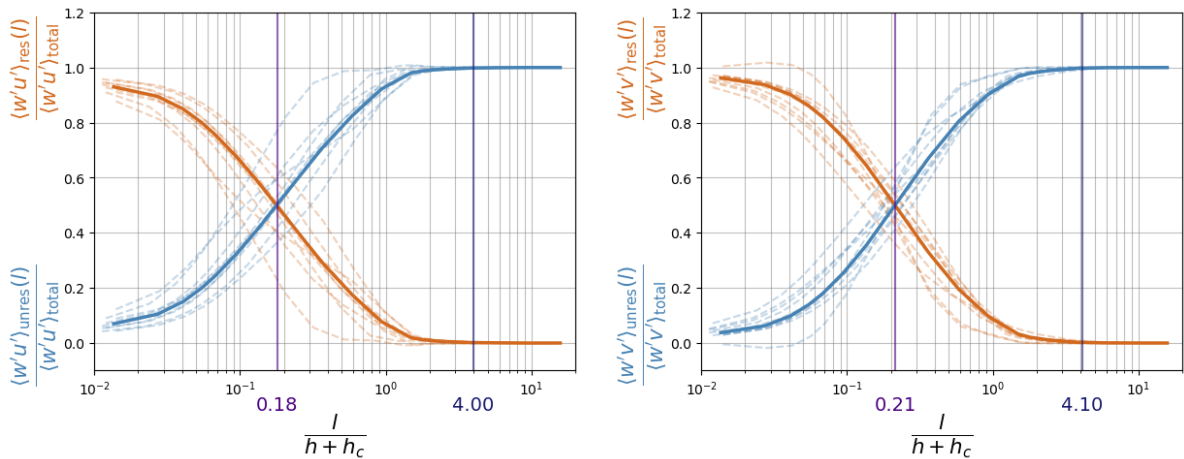


(i) Resolved and unresolved partitioning of the momentum flux ($w'v'$)

(ii) Resolved and unresolved partitioning of the momentum flux ($w'u'$)

Figure 5.14: Partitioning functions, at $0.25 \leq \frac{z_c}{h_c} \leq 0.75$, with $t \in t_{cloudy}$.

With the hourly (patterned) and mean (solid) partitionings of the resolved (orange) and unresolved (blue) momentum fluxes. The dotted lines show the BOMEX results, and the dashed lines show the Cabauw results. The indicators I_{int} and I_{exc} are depicted in light and dark purple



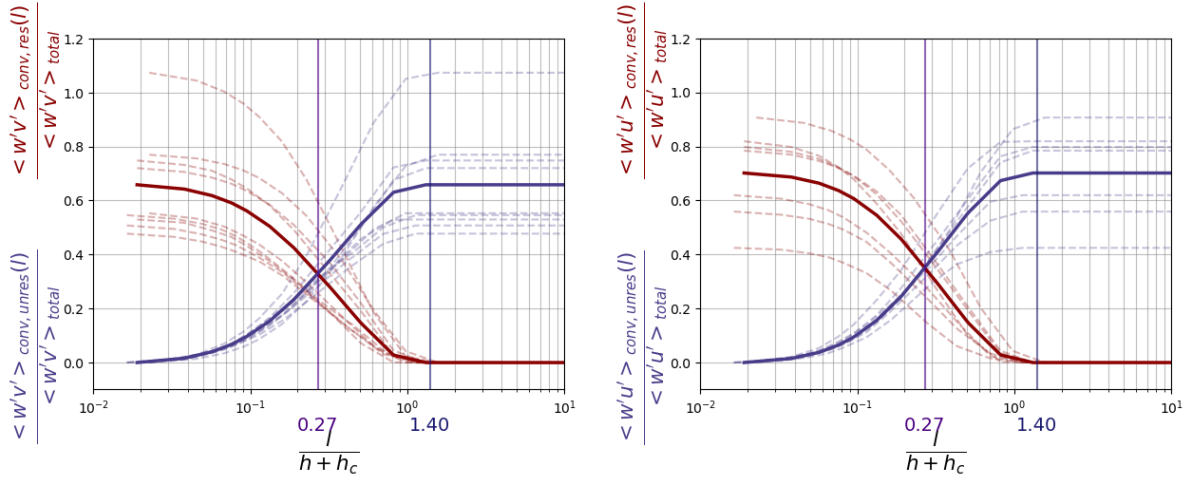
(i) Resolved and unresolved partitioning of the momentum flux ($w'v'$)

(ii) Resolved and unresolved partitioning of the momentum flux ($w'u'$)

Figure 5.15: Partitioning functions, at $0.25 \leq \frac{z_c}{h_c} \leq 0.75$, with $t \in t_{cloudy}$.

With the hourly (patterned) and mean (solid) partitionings of the resolved (orange) and unresolved (blue) momentum fluxes. The dotted lines show the BOMEX results, and the dashed lines show the Cabauw results. The indicators I_{int} and I_{exc} are depicted in light and dark purple

The convective partitioning to these momentum fluxes, shown in figure 5.16, similarly shows better scaling for the stronger wind, but both with a large spread. This may be explained by a less strong correlation between the momentum and the vertical velocity, where the updrafts may transport both negative and positive flux of momentum. Additionally, comparing these to the partitioning of the convective flux of the moisture and heat, the momentum seems to be effected less by the flows higher in the cloud.



(i) Resolved and unresolved partitioning of the convective momentum flux

(ii) Resolved and unresolved partitioning of the momentum heat flux

Figure 5.16: Partitioning function of the convective momentum flux, selecting the updrafts where $w > 0$ and $q_t > q_{sat}$. Taken at $0.25 \leq \frac{z_c}{h_c} \leq 0.75$, with $t \in t_{cloudy}$.

With the hourly (patterned) and mean (solid) partitionings of the resolved (red) and unresolved (purple) convective fluxes. The dotted lines show the BOMEX results, and the dashed lines show the Cabauw results. The indicators I_{int} and I_{exc} are depicted in light and dark purple.

Cross-sections

For both cases, multiple cross-sections, both in the vertical and horizontal domain, were taken, to study the structures of the discussed fluxes. Figure 5.17 shows such vertical cross-sections of the fluxes of the conserved variables and the momentum, taken from both the BOMEX and the Cabauw case. These are both selected at times and locations where cloud formation is clearly visible. The limits of each flux are set at scaled-down values of their true maximum and minimum, in a similar way, to focus on the structures and signs of the fluxes. The grids selected as updrafts are contoured with a black line, both in the mixed layer and in the cloud layer. The height of the mixed layer (h) and the height of the cloud layer ($h + h_c$) are indicated with the black dotted lines, and the locations in these layer ($\frac{1}{4}h, \frac{1}{2}h, \frac{3}{4}h, h + \frac{1}{4}h_c, h + \frac{1}{2}h_c, h + \frac{3}{4}h_c$) are indicated with the grey dotted lines.

Both cases show turbulent transport of moisture, heat, and momentum with both convective updrafts, and environmental turbulence. Some of these convective updrafts show to be the roots of the clouds, and grow stronger and more dominant in the cloud layer. Both in the mixed layer and in the cloud layer, the height of the updraft appear to be well represented by the height of the mixed layer and the height of the cloud layer. These figures also show, that with similar values of $h + h_c$, the depth of the clouds can vary significantly.

From the partitionings in the mixed layer, the resolved and unresolved partitioning to the total moisture flux showed to scale well with the height of the mixed layer, for both cases. However, the difference between the total and convective partitionings indicated that these selected updrafts were not strongly dominant for the total moisture and that other scales were effective. The strong, positive moisture flux in cross-section 5.17i and 5.17ii, indeed seem to be carried on the these updrafts, containing the highest vertical velocities. Additionally, some strong fluxes show to be carried on structures that do not contain these highest velocities.

In the same mixed layer, the resolved and unresolved partitioning to the total heat flux showed an unexpectedly large spread, which appeared to originate from higher levels in the mixed layer. The decomposition of the convective partition to the total flux showed similar results, indicating that this spread is located in these updrafts. As was theorized, the heat flux of both the BOMEX (5.17iii) and the Cabauw case (5.19iv) show strong negative fluxes near the LCL, located in the convective updrafts. With the lower height of the mixed layer of the BOMEX case, these negative fluxes penetrate deep into the mixed layer, effecting the total flux at both halfway and three third ($\frac{1}{2}h, \frac{3}{4}h$). Whereas these only significantly affect the total flux at the highest location ($\frac{3}{4}h$) of the Cabauw case. This is in agreement with what was seen in the partitioning functions (5.5).

From the partitioning functions of the momentum fluxes and the convective decomposition in the mixed layer, the fluxes of the strong winds appeared to be carried with the updrafts. However, they also indicated the presences of other structures carrying the momentum flux, that do not contain these highest velocities. The momentum flux of weaker winds showed very little correlation with the fluctuations in vertical velocity. And indeed, the momentum flux of the strong winds, e.g., the meridional wind of the Cabauw case and the zonal wind of the BOMEX case, show pretty strong correlation of the positive fluxes being carried on the strong updrafts. This is not as strong as the convective transport of the moisture, but still significant. Additionally, large structures show that contribute transport of strong fluxes as well, which do not contain the highest velocities.

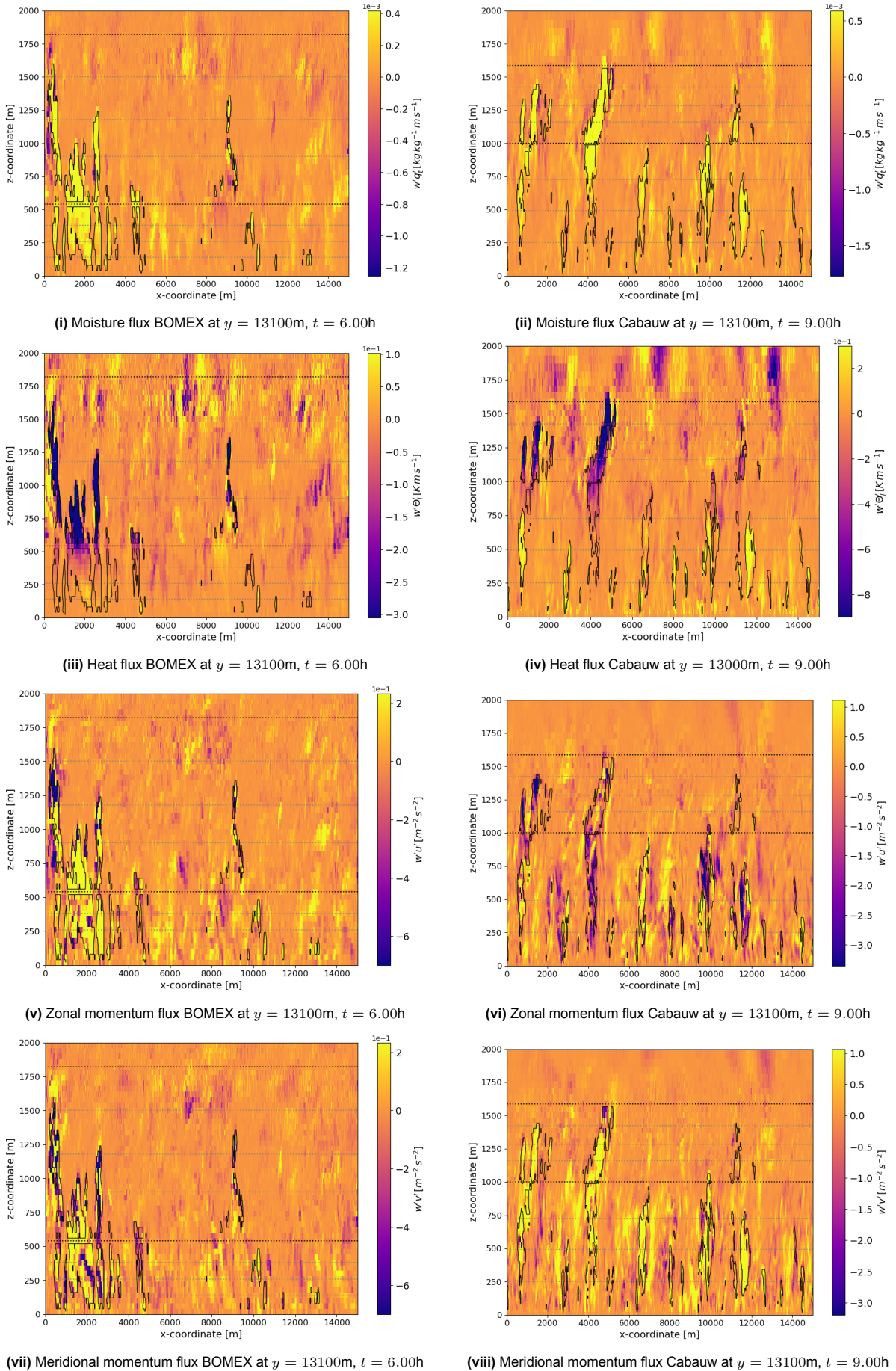


Figure 5.17: Vertical Cross-section of the moisture flux ($w'q'_t$), heat flux ($w'\theta'_t$), and momentum fluxes ($w'u'$, $w'v'$) of the Cabauw and BOMEX case. The black dotted lines indicate the height of the mixed layer (h) and the height of the cloud layer ($h + h_c$), and the grey dotted lines indicate the selected locations in these layers ($\frac{1}{4}h$, $\frac{1}{2}h$, $\frac{3}{4}h$, $h + \frac{1}{4}h_c$, $h + \frac{1}{2}h_c$, $h + \frac{3}{4}h_c$). The selected updrafts are outlined in black.

From the partitioning functions in the cloud layer, both the moisture and heat flux seemed strongly dominated by the convective transport in the updrafts, and scale very well with the height of the cloud layer ($h + h_c$). Whereas the Cabauw case showed much more spread, with strong outliers found at the highest locations in the cloud. These outliers were thought to originate in subsidence of clouds, or strong negative contribution to the total flux from flows at the cloud top. Looking at the cross-sections of the moisture and heat flux of the two cases, actually both cases show strong, fluctuating fluxes at the cloud top, but appear larger for the Cabauw case. This most strongly visible for the heat flux. The total fluxes of BOMEX case may be less affected by such flows, as its convective fluxes are very strong. Additionally, the more shallow cloud layer of the Cabauw case results in a relatively deeper penetration of these fluxes into the cloud layer, effecting more of the selected locations.

The momentum fluxes show much less correlation with the updrafts in the clouds. Even though most of the strong momentum fluxes are dominantly carried by these updrafts, they transport both strong negative and strong positive momentum fluxes. Only the zonal momentum of the Cabauw case appears to be significantly carried on these updrafts. The flows higher in the clouds, that strongly affected the moisture and heat flux, do not show to affect the momentum flux in a similar way. These findings are all in agreement with the behavior of the partitionings functions of the momentum flux in the cloud layer.

The horizontal cross-sections are shown both halfway the mixed layer ($\frac{z}{h} = \frac{1}{2}$) and halfway the cloud layer ($\frac{z_c}{h_c} = \frac{1}{2}$), taken at the same time as for the vertical cross-sections. These further confirm these findings. In the mixed layer, the updrafts show to strongly transport moisture in both cases. The negative flux in the updrafts carrying the heat flux already shows halfway in the mixed layer for the BOMEX case, whereas it's still positive here for the Cabauw case. And both moisture and heat show transport on structures that do not contain the highest velocities, but are similar in size or even larger. The positive momentum of the stronger velocities shows to be correlated with the updrafts for both cases, whereas those of the weaker wind show much less correlation. Additionally, these structures that do not contain the highest velocities but contribute significantly to the flux show even stronger in the transport of momentum.

In the cloud layer, the convective updrafts show to be strongly concentrated, especially in the BOMEX case. For this case, it shows the strong moisture and heat flux, concentrated in the updrafts, being very dominant. The Cabauw case also shows such strong updrafts, but also show the large flows outside these updrafts contributing to the total flux. The positive momentum flux of the most strong wind (5.19viii), shows to be carried on the updrafts, but the other momentum fluxes show not such a strong correlation as both positive and negative fluxes are carried upwards.

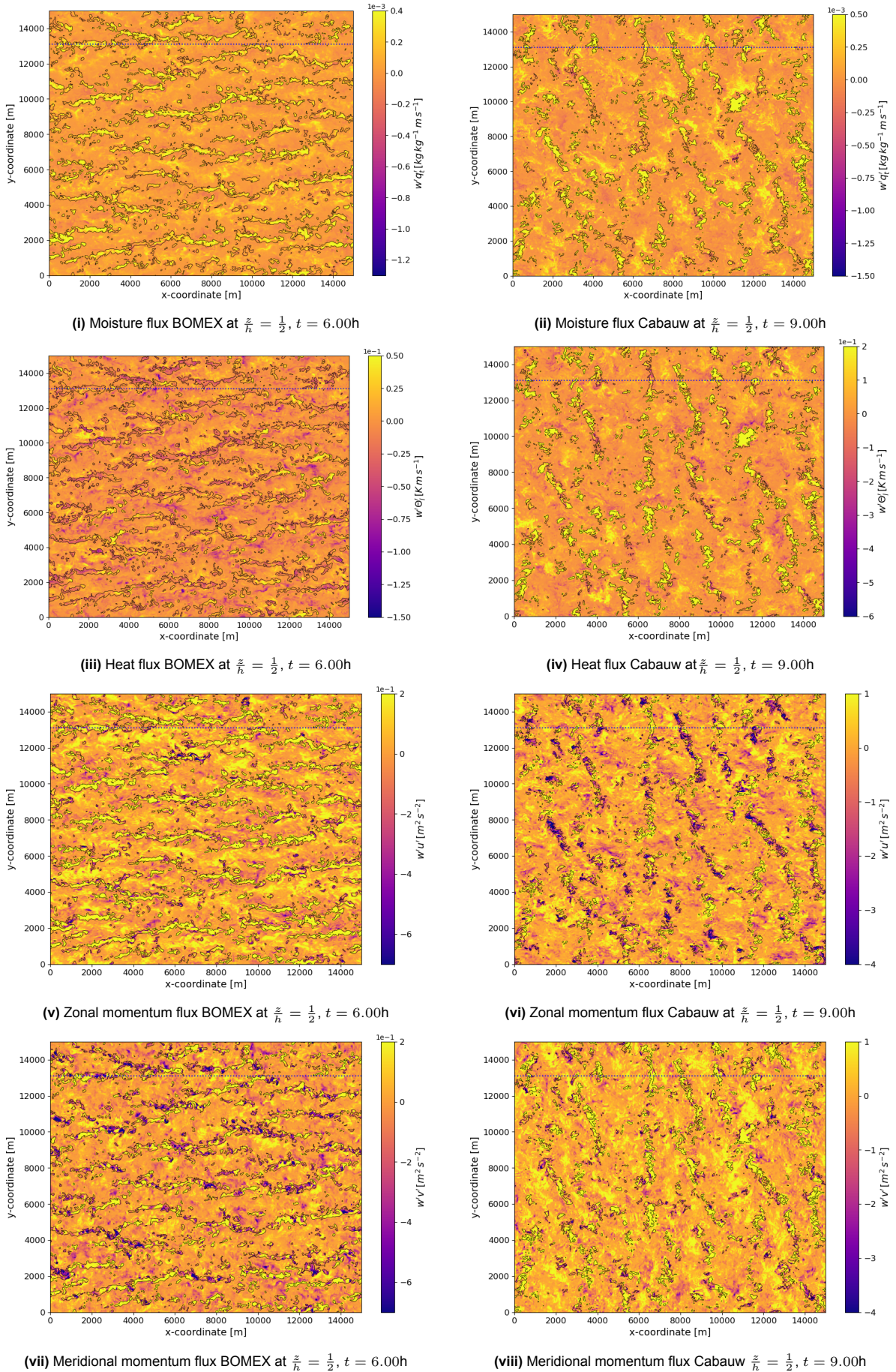


Figure 5.18: Horizontal cross-section of the moisture flux ($w'q'_t$), heat flux ($w'\Theta'_t$), and momentum fluxes ($w'u'_t$, $w'v'_t$) of the Cabauw and BOMEX case at $\frac{z}{h} = \frac{1}{2}$. The blue dotted lines indicates the y -coordinate of the taken vertical cross-section. The selected updrafts are outlined in black.

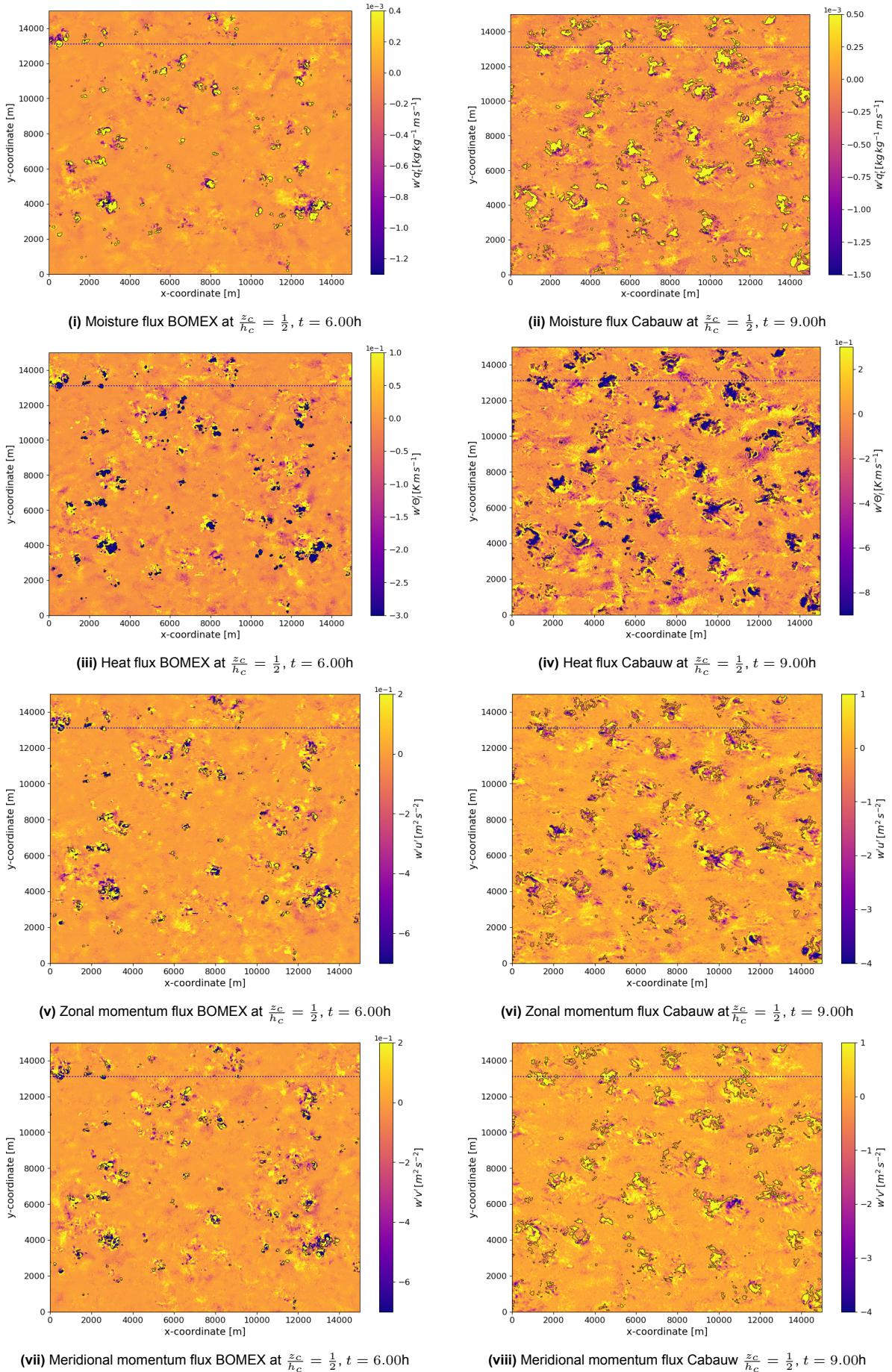


Figure 5.19: Horizontal cross-section of the moisture flux ($w'q'_t$), heat flux ($w'\theta'_t$), and momentum fluxes ($w'u'$, $w'v'$) of the Cabauw and BOMEX case at $\frac{z_c}{h_c} = \frac{1}{2}$. The blue dotted lines indicates the y -coordinate of the taken vertical cross-section. The selected updrafts are outlined in black.

5.2. HARMONIE runs

From the previous chapter, the moisture flux showed to most strongly correlate with the convective up-drafts. To evaluate the performance of the mass-flux in the EDMF-scheme of the HARMONIE model, the moisture flux is taken as a proxy.

In figure 5.20, the mean vertical profiles of the moisture flux, taken over the selected cloudy times, are shown for both the HARMONIE and LES runs in the same figures. The first figure shows the HARMONIE run at 500m resolution without any adaptations in the EDMF-scheme, the second figure shows the same HARMONIE run with the scale-adaptive MF-scheme and the third figures shows this HARMONIE run with the scale-adaptive scheme and the vertical velocity threshold w_{max} . Without any adaptations, the average profile of the moisture flux from the HARMONIE run seems quite similar to the LES run, with the same order of magnitude both in the mixed and in the cloud layer. However, the flux appears to decrease already at a lower altitude than that of the HARMONIE run, but not a fast. On average, the height of the dry updraft reaches higher than the LCL from the LES run, resulting in a higher value for h . The moist updraft also reaches higher than the highest level of liquid water from the LES run, resulting in a higher value of h_c . It is important to note that the HARMONIE turbulence scheme is initialized with a surface scheme, which has a strong influence on the strength of the fluxes.

As the scale-aware MF-scheme is implemented, a somewhat stronger flux is found at lower altitudes in the mixed layer, which inverse slightly more strongly, resulting in a lower flux near cloud base. With the additional vertical velocity threshold, both these effects show even stronger, magnifying the flux at lower altitude and decreasing it more strongly at higher altitudes.

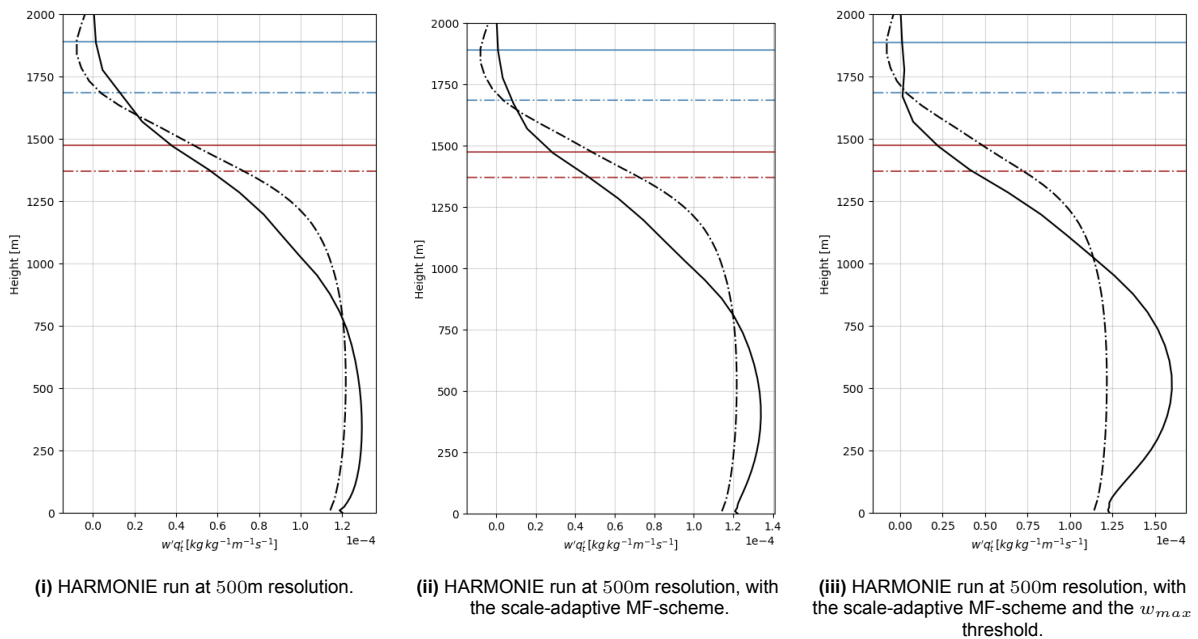


Figure 5.20: Mean vertical profiles of the moisture flux of the Cabauw case, taken over $t \in t_{cloudy}$, from the HARMONIE run at 500m resolution (solid) and the LES run (dashed). With the height of the mixed layer (h) shown in red, and the height of the cloud layer ($h + h_c$) shown in blue.

In figure 5.21, these vertical profiles of the moisture flux from the HARMONIE run are shown, with the resolved and subgrid fluxes depicted separately. The black and the green solid line indicate the total and the resolved flux, respectively. The subgrid fluxes are patterned, with the dashed lines indicating the dry (brown) and moist (blue) MF-transport and the dotted grey line indicating the ED-transport.

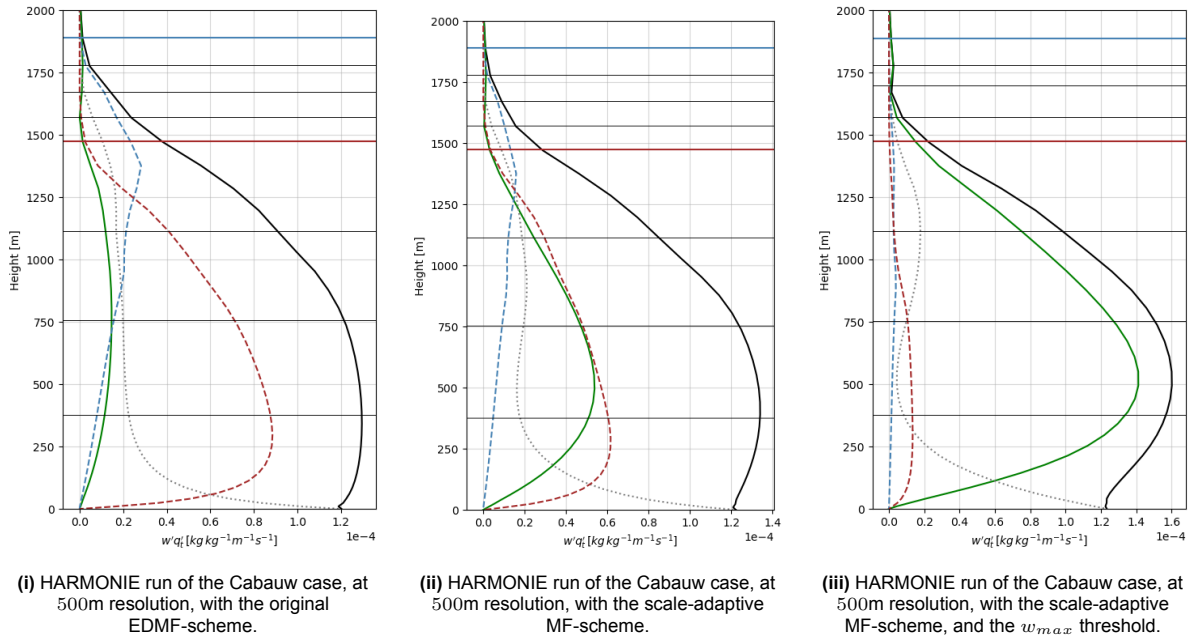


Figure 5.21: Mean vertical profiles of the moisture flux of the HARMONIE runs, taken over $t \in t_{cloudy}$. The black solid line indicates the total flux, the green solid line indicates the total resolved flux. The subgrid fluxes are patterned, with the dashed lines indicating the dry (brown) and moist (blue) MF-transport and the dotted grey line indicating the ED-transport. With the height of the mixed layer (h) shown in red, and the height of the cloud layer ($h + h_c$) shown in blue.

In the mixed layer, scaling down the dry mass-flux with the height of the mixed layer (h), shows to significantly decrease its partitioning to the total moisture flux. This results in a significantly higher partitioning of resolved moisture flux, with a higher total flux at these lower altitudes. An additional use of the vertical velocity threshold w_{max} , ensures the MF-scheme to be turned off at grids where the absolute velocity exceeds 0.1m/s (below 7km). This results in an additional strong decrease of the partitioning of the dry mass-flux to the total moisture flux. The resolved flux is now dominant to the total flux in the mixed layer, increasing it even more.

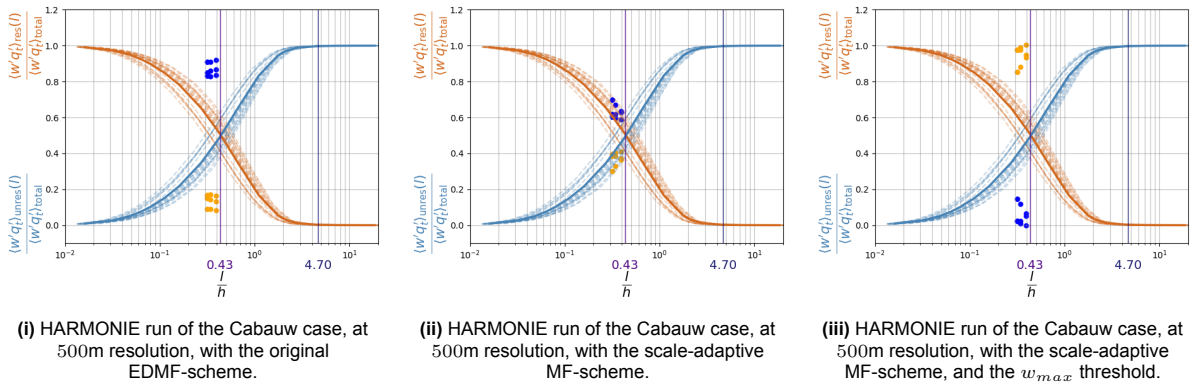


Figure 5.22: The hourly partitions of the resolved (orange markers) and unresolved (blue markers), for the locations in the mixed layer ($\frac{1}{4}h$, $\frac{1}{2}h$ and $\frac{3}{4}h$), plotted on the LES-based partitioning functions of the moisture flux in the mixed layer for the Cabauw case.

In figures 5.22, the LES-based partitioning functions of the moisture flux in the mixed layer of the Cabauw case from the previous chapter are shown, with the hourly resolved and unresolved partition to the total flux in the mixed layer from the HARMONIE runs marked. Scaling the MF-scheme with the height of the mixed layer, the partitioning of the subgrid flux shows to be higher than expected from the LES results, and subsequently the resolved partitioning show to be lower than expected. This may suggest that in the mixed layer, the down-scaling of the dry MF with the height of the mixed layer (h) is not strong enough for this case. Another explanation could be the ED-scheme, as this is not adapted

to the Grey zone resolution. This may be too strong, resulting in a too high partitioning of the subgrid turbulence to the total. Adding the vertical velocity threshold, the resolved partitioning now shows to be larger than expected, and the unresolved partitioning subsequently lower. This indicates that this threshold of vertical velocity is set too low, shutting down the dry mass-flux too early.

Looking at these HARMONIE profiles of the moisture flux in the cloud layer, the resulting partitionings of the resolved and unresolved flux to its total, is compromised at higher locations in the cloud. From approximately 1600m till the top of the cloud, the resolved moisture flux appears stronger than lower in the cloud, and is not affected by decrease in mass-flux parametrization. As discussed in chapter 4.1, the LES runs are imposed with the dynamical tendencies from the HARMONIE model. Looking back on the cross-sections of the LES runs (5.17ii), it showed such strong dynamics at these heights, positively contributing to the moisture flux. These strong fluxes therefore interfere with the results as they are seen as 'resolved' fluxes and give unrepresentative higher values to resolved partitionings, at these locations. This shows more clearly when the vertical profiles of these resolved partitionings to the total flux are plotted against the height, shown in figure 5.23.

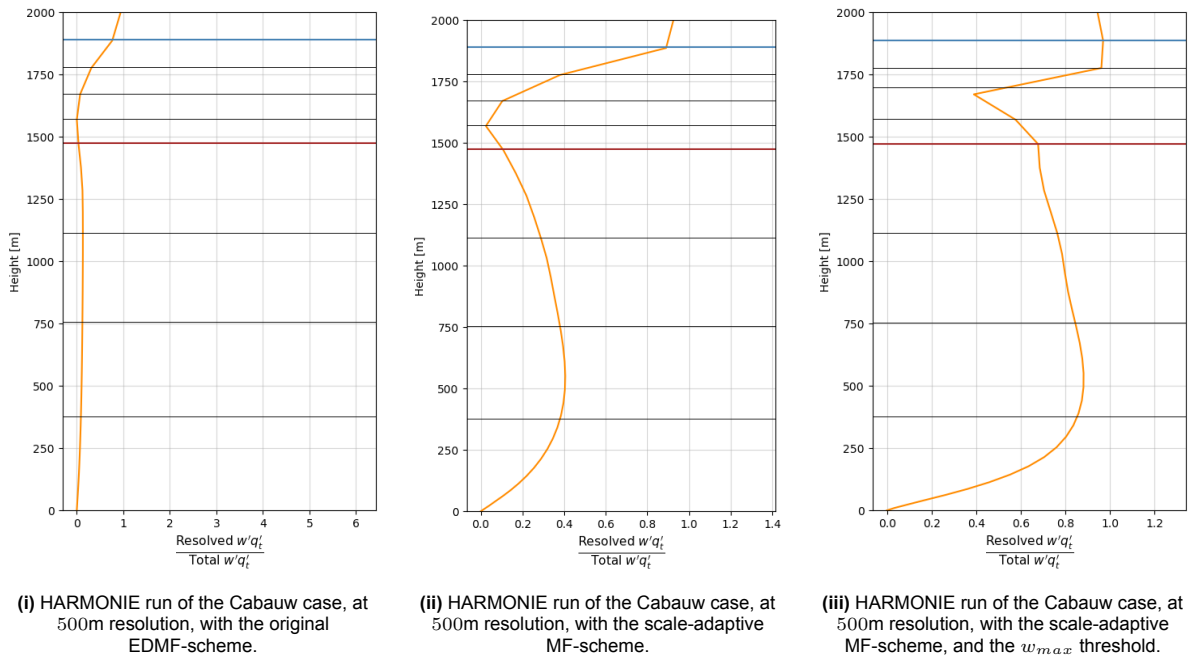


Figure 5.23: Mean vertical profiles of the resolved partitioning to the total moisture flux of the HARMONIE runs of the Cabauw case, taken over $t \in t_{cloudy}$. With the height of the mixed layer (h) shown in red, and the height of the cloud layer ($h + h_c$) shown in blue.

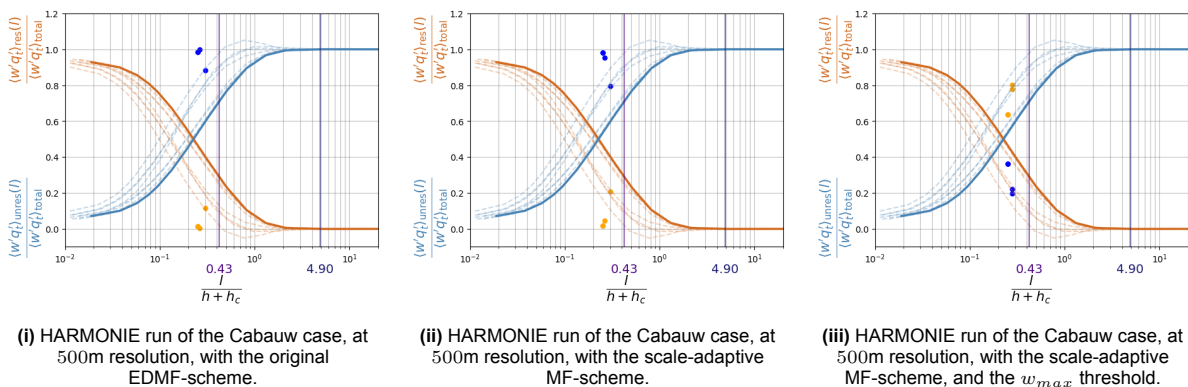


Figure 5.24: The hourly partitions of the resolved (orange markers) and unresolved (blue markers), for the locations in the mixed layer ($h + \frac{1}{4}h_c$, $h + \frac{1}{2}h_c$ and $h + \frac{3}{4}h_c$), plotted on the LES-based partitioning functions of the moisture flux in the cloud layer for the Cabauw case.

Therefore, in figure 5.24, only the HARMONIE partitionings are shown for the lowest height in the cloud layer ($h + \frac{1}{4}h_c$), in the LES-based partitioning functions of the moisture flux in the cloud layer. These show, that at these heights, scaling down the moist mass-flux with the height of the cloud layer results in very similar partitionings to the total flux as without this down-scaling. Looking at the mean vertical profiles of the moisture flux in the HARMONIE runs 5.21, it shows that this down-scaling does decrease the moist mass-flux, however, this does not show in a similar strong increase in resolved flux. This results in a lower total flux, leaving the resulting partitionings to be very similar. This indicates that the height of the cloud layer may be a too strong indicator of the convective nature of the clouds, in this case. An additional use of the vertical velocity threshold w_{max} , results in an almost zero moist mass-flux. With this, the total flux is almost completely defined by the resolved flux, resulting in a too high partitioning of the resolved flux, and an even lower total flux. Again, this suggests that the threshold of the vertical velocity is set too low.

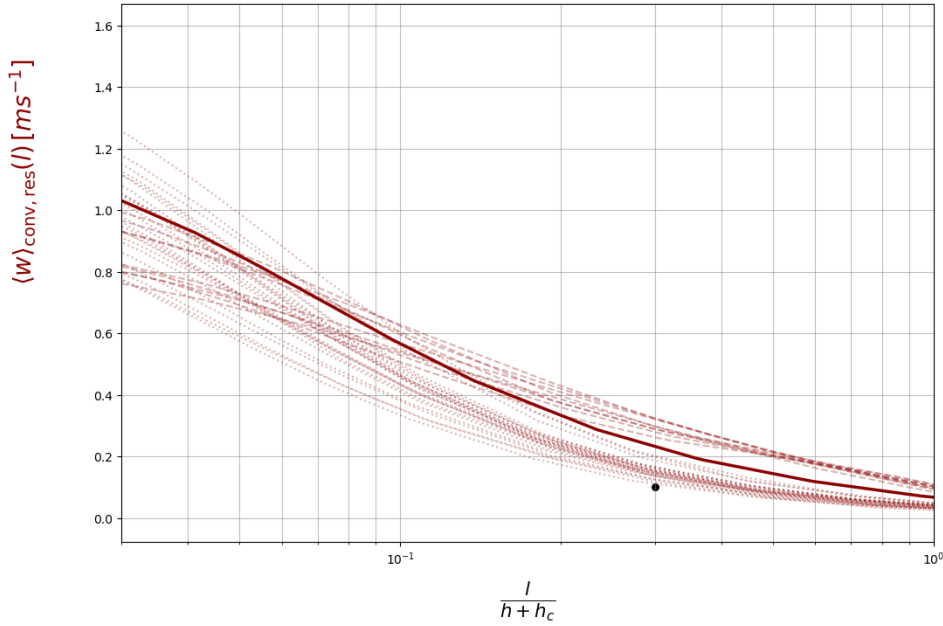


Figure 5.25: Mean vertical velocity of the convective grid, selected with $w > 0$ and $q_t > q_{sat}$. Taken at $0.25 \leq \frac{z_c}{h_c} \leq 0.75$, with $t \in t_{cloudy}$. With the hourly (patterned) and their mean (solid). The dotted lines show the BOMEX results, and the dashed lines show the Cabauw results.

From these findings, the LES results were used again to create an additional figure, shown in 5.25. In this figure, the mean vertical velocity of the grids that were selected as convective updrafts in the cloud layer, is plotted against the resolution, normalized with the height of the cloud layer. This shows that the correlation between this relative resolution and these mean velocities coincide well for both cases. Both gradually decrease from averagely 1.0 m/s at LES resolution, to nearly zero at $l = h + h_c$, as the updrafts are dissolved at this resolution. The black dot indicates the vertical velocity threshold used at the HARMONIE runs, $w_{max} = 0.1$ m/s, plotted against the resolution normalized with the average cloud height. This shows to be lower than the average LES-based convective velocity, and especially lower than that of the Cabauw case. This may explain that the threshold of the vertical velocity is set too low for these HARMONIE run, and a higher threshold could be more effective.

6

Conclusion

In this research, the scale-adaptivity of the HARMONIE EDMF-scheme in the grey zone of turbulence, for the shallow cumulus boundary layer, is investigated in a two-step approach.

Firstly, LES results were used to answer the following questions:

1. *Is the height of the mixed layer (h) expected to be an effective measure for scale-adaptivity of the dry mass-flux of the HARMONIE EDMF-scheme, in the Grey zone of turbulence?*

From the resolved and the unresolved partitioning functions found using LES-based coarse-graining in the mixed layer, the height of the mixed layer showed to represent the dominant size of the convective updrafts sufficiently. These convective updrafts were found to strongly transport the positive moisture flux, transport both positive and negative heat flux and also showed to transport momentum of strong winds. However, for all these quantities, structures similar and even greater in size, that did not contain the highest vertical velocities ($p = 10$ used), were found to strongly contribute the total flux in the mixed layer. From this, it is expected that the height of the mixed layer is effective for scaling down the dry-mass flux itself, but that this may not result in sufficient downscaling of the total parametrized turbulence.

2. *Is the height of the cloud layer ($h + h_c$) expected to be an effective measure for scale-adaptivity of the moist mass-flux from the EDMF-scheme, in the Grey zone of turbulence?*

From the resolved and the unresolved partitioning functions found using LES-based coarse-graining in the mixed layer, the height of the mixed layer showed to represent the dominant size of the convective updrafts sufficiently for the strong convective BOMEX case. These convective updrafts were found to strongly transport the positive moisture flux, transport both positive and negative heat flux and also showed to transport momentum of strong winds. However, the less convective Cabauw case showed much more spread and interference from larger flows. Both cases show almost similar values of the height of the cloud top ($h + h_c$), but very strong differences in the convective strength and stability of the clouds. From this, it is questionable if scaling down the moist mass-flux with this height is sufficient.

Secondly, HARMONIE was run at three different settings to answer the following questions:

3. *Do scale-adaptations on the Dual Mass-Flux, based on h and $h + h_c$, improve the representation of turbulent transport from the HARMONIE model in the Grey zone of turbulence?*

In the mixed layer, the dry mass-flux showed to significantly scale down by using the height of the mixed layer (h), allowing more turbulent transport to be resolved. However, the resulting partitioning of the subgrid flux to the total flux showed to still be higher than expected from the LES results. This may suggest that down-scaling of the dry MF with the height of the mixed layer is not strong enough for this case, or that the ED-scheme, which is not scale-adapted, is too strong. In the cloud layer, the moist mass-flux showed to significantly scale down by using the height of the mixed layer ($h + h_c$), but this did not result in an evenly strong increase in resolved turbulence, suggesting that this height is a too strong indicator of the convective nature of the clouds, in this case.

4. Does an additional vertical velocity threshold improve the representation of turbulent transport from the HARMONIE model in the Grey zone of turbulence?

Both in the mixed layer and in the cloud layer, an additional use of the vertical velocity threshold w_{max} , results in an almost zero mass-flux. With this, the total flux is almost completely defined by the resolved flux, resulting in a too high partitioning of the resolved flux, and a too low value for the total flux. These results suggest that the threshold of the vertical velocity is set too low, shutting down too much of the MF-scheme. An additional LES-based figure of the mean resolved vertical on the selected updrafts grid supports this suggestion.

These conclusions should not be interpreted as decisive in the scale-adaptivity of the EDMF-scheme of the HARMONIE model. They question the application of the height of the boundary layer as a parameter to adapt the scheme in the Grey zone of turbulence, as it does not seem sufficient for these cases studied. However, it does not negate its potential. It should be noted that the resolved and the unresolved partitioning functions are based on applying a running-mean filter on LES fields. This is a rather static method of decomposing these resolved and unresolved values, which is easy to interpret, but gives rise to mathematical effects that are not representative of atmospheric dynamics. For instance, this showed in the coarse-graining of the heat flux, where the negative and positive flux canceled each other out. This could have been avoided by using a spectral analysis. Moreover, the use of conditional sampling on the average fields is somewhat ambiguous. Firstly, the 'convective' grids are selected using thresholds, which themselves are arbitrary. Secondly, applying these thresholds on the stationary filtered fields may not result in convective updrafts that are representative of updrafts that would have dynamically formed from an actual LES run at the same resolution. Furthermore, the HARMONIE runs are simulated for only one case, and the partitioning is only reviewed for the moisture flux. This further emphasizes that these conclusions on the scale-adaptivity of the EDMF scheme are not definitive.

Outlook

To further investigate the scale-adaptivity of the HARMONIE EDMF-scheme in the grey zone of turbulence, a couple of recommendations are proposed.

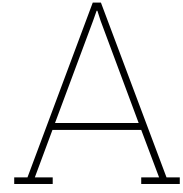
Firstly, it could be more insightful to quantify the resolved and unresolved partitioning to the total turbulence from actually coarsening the resolution of the LES model, as this is more dynamical and may be a better representation of these values.

Secondly, it would be interesting to run the HARMONIE model at the three proposed settings, on additional shallow-cumulus cases to gain a more comprehensive understanding of the effect of the different EDMF-schemes on the representation of the mass-flux, and the consequent overall performance. To accurately assess the efficacy of the different schemes, it would be beneficial to conduct a series of shallow-cumulus simulations under varying environmental conditions. Then, these additional runs could be used to study not only the effect of the scaled-down mass-flux on the moisture flux, but also separately investigate the effect it has on the representation of turbulent transport of moisture, heat and momentum.

Additionally, in 5.25, a first insight into the scale sensitivity of the convective vertical velocity was given. This suggests that the vertical velocity threshold w_{max} may need to be scale-adaptive in order to sufficiently scaled down the MF-scheme. This is substantiated by the observation that the MF-scheme is reduced too strongly in the HARMONIE runs, by using $w_{max} = 0.1\text{m/s}$. In order to gain further insight into the scale-dependency of the convective vertical velocity, it would be beneficial to conduct additional investigation. This could be achieved by employing a similar coarse-graining and conditional sampling method, but utilizing a tracer on increasingly coarse resolutions would provide more robust evidence. Following this, a next step would be to run the HARMONIE with a scale-adaptive vertical velocity threshold w_{max} and review its representation of turbulence and its overall performance.

Lastly, modifying the MF of the EDMF-scheme remains in the anisotropic assumption of subgrid turbulence. However, especially when encountering even higher resolutions, diffuse turbulence may also need to be adapted. It is found the assumption of homogenous and isotropic subgrid diffuse turbulence no longer holds at resolutions finer than half of the boundary-layer height (Honnert, 2016). Therefore, the ED-scheme in the Grey zone may need to be adapted from one-dimensional to three-dimensional. To accurately parametrize turbulence in the Grey zone of turbulence, additional research

into this adaption of the ED-scheme is suggested.



Coarse-graining

To zoom in on the performance of the proposed coarse-graining method, a horizontal cross-section of both the Cabauw case is considered at $\frac{1}{2}h$. This cross-section is taken at 9.00h, with $\frac{1}{2}h = 494\text{m}$ (see table 4.1).

To confirm that the coarse-graining method works in the desired way, two expected results were verified. First, it is expected that as the filter grid-size increases from LES resolution to lower resolutions, the variance of the variable on the horizontal domain tends toward zero. Second, from the definition of averaging, it is expected that the mean of the variable in this domain does not change with decreasing filter resolution. Following these two, it is expected that the overall domain tends towards its mean values as the grid-size of the filter increases.

In figure A.2, the 2D-fields of the potential liquid temperature, the total specific humidity, the vertical velocity, and the horizontal velocities over decreasing filter resolutions are shown. Indeed, the coarse-grained fields show fluctuations diminishing as the resolution reduces, and with this gradually approaching the domain's average value.

In figure A.1, the variance and mean of each variable with growing filter size are plotted for the same location. To easily compare these with each other and with the LES resolution, for all the variables both the variances and mean are normalized by their value at LES resolution. The variances indeed tend toward zero as the filter size increases, compared to their LES variance, and in both cases are almost completely zero with a filter size larger than 1km. Additionally, it shows that the mean values of the two-dimensional fields remain equal to their mean value on the original LES grid size.

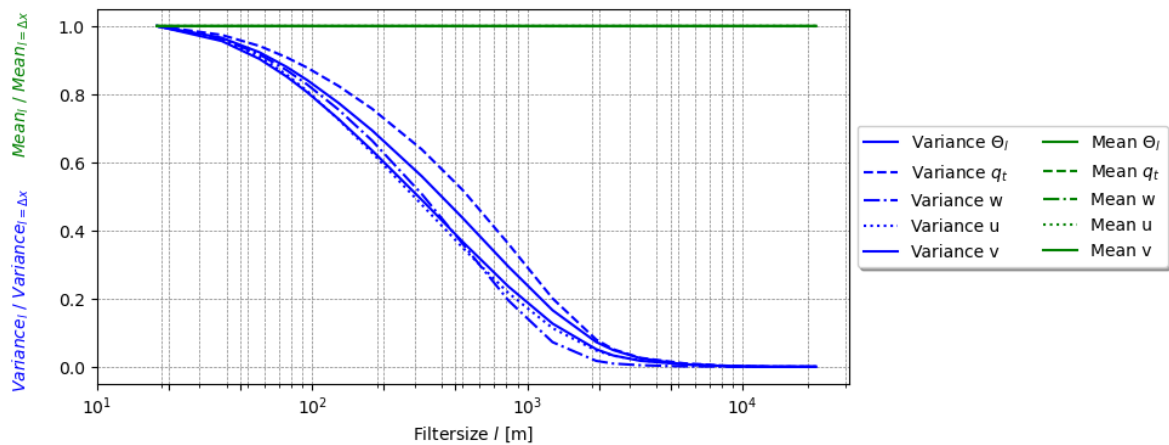


Figure A.1: Normalized variance and mean of prognostic LES variables Θ_l , q_t , w , u and v at $t = 9.00\text{h}$ $z = \frac{1}{2}h$

How the variance decreases, depends on the quantity that is observed. For instance, figure A.1 shows that the variance in the vertical velocity w diminishes faster than that of the total specific humidity

q_t . And indeed, figure A.2 shows that the latter appears to have larger structures than those of the vertical velocity, which consequently remains more visible at larger filter sizes. The grid-size dependency of the variances of the different variables is examined in chapter 5.1.

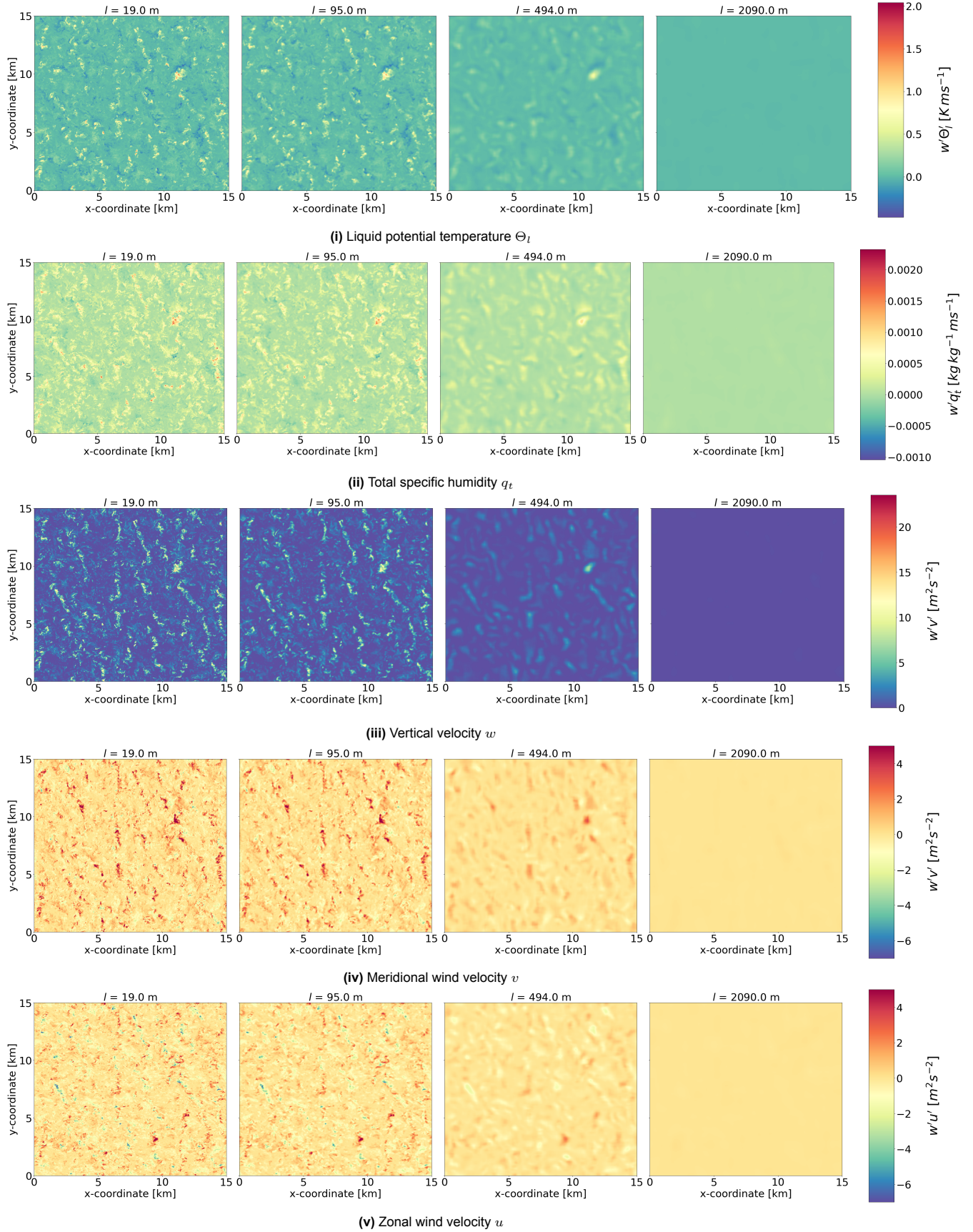


Figure A.2: Coarse-graining the horizontal cross-sections of the liquid potential temperature (Θ_l), the total specific humidity (q_t), and the wind velocities (w , u and v) for the Cabauw case at $t = 9.00h$, $z = \frac{1}{2}h$

B

Conditional sampling

The total turbulent fluxes are decomposed by selecting the updraft and the remaining environmental grids. This is done both in the mixed layer and the cloud layer, with separate thresholds for conditional sampling.

Mixed layer

In the mixed layer, the updraft grids are selected based on the p_{th} percentile of the vertical velocity. With p ranging between 90 and 99.

As the percentile decreases, lower velocities are considered as updrafts and higher area fractions are selected. This is shown for both the BOMEX and the Cabauw case in figure B.2 and B.3, respectively. The figures show that the highest percentiles do not seem to accurately capture the updrafts with strong positive values. It also shows that from $p = 95$ and lower, the areas selected do not strongly grow anymore, especially for the BOMEX case. Additionally, by using a decreasing percentile, the contribution of the convective flux to the total starts to stagnate to approximately 50%, for both cases, shown in figure B.1. Which can be explained as the area of updraft increases, but the difference between the moisture in the updraft and environmental decreases.

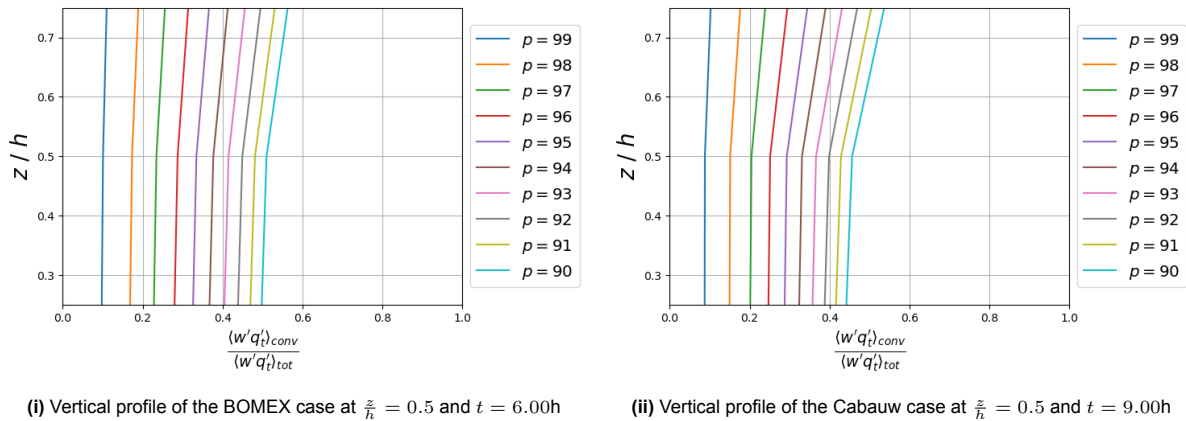


Figure B.1: Vertical profiles of the contribution of the mean convective moisture flux to the mean total moisture flux ($w'q'_t$). For decreasing percentiles used to select the updrafts with $w > w_{p\%}$.

As selecting the percentile from $p = 95$ and below did not significantly impact the size of the mean convective flux in the selected updrafts, $p = 10$ was utilized to ensure that all updrafts were included in the analysis.

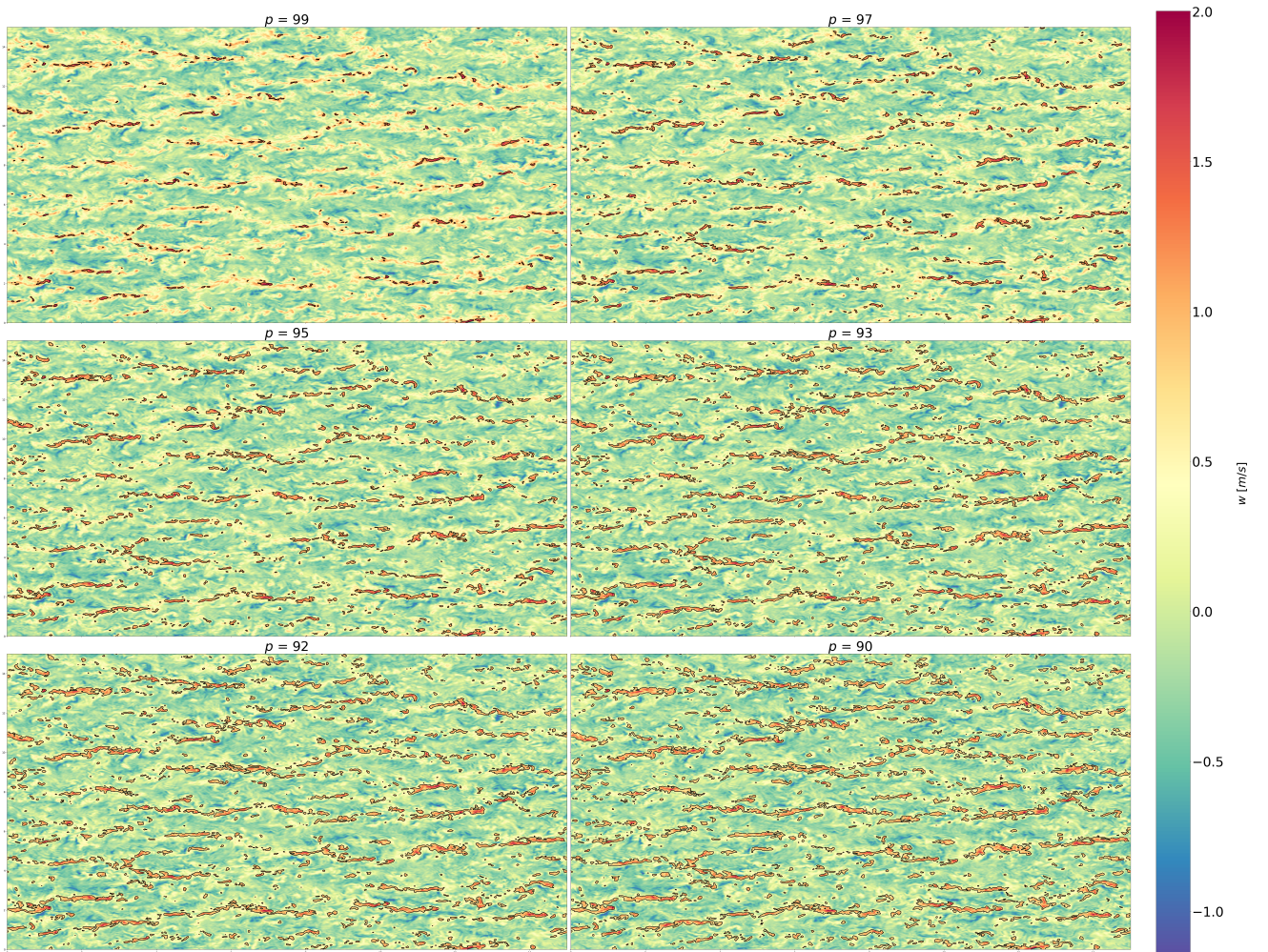


Figure B.2: Cross-section of the mixed layer ($\frac{z}{h} = 0.5$) of the vertical velocity (w) of the BOMEX case at $t = 6.00\text{h}$. The updrafts are selected with $p \in [1, 3, 5, 7, 8, 10]$ of the vertical velocity at LES resolution, and are contoured with a black line.

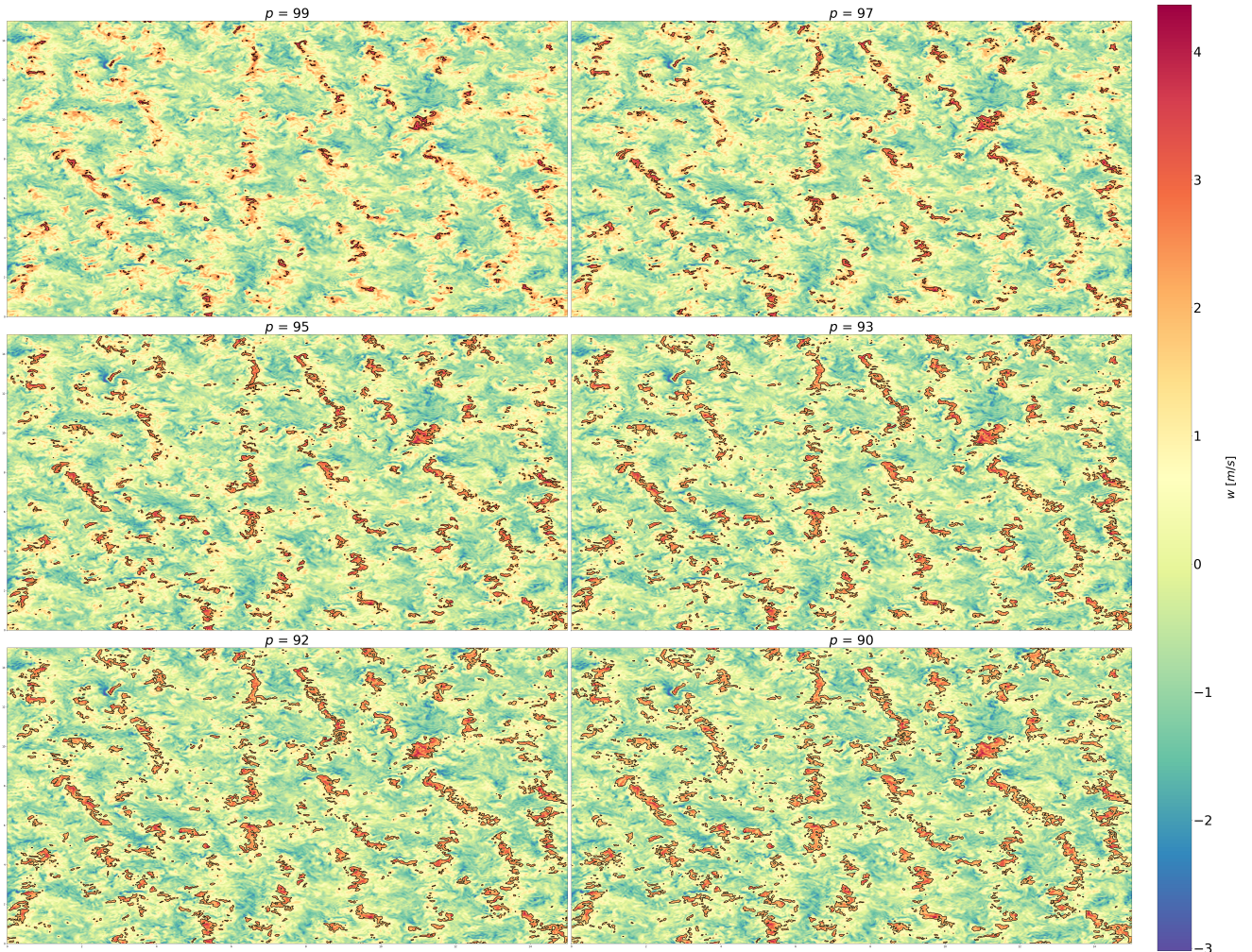


Figure B.3: Cross-section of the mixed layer ($\frac{z}{h_i} = 0.5$) of the vertical velocity (w) of the Cabauw case at $t = 9.00\text{h}$. The updrafts are selected with $p \in [1, 3, 5, 7, 8, 10]$ of the vertical velocity at LES resolution, and are contoured with a black line.

It is important to note that by definition of using a percentile value as a threshold to select updrafts, the area fraction of these updrafts will always be a fixed number. For instance, when choosing the updrafts as those grids with a vertical velocity higher than the 90% percentile of this velocity, the updraft area fraction will always be 10%. Applying the percentile threshold, while coarse-graining, may thus not be representative. This is visualized in figure B.4. In this figure, a cross-section of the Cabauw case in the mixed layer is given, coarse-grained between the LES-resolution up to more than 3km grid-spacing. It becomes evident, that even at these very low resolutions, the grids with velocities higher than the 90th percentile of the vertical velocity of this coarse-grained field are selected as updrafts, even if they are very close to zero.

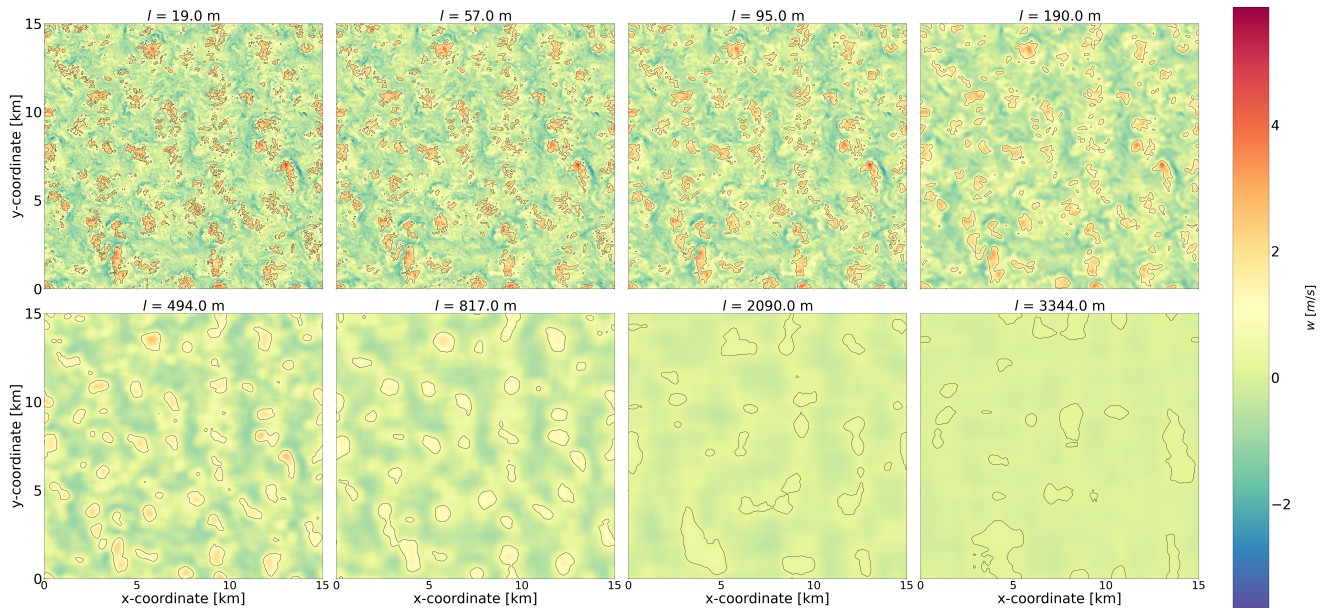


Figure B.4: Coarse-grained cross-section of the mixed layer ($\frac{z}{h} = 0.75$) of the vertical velocity (w) of the Cabauw case. The updrafts are selected with $p = 90$, and are contoured with a black line.

Therefore, the decision is made to select the updraft grids of the coarse-grained field as the grid boxes that have a larger positive vertical velocity than the p -percentile of the vertical velocity distribution at that height at LES resolution.

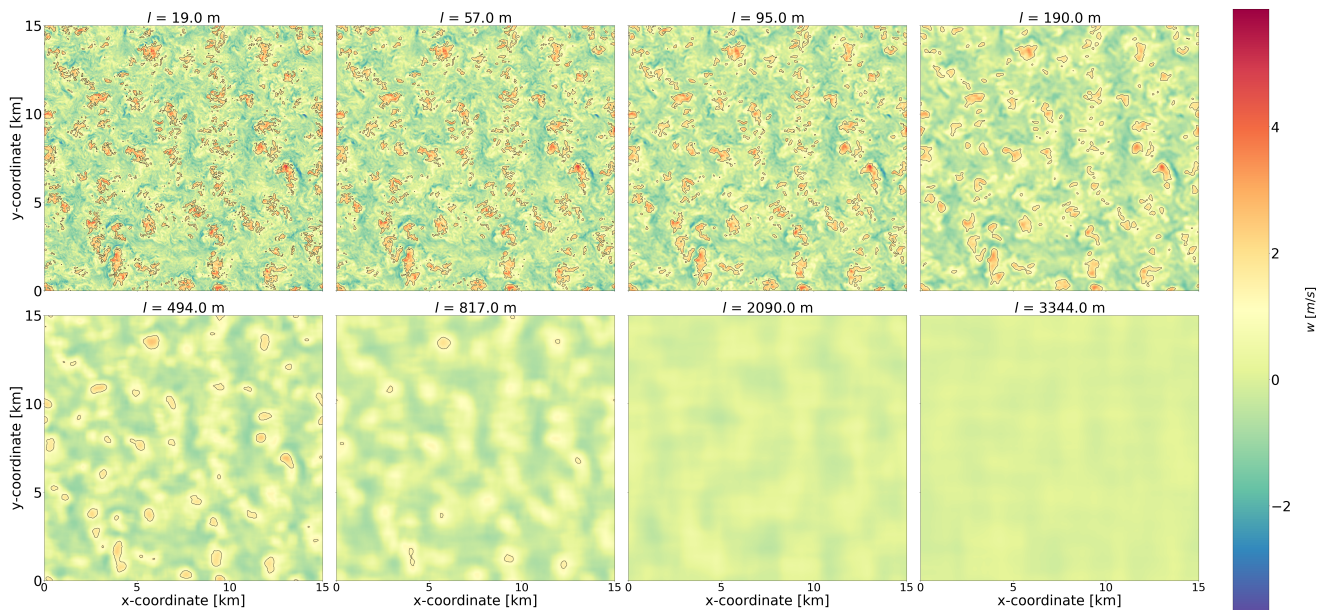


Figure B.5: Coarse-grained cross-section of the mixed layer ($\frac{z}{h} = 0.75$) of the vertical velocity (w) of the Cabauw case. The updrafts are selected with $p = 90$ of the vertical velocity at LES resolution, and are contoured with a black line.

The same cross-section of the Cabauw case is shown in figure B.5, using this p -percentile of the vertical velocity distribution at LES resolution as updraft threshold. This shows to be more effective, as the updrafts decrease with diminishing vertical velocities.

Cloud layer

In the cloud layer, the updraft grids are selected as those containing liquid humidity and that have a positive vertical velocity. As discussed, determining if the grid box contains liquid humidity, is done by

computing the saturation humidity at the resolved field and selecting the grid where the total humidity is greater than this value. This specific approach was applied to prevent averaging the whole field as liquid-containing by coarse-graining. In figure B.6, a coarse-grained cross-section of the liquid specific humidity, computed with $q_l = q_t - q_{sat}$, in the middle of the cloud layer of the Cabauw case is shown. In figure B.7, the same cross-section is shown, while coarse-graining the LES field of the liquid specific humidity q_l . In both figures, the grids containing liquid humidity are contoured with a black line. This shows that, indeed, using the second approach causes an averaging of the liquid humidity over the domain, causing the area of liquid-containing grids to grow with decreasing resolution. This is not representative, confirming the expectation.

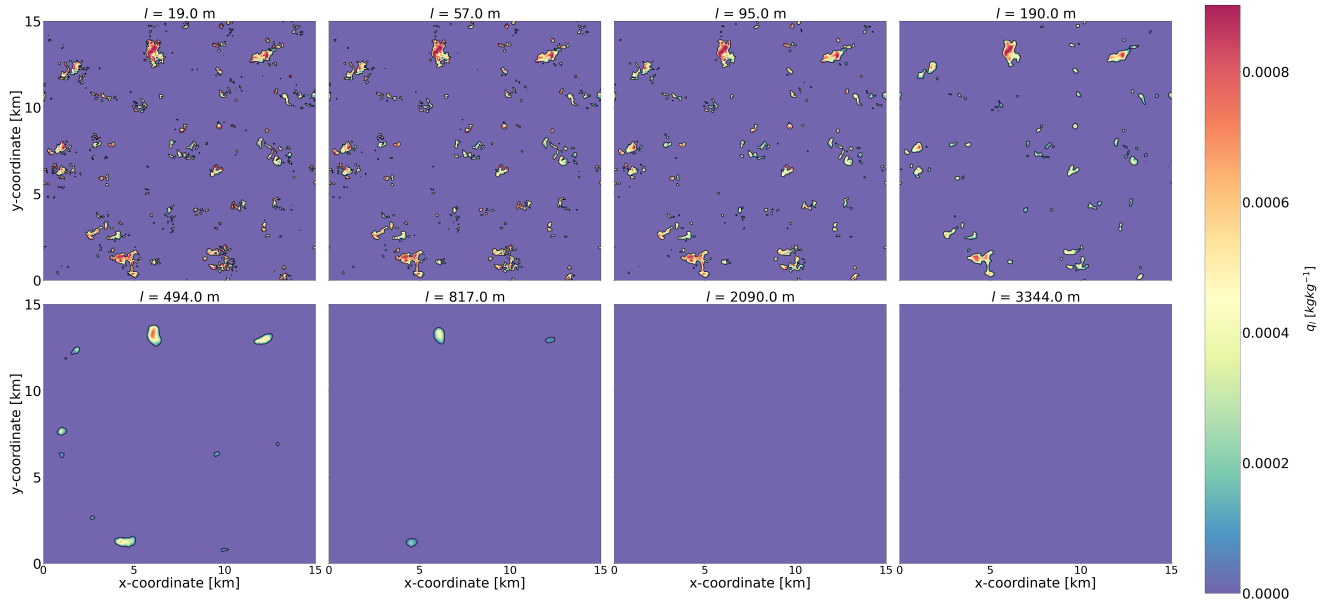


Figure B.6: Coarse-grained cross-section of the cloud layer ($\frac{z_c}{d_c} = 0.5$) of the liquid humidity computed with $q_l = q_t - q_{sat}$ of the Cabauw case. The liquid-containing areas are contoured with a black line.

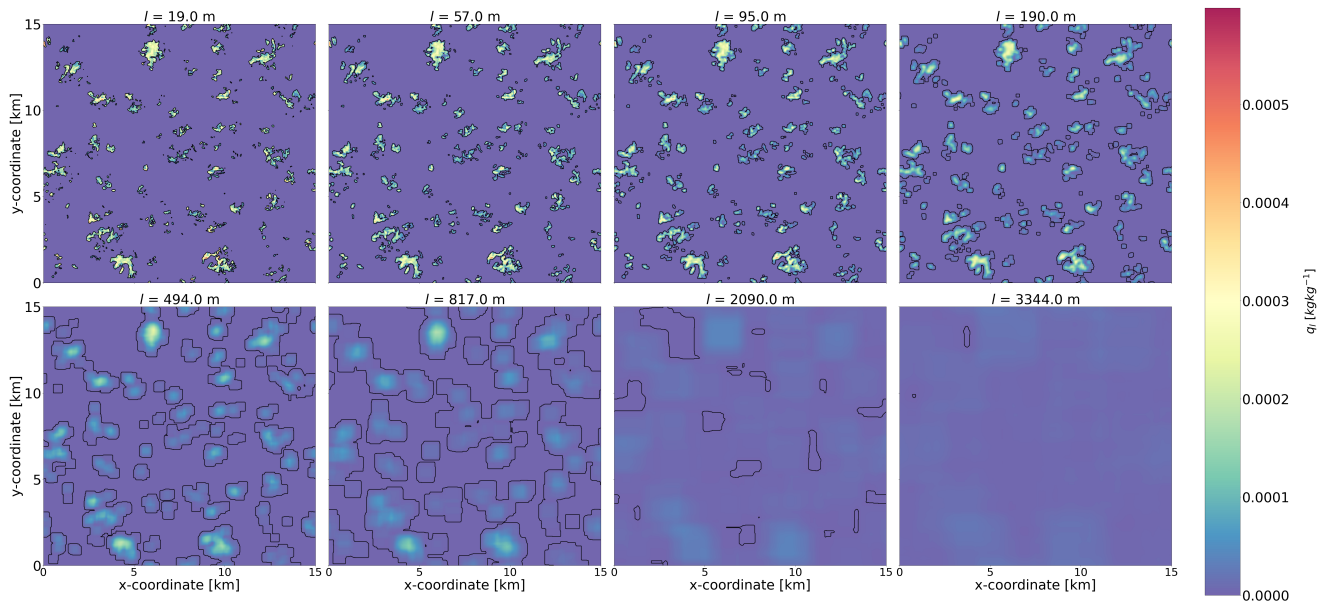
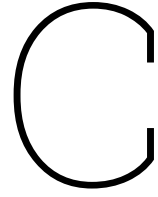


Figure B.7: Coarse-grained cross-section of the cloud layer ($\frac{z_c}{d_c} = 0.5$) of the liquid humidity q_l of the Cabauw case. The liquid-containing areas are contoured with a black line.



Scaling with other heights

The partitioning functions were also examined using alternative scales to normalize the grid-spacing, using the height of the cloud layer ($h + h_c$) in the mixed layer and using the depth of the cloud layer (h_c) in the cloud layer. Neither showed improvement in scaling, compared to the heights used in this research.

C.1. Scaling with $h + h_c$ in the mixed layer

The resolved and unresolved partitionings to the total moisture and heat flux in the mixed layer are plotted against the grid-size, normalized with the height of the cloud layer ($h + h_c$).

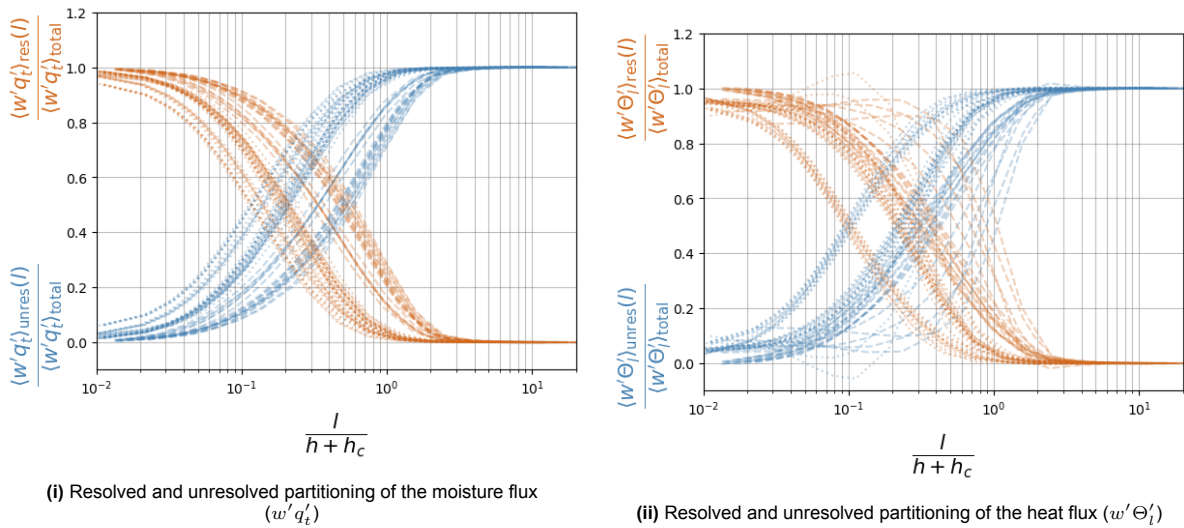


Figure C.1: Partitioning functions, at $0.25 \leq \frac{z}{h} \leq 0.75$, with $t \in t_{cloudy}$. With the hourly (patterned) and mean (solid) partitionings of the resolved (orange) and unresolved (blue) fluxes. The dotted lines show the BOMEX results, and the dashed lines show the Cabauw results. The grid size is normalized with the height of the cloud layer

C.2. Scaling with h_c in the cloud layer

The resolved and unresolved partitionings to the total moisture and heat flux in the mixed layer are plotted against the grid-size, normalized with the depth of the cloud layer (h_c).

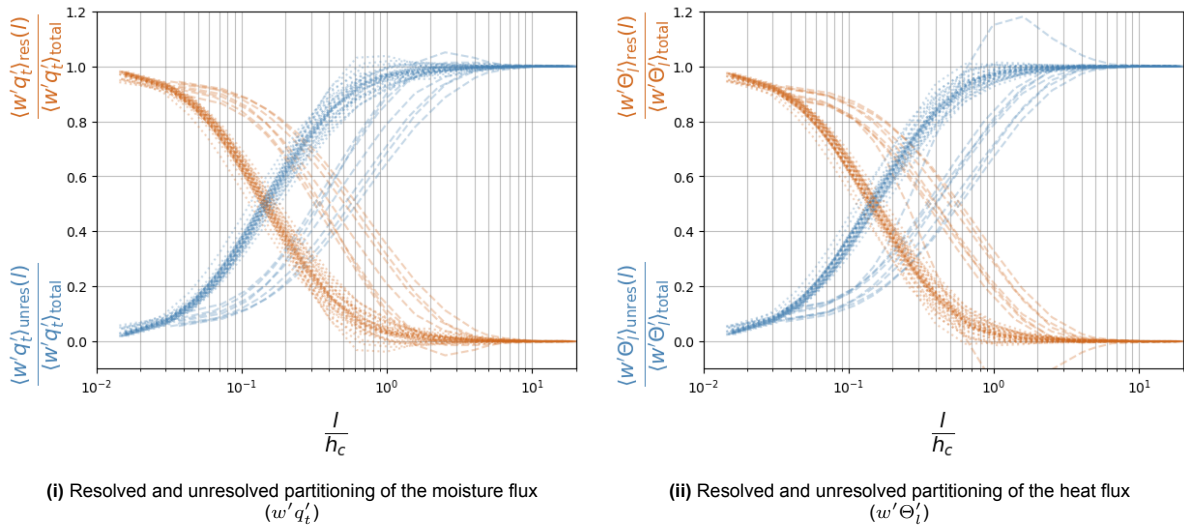


Figure C.2: Partitioning functions, at $0.25 \leq \frac{z_c}{h_c} \leq 0.75$, with $t \in t_{cloudy}$.

With the hourly (patterned) and mean (solid) partitionings of the resolved (orange) and unresolved (blue) fluxes. The dotted lines show the BOMEX results, and the dashed lines show the Cabauw results. The grid size is normalized with the depth of the cloud layer

D

TKE

The TKE budget is an important parameter for turbulence modeling. It is used to determine the diffusivity for modelling small-scale turbulence, and couples the convective and diffusive turbulence by enabling energy cascade from the larger eddies down to the smaller ones. This energy from turbulent velocity structures is represented with the variances of both the vertical and horizontal velocities (2.22). The resolved and unresolved partitioning to the total TKE is depicted for the mixed layer in figure D.1, and for the cloud layer in figure D.2.

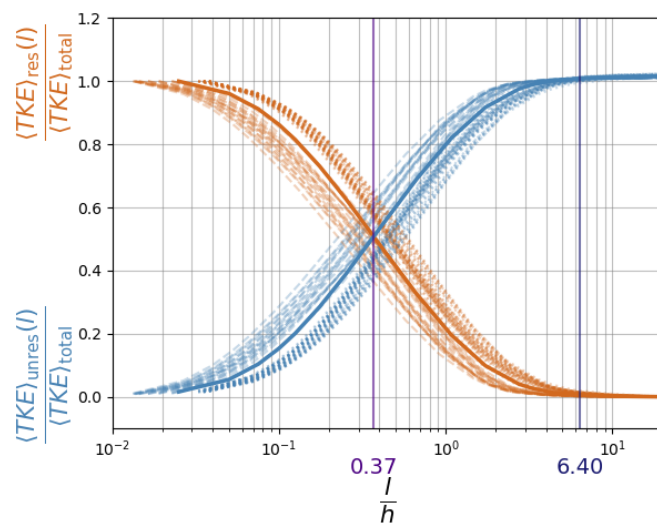


Figure D.1: Partitioning functions TKE, at $0.25 \leq \frac{z}{h} \leq 0.75$, with $t \in t_{cloudy}$.
 With the hourly (patterned) and mean (solid) partitionings of the resolved (orange) and unresolved (blue) TKE.
 The dotted lines indicate the BOMEX case, and the dashed lines indicate the Cabauw case.
 The indicators I_{int} and I_{exc} are depicted in light and dark purple

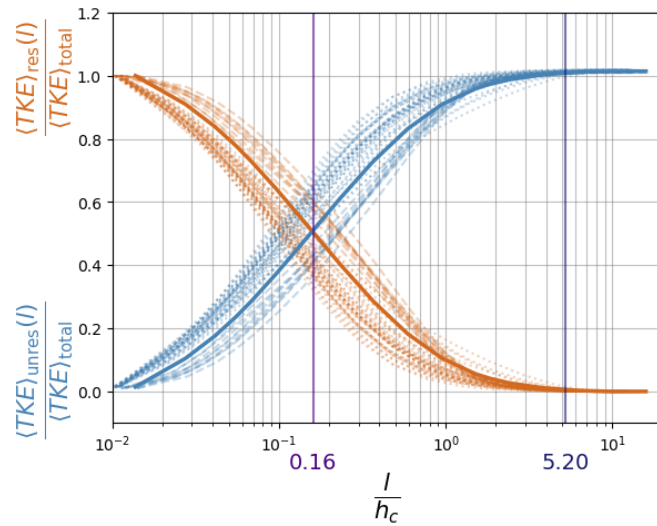


Figure D.2: Partitioning functions TKE, at $0.25 \leq \frac{z_c}{h_c} \leq 0.75$, with $t \in t_{cloudy}$.

With the hourly (patterned) and mean (solid) partitionings of the resolved (yellow) and unresolved (green) TKE. The dotted lines indicate the BOMEX case, and the dashed lines indicate the Cabauw case. The indicators I_{int} and I_{exc} are depicted in light and dark purple